Università degli Studi di Milano-Bicocca

Dipartimento di Fisica G. Occhialini

Corso di Dottorato in Fisica e Astronomia - Ciclo XXVI

Ph.D. Thesis

Development and Experimental Validation of a Monte Carlo Simulation Model for the TRIGA Mark II Reactor

Davide Chiesa

Supervisor:
Prof. Ezio Previtali

Settore Scientifico Disciplinare FIS/07

Anno Accademico 2012/2013

I dedicate this thesis
to Attilia, the joy of my life,
and to Fiorella and Roberto,
for the gift of life and education.

Contents

Introduction

The increasing worldwide energy demand, especially in the developing countries, and the environmental effects generated by energy production, such as soil and atmospheric pollution, issue great challenges for the future.

The urgent need to find safe, clean and possibly inexpensive energy supplies is leading to a gradual reduction of the fossil fuels exploitation, thus limiting the CO_2 emissions, responsible of the so-called greenhouse effect.

Many issues could be addressed by simultaneously exploiting the different available energy sources. In this respect, the slow and limited introduction of new renewable energies, are pushing worldwide towards a rekindling of interest in nuclear energy from fission [1]. In fact, several combined factors, such as economic advantage over other comparable sources, the low level of fuel costs and negligible emissions of gas and dust with noticeable environmental impact, make nuclear power competitive.

The International Atomic Energy Agency (IAEA) reports that, in 2013, there are 434 operational nuclear power reactors, providing a total net electrical capacity of 370 GWe, which are equal to 6% of world total energy and 16% of world electricity. Moreover, 69 power reactors are under construction worldwide, most of them in China (28), Russia (10) and India (7).

However, despite some advantages, nuclear energy produced by fission presents also some disadvantages. One of the main drawbacks affecting current technology are the low efficiency in the use of uranium resources and the abundant production of high-level nuclear waste, mostly made of long-lived fission fragments and trans-uranium (TRU) actinides. For this reason, new systems are being investigated, which could allow to overcome the limitations of current nuclear technology.

A promising solution to the waste problem is the use of subcritical Accelerator Driven Systems (ADS), in which isotopes with long lifetime are transmuted in stable or short-lived nuclei by means of neutron-induced reac-

tions (mainly capture and fission). In this scheme, high-current, high-energy proton or deuteron accelerator supplies the neutron flux necessary to sustain the transmutation reactions.

On the other hand, the so-called Generation IV nuclear reactors could also offer a valuable solution to the waste problem. The main concept of these reactors is the exploitation of nuclear reactions induced by fast neutrons so to achieve the partial or full recycling of trans-uranium actinides. In this way, the uranium resources would be used with higher efficiency and the final volume of high-level nuclear waste to be stored in geological repositories would be minimized. In this panorama, although nuclear reactors have been operational for several decades, there are many aspects to be investigated and much research still needs to be carried out. In particular, the design of advanced nuclear energy systems requires:

- more accurate neutron cross section data for a large number of isotopes involved in the new fuel cycles and used as structural materials;
- the development of methodologies and tools for analyzing the reactor neutronics, dynamics and fuel cycle.

In recent years, many computer codes, based on Monte Carlo methods or deterministic calculations, have been developed to separately analyze different aspects regarding nuclear reactors. However, it should be noted that reactors are very complex systems, which require an integrated analysis of all the variables which are intrinsically correlated: neutron fluxes, reaction rates, neutron moderation and absorption, thermal and power distributions, heat generation and transfer, criticality coefficients, fuel burnup, etc. For this reason, one of the main challenges in the analysis of nuclear reactors is the coupling of neutronics and thermal-hydraulics simulation codes [2], with the purpose of achieving a good modeling and comprehension of the mechanisms which rule the transient phases and the dynamic behavior of the reactor. This is very important to guarantee the control of the chain reaction, for a safe operation of the reactor.

In developing simulation tools, benchmark analyses are needed to prove the reliability of the simulations. The experimental measurements conceived to be compared with the results coming out from the simulations are really precious and can provide useful information to improve the description of the physics phenomena in the simulation models.

My PhD research activity was held in this framework, as part of the research project *Analysis of Reactor COre* (ARCO, promoted by INFN) whose task was the development of modern, flexible and integrated tools for the

analysis of nuclear reactors, relying on the experimental data collected at the research reactor TRIGA Mark II, installed at the Applied Nuclear Energy Laboratory (LENA) at the University of Pavia. In this way, once the effectiveness and the reliability of these tools for modeling an experimental reactor have been demonstrated, these could be applied to develop new generation systems.

In this thesis, I will present the complete neutronic characterization of the TRIGA Mark II reactor, which was analyzed in different operating conditions through experimental measurements and the development of a Monte Carlo simulation tool (relied on the MCNP code) able to take into account the ever increasing complexity of the conditions to be simulated.

First of all, after giving an overview of some theoretical concepts which are fundamental for the nuclear reactor analysis (Chapter 1), a model that reconstructs the first working period of the TRIGA Mark II reactor, in which the "fresh" fuel was not heavily contaminated with fission reaction products, will be described (Chapter 2).

In particular, all the geometries and the materials are described in the MCNP simulation model with good detail, in order to reconstruct the reactor criticality and all the effects on the neutron distributions. The very good results obtained from the simulations of the reactor at low power condition −in which the fuel elements can be considered to be in thermal equilibrium with the water around them− are then used to implement a model for simulating the full power condition (250 kW), in which the effects arising from the temperature increase in the fuel-moderator must be taken into account. The MCNP simulation model was exploited to evaluate the reactor power distribution and a dedicated experimental campaign was performed to measure the water temperature within the reactor core. In this way, through a thermal-hydraulic calculation tool, it has been possible to determine the temperature distribution within the fuel elements and to include the description of the thermal effects in the MCNP simulation model.

Thereafter, since the neutron flux is a crucial parameter affecting the reaction rates and thus the fuel burnup, its energy and space distributions are analyzed presenting the results of several neutron activation measurements (Chapter 3).

Particularly, the neutron flux was firstly measured in the reactor's irradiation facilities through the neutron activation of many different isotopes. Hence, in order to analyze the energy flux spectra, I implemented an analysis tool, based on Bayesian statistics, which allows to combine the experimental data from the different activated isotopes and reconstruct a multi-group flux spectrum. Subsequently, the spatial neutron flux distribution within the

core was measured by activating several aluminum-cobalt samples in different core positions, thus allowing the determination of the integral and fast flux distributions from the analysis of cobalt and aluminum, respectively.

Finally, I will present the results of the fuel burnup calculations, that were performed for simulating the current core configuration after a 48 years-long operation. The good accuracy that was reached in the simulation of the neutron fluxes, as confirmed by the experimental measurements, has allowed to evaluate the burnup of each fuel element from the knowledge of the operating hours and the different positions occupied in the core over the years. In this way, it has been possible to exploit the MCNP simulation model to determine a new optimized core configuration which could ensure, at the same time, a higher reactivity and the use of less fuel elements. This configuration was realized in September 2013 and the experimental results confirm the high quality of the work done.

Based on the results achieved during this thesis work, the following publications have been produced:

- A. Borio di Tigliole and *et al.*, "TRIGA reactor absolute neutron flux measurement using activated isotopes", *Progress in Nuclear Energy*, vol. 70, pp. 249-255, January 2014;
- D. Chiesa, E. Previtali, and M. Sisti, "Bayesian statistical analysis applied to NAA data for neutron flux spectrum determination", *accepted for publication in Nuclear Data Sheets*;
- D. Alloni and *et al.*, "Final characterization of the first critical configuration for the TRIGA Mark II Reactor of the University of Pavia using the Monte Carlo code MCNP", *submitted to Progress in Nuclear Energy*;
- D. Chiesa, E. Previtali, and M. Sisti, "Bayesian statistics applied to neutron activation data for reactor flux spectrum analysis", *submitted to Annals of Nuclear Energy.*

Chapter 1

Theoretical background for nuclear reactor analysis

The operation of a nuclear reactor depends fundamentally on the way in which neutrons interact with atomic nuclei.

In the first section of this chapter, I will present the mechanisms of neutron interaction with matter, deepening the aspects related to the thermal motion of nuclei and the chemical binding effects. Moreover, the fission reaction will be treated with some detail, focusing the aspects which are relevant for nuclear reactors.

In the second section, the nuclear reactors operating principles will be discussed defining the most important physical quantities, explaining the main models used to describe the moderation and the diffusion of neutrons and deriving the so-called *inhour equation*, which is fundamental for the kinetic analysis of nuclear systems (see [3], [4] and [5] as references for this chapter).

1.1 Neutron interaction with matter

Neutrons interact with matter in a variety of ways. In general, three main categories of interactions can be identified: the *elastic scattering* (n, n), the *inelastic scattering* (n, n') and the *absorption reactions*. In the first case, the nucleus is unchanged in both isotopic composition and internal energy after interacting with a neutron. On the other hand, if the nucleus, still unchanged in composition, is left in an excited state, the process is called inelastic scattering because the kinetic energy is not conserved. Finally, we speak about absorption if the original neutron disappears after the interaction.

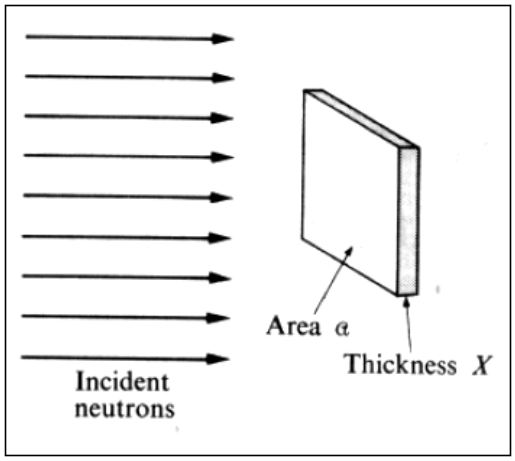

Fig. 1.1: Neutrons incident on a target.

The most important absorption reaction is *radiative capture* (n, γ), in which $\gamma-$radiation is one of the reaction products. Neutrons also disappear in charged-particle reactions such as the (n, p) or (n, α). Moreover, when a nucleus is struck by a high-energy neutron, reactions having two or more products $-$such as $(n, 2n)$, $(n, 3n)$, (n, pn), $(n, n\alpha)$ and some other$-$ can also occur. Finally, when a neutron collides with certain heavy nuclei, the nucleus splits into two or more fragments with the release of considerable energy and the emission of some free neutrons. This is the *fission* reaction, which is the basis for the design of nuclear reactors.

The interactions of neutrons with matter are quantitatively described through the *cross sections*, which are closely related to the probability that an incident neutron interacts with a nucleus in the target under consideration. In particular, when considering a thin target of area $\mathcal{A}$ and thickness X, containing $\mathcal{N}$ atoms per unit volume, placed in a uniform beam of neutrons of intensity I (to be intended as the number of neutrons per $\mathrm{cm}^2 \cdot \mathrm{s}$), as shown in Fig. 1.1, the interaction rate in the entire target R fulfills the following proportionality law:

$$R = \sigma I \mathcal{N} \mathcal{A} X \tag{1.1}$$

where the proportionality constant σ is the cross section, which has the dimensions of area and is usually measured in units of barns ($1\, b = 10^{-24}\mathrm{cm}^2$). In this picture, since $I\mathcal{A}$ neutrons strike the target per second, the relative probability that any one neutron in the beam interacts is:

$$\frac{\sigma I \mathcal{N} \mathcal{A} X}{I \mathcal{A}} = \left(\frac{\sigma}{\mathcal{A}}\right) (\mathcal{N} \mathcal{A} X) \tag{1.2}$$

Since $\mathcal{N}\mathcal{A}X$ is the number of nuclei in the target, it follows that $\sigma/\mathcal{A}$ is

the probability per target nucleus that a neutron in that portion of the beam striking the target will interact. Since the target area is fixed by the experiment, the probability of interaction is determined by σ alone. It is therefore convenient to describe each type of interaction in terms of a characteristic cross section, which usually depends on the target nucleus and on the incident neutron energy.

Finally, the intensity of a monoenergetic neutron beam crossing a target with thickness x fulfills the following exponential attenuation law:

$$I(x) = I_0 e^{-\mathcal{N}\sigma x} \tag{1.3}$$

in which $\mathcal{N}\sigma$ clearly represents the interaction probability per unit path. This quantity is called *macroscopic cross section* (Σ) and is closely related to the neutron *mean free path* (λ) through the relation:

$$\lambda = \frac{1}{\Sigma} \tag{1.4}$$

1.1.1 Total cross section

The total cross section (σ_t) is defined as the sum of the cross sections associated to each possible interaction:

$$\sigma_t = \sigma_s + \sigma_i + \sigma_a = \sigma_s + \sigma_i + \sigma_\gamma + \sigma_f + ... \tag{1.5}$$

where the subscripts indicate, respectively, the elastic scattering (s), the inelastic scattering (i) and the absorption reactions (a), which can be further specified in different components: radiative capture (σ_γ), fission (σ_f), etc.

The total cross section is usually measured in transmission experiments, which over time have provided a lot of data for most part of isotopes. Although the cross sections depend on the nature of target nuclei, it is possible to identify few rather broad categories of isotopes characterized by similar features.

Light ($A \leqslant 25$) and magic nuclei. At low energy, between 0.01 eV and 1 eV, σ_t behaves as:

$$\sigma_t = C_1 + \frac{C_2}{v} \tag{1.6}$$

where v is the neutron velocity, while C_1 and C_2 are constants related to the elastic scattering and the capture reactions, respectively. If $C_1 \gg C_2$, σ_t is approximately constant in this energy range, as in the case of ^{12}C (Fig. 1.2a). On the contrary when $C_2 \gg C_1$, the second term of Eq. 1.6 dominates over

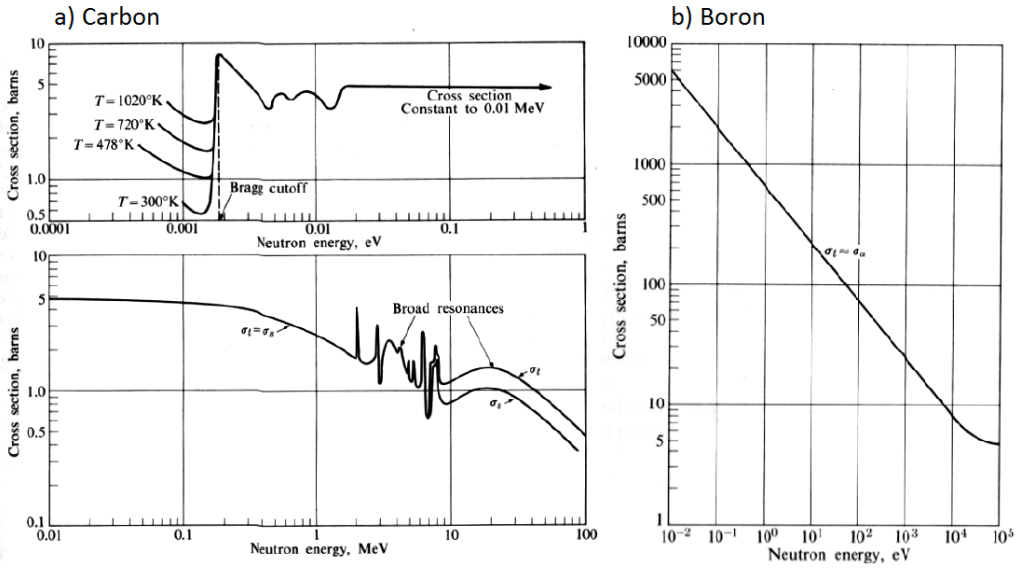

Fig. 1.2: Total cross section of carbon (left) and boron (right).

the first and the cross section exhibits a $1/v$ behavior (Fig. 1.2b), which is characteristic of radiative capture or any other exothermic reaction which may be possible at these energies. Looking at ^{12}C, it will be noted that at very low energies ($E < 0.01$ eV) the cross section exhibits a complicated and temperature dependent behavior: this is due to various crystalline effects which influence the thermal neutrons interactions (see Sec. 1.1.2). At higher energies, instead, a number of fairly wide peaks, called *broad resonances*, are observed in the MeV-region. The above remarks concerning σ_t for light nuclei apply equally well to some *magic nuclei* [1]. This is the case, for example of ^{208}Pb, whose nucleus contains two magic numbers: 126 neutrons and 82 protons. This isotope exhibits a cross section similar to the ^{12}C one, being nearly constant up to about 0.01 MeV.

Heavy nuclei ($A \geqslant 150$). With heavy nuclei, such as ^{238}U, σ_t may again be constant or exhibit a $1/v$ behavior at low energy. However, this is followed in the eV-region by a series of very sharp and close resonances, in which the cross section rises to large values (Fig. 1.3).

The presence of these resonances can be explained by the *compound nucleus formation* interaction mechanism. In this process the incident neutron is absorbed by the nucleus, forming a compound nucleus at the energy $E_n + B$

[1] The nuclei with proton or neutron numbers equal to 2, 8, 20, 28, 50, 82 or 126 have particularly large binding energies and are hence more stable against nuclear decay.

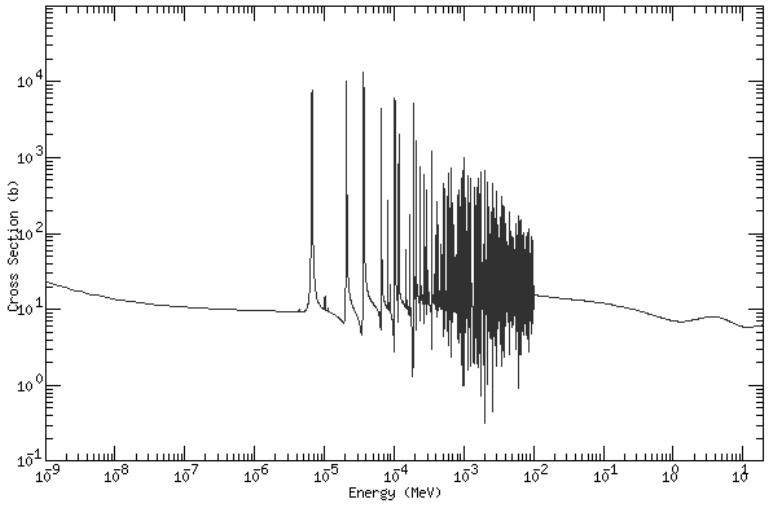

Fig. 1.3: Total cross section of ^{238}U.

above the ground state (where E_n is the neutron kinetic energy and B the binding energy acquired by the nucleus when absorbing the neutron). The compound nucleus can immediately decay with the reemission of the neutron −this is the case of the *resonance scattering*, which can be either elastic or inelastic− or by the emission of one or more *capture* γ*-rays*, eventually reaching the ground state. It can be shown using quantum mechanics models that the probability of formation of the compound nucleus is high if the compound nucleus has an excited state in the vicinity of the energy $E_n + B$, thus explaining the presence of the resonance peaks in the cross sections.

Intermediate nuclei ($25 \leqslant A \leqslant 150$)**.** Finally, the total cross sections of intermediate nuclei exhibits features similar to both light and heavy nuclei. The resonance region usually extends from around 10 eV to the keV-region, but the resonances are neither as narrow and high as in the heavy nuclei, nor as wide and short as they are in light nuclei.

1.1.2 Thermal motion and chemical binding effects

In describing the neutron interaction with matter it is important to consider two aspects:

- the thermal motion of nuclei;
- the chemical bindings of atoms within the molecules or the solid lattices.

The first one is relevant for modelling the thermal neutron scattering, because the neutron velocities are comparable with the ones of nuclei, which can not be assumed *at rest*. Moreover, the thermal motion causes the *Doppler broadening* of the resonance peaks, with considerable consequences on the absorption processes.

On the other hand, the chemical binding effects are not negligible if the neutron energy is below few eV (which is the typical binding energy in molecules and lattices). In this case the nuclei can not be considered to be *free*, because the neutron has not enough energy to disrupt the chemical bindings. It is so necessary to consider the whole molecule or lattice mass, together with the possibility of rotational and vibrational quantum exchanges.

Free gas model for temperature dependence analysis

In considering the elastic scattering of neutrons within a material characterized by $\sigma_s \gg \sigma_a$, a condition of *thermal equilibrium* is reached, because neutrons can either transfer energy to the material or receive some energy from the nuclei, which have a thermal energy of the order of kT.

In order to understand the dependence of the cross section from the material temperature, the so-called *"free gas"* model can be considered. When a neutron interacts with a gas of free atoms, the available energy in the elastic interaction is given by:

$$E_c = \frac{1}{2}\mu v_r^2 \tag{1.7}$$

where μ is the reduced mass and v_r the relative velocity of the neutron-nucleus system. Therefore, a monoenergetic neutron beam interacts with different E_c depending on whether the nucleus is moving in the same or in the opposite direction with respect to the neutron. In considering the interaction rate in the laboratory and in the center-of-mass coordinate systems, the following equivalence can be written:

$$IN\bar{\sigma}(E,T) = \int nv_r\sigma(E_c)N(\mathbf{V})d\mathbf{V} \tag{1.8}$$

where N is the number of atoms in the target and $\bar{\sigma}(E,T)$ is the observed cross section in the laboratory system, which depends on the temperature T and on the neutron energy E. In the second member, nv_r is the neutron beam intensity in the center-of-mass system (being n the neutron beam density), while $N(\mathbf{V})d\mathbf{V}$ is the number of nuclei with velocities between $\mathbf{V}$ and $\mathbf{V}+d\mathbf{V}$. Now, since it is known from theory that the elastic cross section in the center-of-mass system $\sigma(E_c)$ is constant at low energies and observing that the beam

intensity I is equal to nv (where v is the laboratory neutron speed), the observed cross section results:

$$\bar{\sigma}(E,T) = \frac{\sigma}{v} \int v_r \, P(\mathbf{V}) \, d\mathbf{V} \tag{1.9}$$

where $P(\mathbf{V})$ is the probability distribution of the nuclei velocities. As predicted by statistical mechanics, the free gas nuclei velocities follow a *Maxwell-Boltzmann* distribution:

$$P(\mathbf{V}) \, d\mathbf{V} = \left(\frac{M}{2\pi kT} \right)^{\frac{3}{2}} \exp\left(-\frac{MV^2}{2kT} \right) V^2 \, dV \, d\Omega_V \tag{1.10}$$

Hence, defining $\zeta^2 = AE/kT$ (where $A = M/m$ is the ratio of the mass of the scattering atom to the neutron mass) and carrying out the integral in Eq. 1.9, it results that:

$$\bar{\sigma}(E,T) = \sigma \left[\left(1 + \frac{1}{2\zeta^2} \right) \mathrm{erf}(\zeta) + \frac{1}{\zeta\sqrt{\pi}} e^{-\zeta^2} \right] \tag{1.11}$$

where $\mathrm{erf}(\zeta)$ is the so called *error function*, which is defined as:

$$\mathrm{erf}(\zeta) = \frac{2}{\sqrt{\pi}} \int_0^{\zeta} e^{-x^2} dx \tag{1.12}$$

In conclusion, it is possible to analyze two limiting cases:

$$\begin{cases} \bar{\sigma}(E,T) \propto \dfrac{\sigma}{\zeta} \propto \sigma \dfrac{\sqrt{T}}{v} & \text{if } AE \ll kT \ (\zeta \to 0) \\ \bar{\sigma}(E,T) \to \sigma & \text{if } AE \gg kT \ (\zeta \to \infty) \end{cases} \tag{1.13}$$

In the first case, the cross section exhibits a behavior proportional to $\sqrt{T}/v$; instead, when the thermal energy becomes to be negligible, the observed cross section tends to the value of σ for nuclei *at rest*, as expected.

Chemical binding effects

The "free gas" model is based on the hypothesis that nuclei are not bound with the surrounding atoms. However, this simplified model is not suitable to take into account the complexity of the thermal neutron scattering by molecules or solid lattices: in fact, it is experimentally observed that the cross section at energies below few eV is usually greater for bound nuclei respect to the free ones.

Using elementary quantum mechanics and assuming the temperature near to absolute zero, it can be shown that the cross section for the scattering of a neutron by a single nucleus is proportional to the square of the reduced mass of the two particles:

$$\sigma_{free} \propto \mu^2 = \left(\frac{mM}{m+M}\right)^2 \approx \left(\frac{A}{A+1}\right)^2 \tag{1.14}$$

At energies comparable to or less than the chemical binding energy (B_m), the nucleus is no longer free and, as a result, its mass effectively increases: in the limit $E/B_m \to 0$, it becomes equal to the mass of the entire molecule. Therefore, except for light molecules, the reduced mass of the system approaches the mass of the neutron alone:

$$\sigma_{bound} \propto \mu^2 = (1)^2 \tag{1.15}$$

It follows that in the limit as $E/B_m \to 0$ and $T \to 0$ K, the bound and free cross sections are related by:

$$\sigma_{bound} = \left(\frac{A+1}{A}\right)^2 \sigma_{free} \tag{1.16}$$

This phenomenon is illustrated schematically in Fig 1.4. It is worth noting that since the factor $[(A+1)/A]^2$ increases with decreasing A, this bound-nucleus effect is of great importance for the light nuclei, especially for hydrogen. In general, for temperatures above the absolute zero, the adjustment factor for the binding effects is lower, however this correction must be combined with the one due to the thermal motion of nuclei.

The low-energy scattering cross section may also be complicated by the occurrence of *coherent scattering*. This effect arises as the result of the interference of neutron waves from different nuclei in the molecule or lattice and it can lead to anomalous values of the low-energy cross section. Although it is negligible for the molecules containing hydrogen, it is important for solids with a lattice structure such as graphite, beryllium and uranium oxide (UO_2). By analogy with the X-rays model, this effect is also referred to as *Bragg scattering*. If a beam of monoenergetic neutrons is incident at an angle ϑ with respect to one of the planes of the crystal lattice, the neutrons are scattered through the angle 2ϑ, provided the neutron wavelenght λ satisfies the relation:

$$n\lambda = 2d \sin \vartheta \tag{1.17}$$

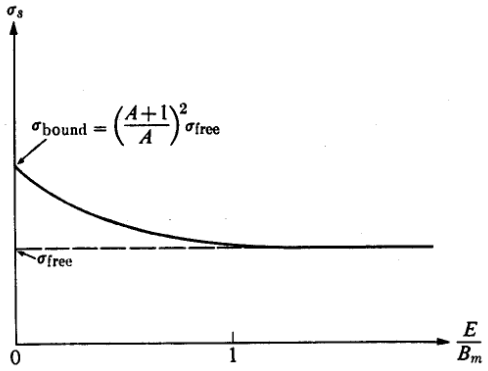

Fig. 1.4: The low energy scattering cross section at 0 K of an atom bound in a molecule as a function of E/B_m

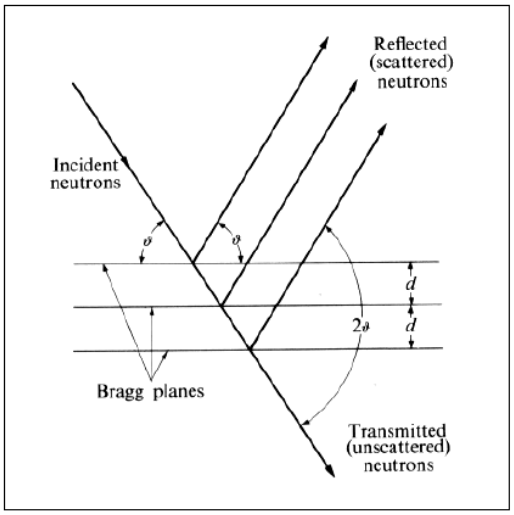

Fig. 1.5: Diagram showing Bragg reflection from three planes.

where d is the distance between adjacent Bragg planes (Fig. 1.5). As a result, the scattering cross section is much enhanced at neutron energies corresponding to the wavelenghts satisfying this relation. Moreover, according to Eq. 1.17, there is a maximum wavelenght ($\lambda_{max} = 2d$) above which Bragg scattering cannot occur. It follows that there is a mimimum energy, called the *Bragg cutoff*, below which Bragg scattering cannot occur. This cutoff and several Bragg peaks are evident at low energy in the cross section of graphite shown in Fig 1.2a.

Finally, a neutron colliding with a molecule or a lattice solid may excite one or more of its vibrational or rotational modes. In this case, since the

kinetic energy is not conserved after the interaction, we speak about *inelastic scattering*. This kind of interaction is described through the *thermal scattering law* $S(\alpha, \beta)$ in terms of two variables: the *momentum transfer* κ, which is related to α, and the *energy transfer* ϵ, which is used to define β.

$$\alpha = \frac{\hbar^2 \kappa^2}{2MkT} \qquad \beta = \frac{\epsilon}{kT} = \frac{E' - E}{kT} \tag{1.18}$$

The $S(\alpha, \beta)$ law must be defined for each material of interest from the frequency spectrum of excitations in the system: $\rho(\omega)$. Particularly, the scattering law can be written as:

$$S(\alpha, \beta) = \frac{1}{2\pi} \int_{-\infty}^{+\infty} e^{i\beta\hat{t}} e^{-\gamma(\hat{t};\, \alpha,\, \rho(\omega))} d\hat{t} \tag{1.19}$$

where $\hat{t}$ is time measured in units of $\hbar/kT$ seconds and $\gamma(\hat{t};\, \alpha,\, \rho(\omega))$ is a function depending on α and $\rho(\omega)$ (see Ref. [6] and [7]).

The double differential cross section is then determined in terms of energy and direction variation as follows:

$$\frac{d^2\sigma}{d\Omega' dE'}(E \to E', \Omega \to \Omega') = \frac{\sigma_{bound}}{4\pi kT} \sqrt{\frac{E'}{E}} S(\alpha, \beta) \tag{1.20}$$

In this regard, it is worth noting that α and β parameters both depend on temperature, therefore the $S(\alpha, \beta)$ cross sections must be calculated for the different material temperatures.

1.1.3 Fission

Nuclear fission is the process in which a heavy nucleus splits into two or more fragments with the release of considerable energy and the emission of neutrons and γ-rays. To understand the energy balance of this process we have to consider the *binding energy* of the nuclei, which is defined as:

$$B = \left(Z m_p + N m_n - M_A\right) c^2 \tag{1.21}$$

The quantity into the brackets is called *mass defect*, because it originates from the fact that the masses of nuclei (M_A) are less than the sum of the masses of the individual neutrons (m_n) and protons (m_p). In considering the binding energy per nucleon as a function of the mass number A (Fig 1.6), we observe that it decreases for $A \geqslant 50$. Therefore, when a heavy nucleus splits into fragments with higher binding energy, there is an energy gain which makes the fission process energetically favorable.

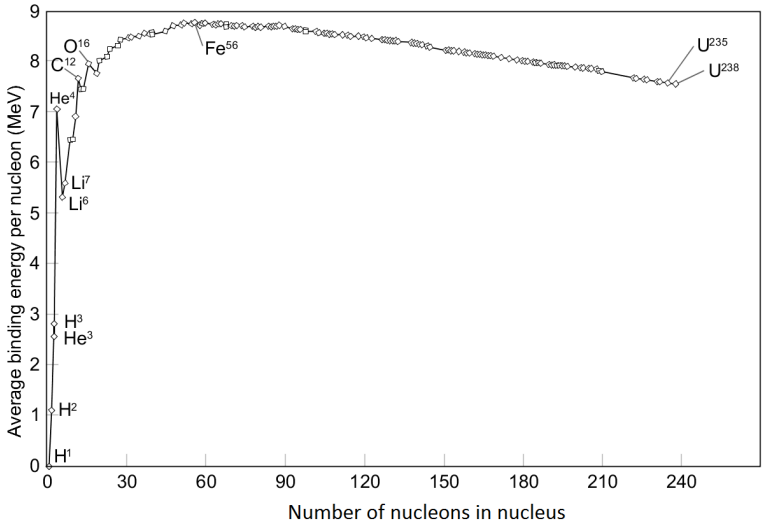

Fig. 1.6: Average binding energy per nucleon as a function of mass number.

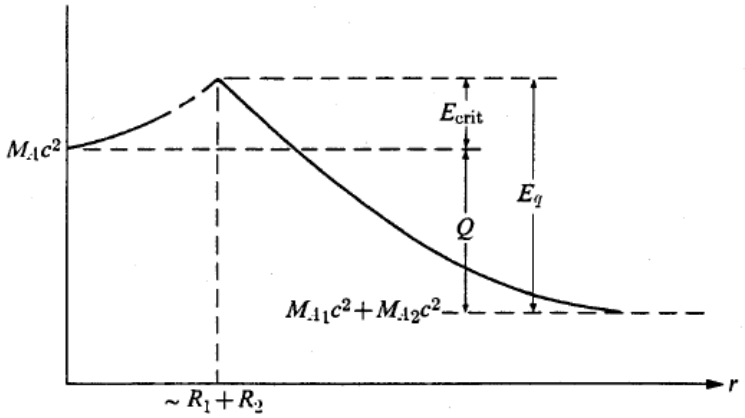

Fig. 1.7: Potential energy of fissioning nuclei as a function of the distance between the separating lobes. The critical energy (E_{crit}) and the Q-value of the reaction are represented.

However, while spontaneous fission is possible, it happens only rarely. For fission to take place with reasonable probability, a certain amount of energy, called *critical energy* (E_{crit}), must be supplied to the nucleus. In this way, the nucleus can be deformed into a double-lobe configuration in which the Coulomb repulsion prevails the nuclear binding energy. The critical energy is thus equal to the potential energy barrier which must be overcome in the nucleus (Fig. 1.7).

The most important method to supply the critical energy is neutron absorption. In this process, the compound nucleus is formed with an excitation

energy equal to $E_n + B$ (see Sect. 1.1.1). If $B > E_{crit}$, fission can be induced with neutrons of any energy and nuclei with such property are called *fissile*. Instead, nuclei requiring that neutrons must have some kinetic energy to induce fission are said to be *fissionable* (with the limitation that $E_n < 10\,\text{MeV}$).

The most important fissile isotopes are ^{235}U (which is the only one present in nature), ^{233}U, ^{239}Pu and ^{241}Pu, while ^{232}Th and ^{238}U belong to the class of fissionable nuclei together with other actinides.

When a nucleus undergoes a fission, a number of products are produced, each one carrying part of the released energy. A generic fission reaction with two fragments can be written as:

$$ {}^{A}_{Z}X + n \quad \rightarrow \quad {}^{A_1}_{Z_1}Y + {}^{A_2}_{Z_2}Z + \nu n + \gamma \tag{1.22} $$

where ν is the average number of neutrons emitted in fission reactions ($\nu = 2.43$ for ^{235}U). The majority of neutrons are emitted during the fission event and thus are called *prompt* neutrons. These neutrons are fairly energetic, being characterized by a *fission spectrum* ($\chi(E)$) with average around 2 MeV (Fig. 1.8). In addition, a small fraction of *delayed* neutrons is emitted during the radioactive decays of some fission products with half lives between 0.18 and 54.5 seconds.

The different fission fragments ${}^{A_1}_{Z_1}Y$ and ${}^{A_2}_{Z_2}Z$ are produced with specific *fission yields*, which depend on the fissioned isotope and on the neutron

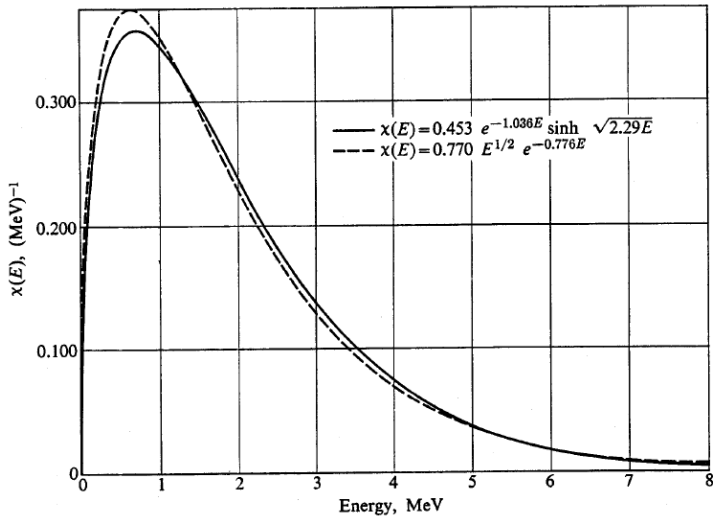

Fig. 1.8: Prompt neutron energy distribution compared for two similar functions describing the experimental data.

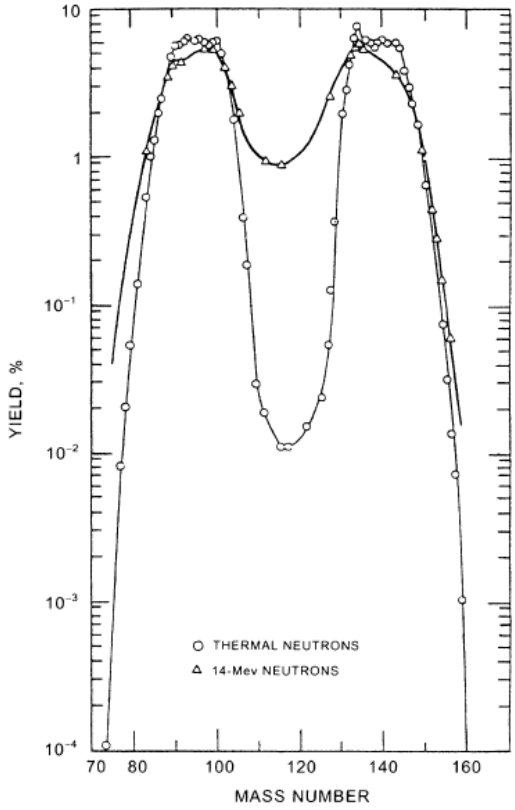

Fig. 1.9: Fission products yield as a function of their mass number in the case of thermal and 14-MeV fissions of ^{235}U.

energy. In particular, the probability that the parent nucleus splits into two fragments with similar mass is very low. In fact, fission almost always occurs in an asymmetric fashion with high probability of emitting two fission fragments with A in the ranges $85-105$ and $130-150$, respectively (Fig. 1.9).

In discussing the energy from fission, it is important to distinguish between the total energy released and the energy which can be recovered in a reactor for the production of heat. In particular, regarding the fission reaction in Eq. 1.22, the whole kinetic energy of fission products and neutrons is recoverable, together with the prompt γ-ray energy.

Moreover, the fission fragments are usually radioactive isotopes excessively "neutron rich", that is, they contain too many neutrons for stability, thus β^- is the preferential decay channel. For this reason, we also have to consider the electrons, the neutrinos and the γ-rays emitted in β decays. While the γ and β rays energies are recoverable, the neutrinos do not interact within the reactor, so their energy is completely lost. Finally, the neutrons which do not participate to new fission reactions, can be absorbed through

Reaction product	Energy (%)
Fission fragments	80
Prompt neutrons	3
Prompt γ-rays	4
Fission product β decay	4
Neutrinos	5
Neutron capture	4

Tab. 1.1: Energy release in nuclear fission.

Isotope	Energy (MeV/fission)
^{233}U	190.0 ± 0.5
^{235}U	192.9 ± 0.5
^{239}Pu	198.5 ± 0.8
^{241}Pu	200.3 ± 0.8

Tab. 1.2: Effective energy released in fission of the principal fissile isotopes by thermal neutrons.

capture reactions, with a subsequent energy release that must be taken into account.

The approximate percentages of the fission energy carried by each reaction product are shown in Tab. 1.1, while the effective recoverable energy for the fission of the main fissile isotopes by thermal neutrons is shown in Tab. 1.2 (see Ref. [4] and [8]).

1.2 Nuclear reactors operating principles

It was pointed out in the previous section that more than one neutron is emitted in a nuclear fission. In the proper environment of fissionable material, these fission neutrons are capable of inducing further fissions with the release of more neutrons, and so on. This sequence of events is known as a *chain reaction* and is the basic process of *nuclear reactors*.

1.2.1 Neutron balance and reactivity

The required condition for a stable, self-sustained chain reaction is that exactly one neutron must be produced per fission which eventually succeeds in inducing another fission. In this way, the number of fission occurring per unit

time and, as a consequence, the released power are constant. The ratio of the number of fissions in one generation to the number of fissions in the preceding generation is usually called *multiplication factor* (k or, equivalently, k_{eff} which stands for *k-effective*). We can distinguish three cases:

- $k = 1$: the number of fissions in each succeeding generation is a constant and the system is said to be *critical*;
- $k > 1$: the number of fissions increases with each generation, therefore the chain reaction diverges and the reactor is said to be *supercritical*;
- $k < 1$: the chain reaction eventually dies out and the system is called *subcritical*.

Another typical physical quantity defined for the reactor analysis is the reactivity ρ, which is related to the multiplication factor by:

$$\rho = \frac{k-1}{k} \tag{1.23}$$

therefore a steady-state critical system must have $\rho = 0$.

In order to maintain a self-sustained chain reaction, a careful balance must be established between the rate at which neutrons are produced in the system and the rate at which they disappear. We can summarize this condition through this formula:

$$\nu = k + A + L \tag{1.24}$$

where ν is the average number of neutrons per fission, while A and L indicate the average number of neutrons which are subtracted to the system through *absorption* reactions and *leaks* from the surface, respectively.

In order to characterize a multiplying system independently of its geometrical dimensions, it is usually defined the multiplication factor for an infinite system k_∞, which depends only on the material composition. For example, considering the fission of ^{235}U by thermal neutrons, it is known that $\nu = 2.43$. However, a thermal neutron absorbed by ^{235}U has 14.8% probability to be captured through (n, γ) reaction, therefore the number of neutrons effectively available for the chain reaction is 2.07. Finally, if we consider the natural uranium (which is 99.28% ^{238}U and 0.72% ^{235}U), the number of neutrons produced per each absorbed neutron decreases to 1.33, because 36% of thermal neutrons is captured by ^{238}U.

In general, due to the neutron leaks and the presence of other moderating[2] and structural materials with non-zero absorption cross section, this term is further reduced below 1, making it impossible to maintain the chain reaction. For this reason, nuclear reactors usually operate with uranium *enriched* in ^{235}U, i.e. the isotopic abundance of ^{235}U is artificially increased, thus favouring the fission reactions. Moreover, the geometric dimensions and shapes are carefully chosen so to minimize the neutron escapes as much as possible[3], and the materials used in the construction of the reactor cores have relatively small absorption cross sections.

In addition to these conditions, which can be managed in the construction phase, it must be considered that the reactivity changes over time due to the fissile material consumption (*fuel burnup*). In fact, together with the decrease of fissile isotopes, some fission products with high absorption cross sections, called *poisons*, are progressively accumulated in the fuel elements, disadvantaging the chain reaction. However, alongside these processes, neutrons can also induce reactions leading to the production of new fissile isotopes from *fertile* materials. This is the case, for example, of the neutron capture interaction with ^{238}U and ^{232}Th, which causes the production of ^{239}Pu and ^{233}U respectively. This process is called *breeding* and the presence of these new fissile isotopes must be taken into account for a correct evaluation of the system criticality.

For operating nuclear reactors, it is fundamental that the multiplication factor k is always kept exactly at 1. In order to maintain this criticality condition over time, the reactors are equipped with *control rods* containing materials with high neutron absorption cross sections. The cores are designed so that $k > 1$ in absence of the control rods. Hence, the control rods can be inserted in the core at various depths to keep the multiplication factor constantly equal to 1.

1.2.2 The diffusion of neutrons

In nuclear reactors, the neutrons propagate and interact in the core, continuously changing their position, energy and flight direction. The neutrons in this case are said to be "transported" and the study of this phenomenon is known as *transport theory*. This theory allows to derive the *Boltzmann equation*, an integro-differential equation which can be analytically solved under certain conditions. This simplified version of the transport theory is called

[2] See Sec. 1.2.3 for the definition of moderating material.

[3] Graphite reflectors surrounding the core are often employed in nuclear reactors to partially back-scatter the neutrons escaping from the core

diffusion theory and provides a good approximation to the exact transport solution. For this reason it is commonly used in many reactor design problems.

First of all, in order to derive the *diffusion equation*, some physical quantities have to be defined. The neutron field in a nuclear reactor is described through the *angular neutron density function* $N(\vec{r}, E, \vec{\omega}, t)$, which depends on the spatial coordinates $(\vec{r})$, on the neutron energy (E), on the flight direction $(\vec{\omega})$ and on the time (t).

The *neutron density function* (independent of the neutron flight direction) is simply obtained by integrating $N(\vec{r}, E, \vec{\omega}, t)$ over all solid angles:

$$n(\vec{r}, E, t) = \int_{4\pi} N(\vec{r}, E, \Omega, t)\, d\Omega \tag{1.25}$$

Multiplying this function by the module of the neutron velocity (v), we obtain the *neutron flux*, which is a fundamental physical quantity for the analysis of nuclear reactors:

$$\varphi(\vec{r}, E, t) = v\, n(\vec{r}, E, t) \qquad \left[\frac{neutrons}{\mathrm{cm}^2\,\mathrm{s}\,\mathrm{MeV}}\right] \tag{1.26}$$

It is worth noting that the neutron flux is a scalar function which does not depend on the flight direction of neutrons, but is defined to measure the combined effects of neutrons coming from different directions and interacting with matter. In fact, it is easy to show that the *interaction rate* in a certain volume V is equal to:

$$R(t) = \int_V d^3r \int dE\, \varphi(\vec{r}, E, t)\Sigma(E) \tag{1.27}$$

where $\Sigma(E)$ is the macroscopic cross section of the material contained in V.

Finally, the net flow of neutrons in a reactor is described by the *neutron current density*, which is defined as:

$$\vec{J}(\vec{r}, E, t) = \int_{4\pi} N(\vec{r}, E, \vec{\omega}, t)\, \vec{v}\, d\Omega \tag{1.28}$$

Now, in order to derive the *diffusion equation*, consider an arbitrary volume V containing mono-energetic neutrons. This model is usually called *one-velocity diffusion theory* and is based on the approximation that all neutrons have an energy equal to the average of the Maxwellian thermal distribution.

These neutrons must satisfy the *condition of continuity*, namely, the time rate of change of the total number of neutrons in V must be:

$$\frac{d}{dt}\int_V n(\vec{r},t)\,dV = \text{production rate} - \text{absorption rate} - \text{leakage rate} \quad (1.29)$$

The production of neutrons can be represented by a *source distribution function* $S(\vec{r},t)$, which is equal to the number of neutrons emitted per $\text{cm}^3 \cdot \text{s}$ at the point $\vec{r}$ and at time t. The absorption rate, instead, can be written in terms of the neutron flux, while the leakage of neutrons can be defined from neutron current density vector, because $J(\vec{r},t)\cdot\hat{n}$ is equal to the net rate of flow through a unit area normal to $\hat{n}$ at $\vec{r}$. Therefore, Eq. 1.29 can be written as:

$$\frac{d}{dt}\int_V n(\vec{r},t)\,dV = \int_V S(\vec{r},t)\,dV - \int_V \Sigma_a(\vec{r})\phi(\vec{r},t)\,dV - \int_A \vec{J}(\vec{r},t)\cdot\hat{n}\,dA \quad (1.30)$$

Exploiting the divergence theorem to transform the leakage term in a volume integral, the following equation is obtained for the integrands:

$$\frac{\partial n(\vec{r},t)}{\partial t} = S(\vec{r},t) - \Sigma_a(\vec{r})\phi(\vec{r},t) - \vec{\nabla}\cdot\vec{J}(\vec{r},t) \quad (1.31)$$

This is called *equation of continuity* and is of central importance in the reactor theory.

When the flux, current and sources are all independent of time, a system is said to be in a *steady state*. In this case, Eq. 1.31 reduces to:

$$\vec{\nabla}\cdot\vec{J}(\vec{r}) + \Sigma_a(\vec{r})\phi(\vec{r}) - S(\vec{r}) = 0 \quad (1.32)$$

which is known as the *steady state equation of continuity*. On the other hand, if the neutron density and the flux are independent of position, $\vec{\nabla}\cdot\vec{J} = 0$ and Eq. 1.31 becomes:

$$\frac{dn(t)}{dt} = S(t) - \Sigma_a\phi(t) \quad (1.33)$$

If we exclude the latter case, the equation of continuity has two unknown functions[4]: $\phi(\vec{r},t)$ and $\vec{J}(\vec{r},t)$. Therefore, to solve this equation, a relation between the flux and the neutron current has to be found.

In the diffusion theory, this relation is provided by the *Fick's law*, which was originally used to describe diffusion phenomena in liquids and gases. The basic idea is that the current is proportional to the negative spatial

[4] Note that $n(\vec{r},t)$ can be expressed in terms of the neutron flux using Eq. 1.26.

gradient of the density, i.e. the neutrons move from high density to low density regions. Therefore, the Fick's law is written as:

$$\vec{J}(\vec{r},t) = -D(\vec{r})\vec{\nabla}\phi(\vec{r},t) \tag{1.34}$$

where $D(\vec{r})$ is called *diffusion coefficient*. In the hypothesis of isotropic scattering in the laboratory coordinate system, it can be shown that $D(\vec{r}) = \Sigma_s(\vec{r})/3\Sigma_t^2(\vec{r})$.

Exploiting the Fick's law and assuming that neutrons diffuse in a homogeneous medium (hence the diffusion coefficient is independent of position $\vec{r}$), the leakage term in the equation of continuity becomes:

$$\vec{\nabla}\cdot\vec{J}(\vec{r},t) = -\vec{\nabla}\cdot\left[D\vec{\nabla}\phi(\vec{r},t)\right] = -D\nabla^2\phi(\vec{r},t) \tag{1.35}$$

Finally, substitution of this term into Eq. 1.31 yields to the *neutron diffusion equation*:

$$\frac{1}{v}\frac{\partial\phi(\vec{r},t)}{\partial t} = S(\vec{r},t) - \Sigma_a\phi(\vec{r},t) + D\nabla^2\phi(\vec{r},t) \tag{1.36}$$

The solution of this equation allows to determine the neutron flux spatial distribution for many different core geometries and is also exploited for the analysis of reactor dynamics when considering non-steady state systems.

1.2.3 Thermalization and neutron flux spectrum

In the previous section, the diffusion of mono-energetic neutrons was discussed. This model can be successfully applied to describe the space distribution of the thermal neutron flux component in nuclear reactors, however it is not suitable for the analysis of the neutron flux energetic spectrum.

In nuclear reactors, neutrons by fissions are produced with an average energy of about 2 MeV (see Fig 1.8). However, since the fissile isotope ^{235}U has a fission cross section with the characteristic $1/v$ behavior, it is convenient to slow down neutrons in order to increase the probability of fission reactions. The nuclear reactors exploiting this solution are called *thermal reactors*, because neutrons are slowed down to thermal energies (0.025 eV at room temperature). This process, called *thermalization*, is achieved by means of materials called *moderators*, such as water or graphite, able to thermalize a neutron with a relatively small number of collisions and characterized by high elastic scattering and low absorption cross sections.

In order to describe the thermalization process and analyze the neutron flux spectrum, it is convenient to define a cutoff energy E_m in such a way that,

for interactions at energies above E_m, the nuclei of the system can be assumed to be free. This is generally true for energies above 1 eV, for which the chemical binding effects are negligible. Therefore, in the energy region above E_m −called the *moderating* region− the classic elastic scattering model can be applied to describe the slowing down process.

Indicating with E and E' the neutron initial and final energy respectively, it can be demonstrated −by applying the energy and momentum conservation laws− that:

$$\frac{E'}{E} = \frac{A^2 + 2A\cos\theta + 1}{(A+1)^2} \tag{1.37}$$

where θ is the scattering angle in the center-of-mass frame and A the mass of the nucleus, assumed initially at rest. In particular, we can identify two limiting cases: if $\theta = 0$ the scattering has not happened and $E' = E$, as expected; on the other hand, if $\theta = \pi$ a head-on collision occurs, causing the maximum energy loss:

$$\frac{E'}{E} = \left(\frac{A-1}{A+1}\right)^2 \equiv \alpha \tag{1.38}$$

According to Eq. 1.38, α is equal to zero when $A = 1$ (i.e. for hydrogen) and increases to unity with increasing A. It is so evident that a neutron loses all its energy in a single head-on collision with a hydrogen nucleus, while for scattering with all other nuclei it can lose at most a fraction of its original energy. For example, α is 0.716 for carbon, so neutrons can lose at most only 28.4% of their energy in an elastic collision with a carbon nucleus. To summarize, the maximum fractional energy loss in a single elastic collision decreases with increasing mass of the struck nucleus.

It is now important to consider where in the interval from αE to E the energy of the scattered neutron is likely to fall. In general, for neutron energies below the MeV-region it is correct to assume that the scattering is isotropic in the center-of-mass system, therefore the energy of the scattered neutron will be uniformly distributed between αE and E:

$$P(E \to E')dE' = \begin{cases} \dfrac{1}{E(1-\alpha)} & \alpha E < E' < E \\ 0 & E' < \alpha E \end{cases} \tag{1.39}$$

This implies that the average energy loss is equal to $E(1-\alpha)/2$ and proportional to the energy of the neutron before the collision.

In order to describe the energy dependence of the neutron flux in the moderating region, it is easier to begin with the case of neutron slowing

down in hydrogen. To simplify the problem, consider an infinite, homogeneous medium containing uniformly distributed sources, emitting neutron with energy E_0 at the constant rate of S neutrons per $\text{cm}^3 \cdot \text{s}$. In this way, all the space and time dependences of the neutron flux can be ignored. It will also be assumed that the medium does not absorb neutrons (this is true for hydrogen, whose absorption cross section is negligible in the resonance region).

The interaction rate per unit volume ($F(E)$, also called *collision density*) and the neutron flux in hydrogen can be determined by considering the scattering of neutrons into and out of an energy interval dE centered at the energy E.

Neutrons arrive in dE as the result of collisions that occur at higher energies involving both the source neutrons and those neutrons that have had one or more collisions but whose energy E' is still above E (Fig 1.10). From Eq. 1.39, since $\alpha = 0$, the probability that one of these neutrons will be scattered into dE is:

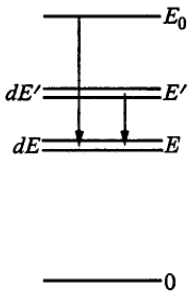

Fig. 1.10: Diagram for slowing down process analysis.

$$P(E' \to E)dE = dE/E' \tag{1.40}$$

with $E' = E_0$ in the case of the source neutrons. Since in the steady state the number of neutrons scattered into dE must be equal to the number scattered out, it follows that the collision density in the interval dE is given by:

$$F(E)dE = S\frac{dE}{E_0} + \int_E^{E_0} \frac{dE}{E'} F(E')dE' \tag{1.41}$$

where $F(E')dE'$ are, by definition, the scattering collisions per $\text{cm}^3 \cdot \text{s}$ in the interval dE' at the energy E'.

This equation can be solved by eliminating dE from both sides and by differentiating with respect to E, obtaining the following solution:

$$F(E) = \frac{S}{E} \tag{1.42}$$

Finally, the energy-dependent flux $\phi(E)$ can be determined exploiting the collision density definition:

$$F(E) = \Sigma_s(E)\phi(E) \tag{1.43}$$

It follows that:

$$\phi(E) = \frac{S}{E\Sigma_s(E)} \tag{1.44}$$

While Eq. 1.44 is strictly correct only for an infinite hydrogen medium, it is often used to give an approximate estimate of the energy-dependent flux in finite hydrogenous systems such as water-moderated reactors. In this regard it is interesting to note that $\phi(E)$ is independent of the energy of the source neutrons E_0; moreover, in the case that Σ_s is constant in the moderating energy region, the neutron flux is proportional to $1/E$.

When passing to consider moderators with $A > 1$, the fact that a neutron cannot lose all its energy in a single collision, leads to some complications, because it is necessary to classify the neutrons according to the number of times they have collided in reaching dE. However, this approach is really necessary only near the energy (E_0) of source neutrons. At energies well below E_0 (i.e. $E \leqslant \alpha^3 E_0$), which is also known as the *asymptotic energy region*, it is possible to obtain a simple expression for the collision density, because source neutrons do not scatter directly into this energy region:

$$F(E) = \int_E^{E/\alpha} \frac{F(E')dE'}{(1-\alpha)E'} \tag{1.45}$$

The solution of this equation is the following function, where C is a constant to be determined:

$$F(E) = \frac{C}{E} \tag{1.46}$$

To find C it is necessary to introduce a variable, called *lethargy*, which is defined as:

$$u = \ln \frac{E_0}{E} \tag{1.47}$$

where E_0 is an arbitrary energy, usually chosen to be the maximum energy of the neutrons in the system, so that u is positive definite[5]. The *average increase in lethargy per collision* (ξ) is an important parameter which can be calculated as:

$$\xi = \int_{\alpha E}^{E} \ln\left(\frac{E}{E'}\right) P(E \to E')dE' = 1 + \frac{\alpha}{1-\alpha}\ln\alpha \tag{1.48}$$

[5] The reason why it is convenient to introduce the lethargy is that $du = -dE/E$, therefore a constant increment of lethargy corresponds to a constant fractional energy decrement, which is the physical condition characterizing the neutron slowing down process.

in the hypothesis of isotropic scattering in the center-of-mass frame. Now, if we consider the *slowing-down density* function $q(E)$, defined as the number of neutrons per cm^3 whose energy falls below E per second, it can be shown that q is independent of the neutron energy and is equal to:

$$q = C\xi \tag{1.49}$$

In the absence of absorption, and since no neutrons leak from an infinite system, the slowing-down density must be equal to the source density ($q = S$), otherwise there would clearly be an accumulation of neutrons somewhere between $E = 0$ and $E = E_0$. From Eq.1.43 and Eq.1.46, the collision density and the energy-dependent flux result:

$$F(E) = \frac{S}{\xi E} \qquad \phi(E) = \frac{S}{\xi E \Sigma_s(E)} \tag{1.50}$$

being independent of the energy of the source neutrons and proportional to $1/E$ in the case that Σ_s is constant.

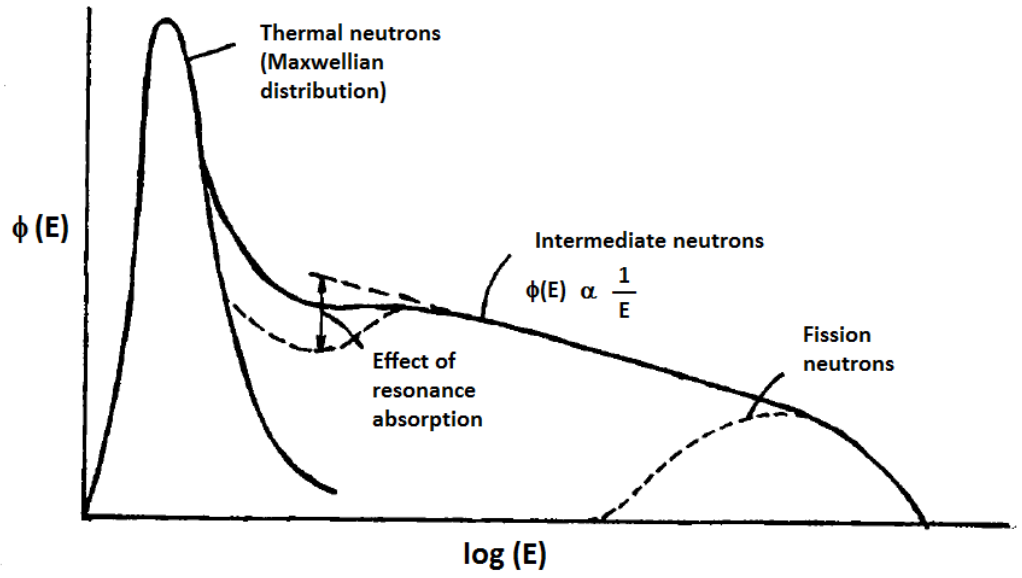

Fig. 1.11: Schematic drawing (not to scale) of the neutron flux spectrum, representing the three main energy regions of thermal, intermediate and fast neutrons. It is interesting to note that in the region between thermal and intermediate neutrons, the spectrum exhibits a deformation if the resonance absorption is not negligible.

After the analysis of the thermalization process, it is now possible to provide a qualitative description of the neutron flux energy spectrum characterizing thermal reactors. In general, the energy spectrum can be subdivided in three main regions characterized by peculiar functional shapes. In this respect, it should be pointed that at the boundaries between two energy regions, the flux spectrum assumes hybrid shapes so as to be a continuous function of energy (Fig 1.11).

In the thermal energy region it can be shown using statistical mechanics that the neutron flux is *Maxwellian*:

$$\phi(E) = \frac{2\pi n}{(\pi kT)^{\frac{3}{2}}}\sqrt{\frac{2}{m}}Ee^{-\frac{E}{kT}}dE \tag{1.51}$$

where n is the total number of thermal neutrons.

In the intermediate moderating region, if the absorption rate is negligible with respect to the scattering, it has just been demonstrated that:

$$\phi(E) \propto \frac{1}{E} \tag{1.52}$$

Finally, in the MeV region of fast neutrons, the neutron flux follows the distribution of the prompt neutrons spectrum. In particular, the fission spectrum can be described by the function:

$$\chi(E) = 0.770\sqrt{E}e^{-0.776E} \tag{1.53}$$

in which the dominant term describing the trend of the right tail is the exponential decreasing function.

1.2.4 Reactor kinetics

In this section, the behavior of the reactor in noncritical condition will be presented with some detail, arriving at the formulation of the so called *"inhour equation"*, which is fundamental for the measurement of the system reactivity ρ. This subject is usually called *reactor kinetics* or *reactor dynamics*.

In general, a reactor can become supercritical or subcritical as a consequences of some changes in the system, such as:

- Control rod motion
- Fuel *burnup* and production of *poisons*
- Temperature changes

Group	Half-life (seconds)	Decay constant $\lambda_i(s^{-1})$	Yield (neutrons per fission)	Fraction β_i
1	55.72	0.0124	0.52×10^{-3}	0.215×10^{-3}
2	22.72	0.0305	3.46×10^{-3}	1.424×10^{-3}
3	6.22	0.111	3.10×10^{-3}	1.274×10^{-3}
4	2.30	0.301	6.24×10^{-3}	2.568×10^{-3}
5	0.610	1.14	1.82×10^{-3}	0.748×10^{-3}
6	0.230	3.01	0.66×10^{-3}	0.273×10^{-3}
				Total yield: 0.0158
				Total delayed fraction (β): 0.0065

Tab. 1.3: The delayed neutron data for ^{235}U thermal fission.

One of the most important factors affecting the dynamics of a reactor are the *delayed neutrons*. These neutrons appear long after the prompt neutrons, in approximately six well-defined distinct groups, each with its own characteristic energy and half-life. The yields of delayed neutrons per fission and the corresponding fractions (β_i) of the total emitted neutrons are listed in Tab. 1.3 for ^{235}U thermal fission.

Although the fraction of delayed neutrons is very small, they are fundamental for the control of nuclear reactors. To understand their importance, it is instructive to consider the response of an infinite homogeneous reactor to a change in its multiplication factor in the absence of the delayed neutrons. Let l_p be the *prompt neutron lifetime*, that is the average time from the emission and the absorption of a prompt neutron. Since the absorption of a prompt neutron initiates a new generation of fission neutrons, l_p is also the average time between successive generations in the chain reaction, therefore the fission rate l_p seconds later will be:

$$N_F(t + l_p) = k_\infty N_F(t) \tag{1.54}$$

However, applying a first order series expansion:

$$N_F(t + l_p) \approx N_F(t) + l_p \frac{dN_F(t)}{dt} \tag{1.55}$$

it follows that $N_F(t)$ is determined by the equation:

$$\frac{dN_F(t)}{dt} \approx \frac{k_\infty - 1}{l_p} N_F(t) \tag{1.56}$$

The solution for the fission rate is therefore:

$$N_F(t) = N_F(0) e^{t/T} \tag{1.57}$$

where T is called the *period* of the reactor, defined as:

$$T = \frac{l_p}{k_\infty - 1} \tag{1.58}$$

In a thermal reactor, l_p is the sum of the slowing-down time t_s and the diffusion time t_d. Since $t_s \ll t_d$, it follows that $l_p \approx t_d$, which is of the order of 10^{-4} seconds in a homogeneous mixture of H_2O and ^{235}U. Considering that the multiplication factor k_∞ is increased only by 0.1%, that is from 1.000 to 1.001, it follows from Eq. 1.58 that:

$$T = \frac{10^{-4}\text{s}}{1.001 - 1} = 0.1 \text{ s} \tag{1.59}$$

This is a very short period: in one second the reactor would pass through 10 periods, and the fission rate (and consequently the power) would increase by a factor $e^{10} = 2.2 \times 10^4$. A reactor with such short period would be impossible to control.

However, if we consider the delayed neutrons, the mean lifetime (l) of all fission neutrons is calculated as:

$$l = (1 - \beta)l_p + \sum_{i=1}^{6} \frac{\beta_i}{\lambda_i} \tag{1.60}$$

where β is the total fraction of delayed neutrons and λ_i are the decay constants of the precursors to the ith delayed group. Using the values of Tab. 1.3, l is found to be 0.085 s, which corresponds to a period $T = 85$ s in case of 0.1% change in k_∞. With this period, the reactor can be easily controlled by the motion of control rods. It is so evident from this example that the mean generation time and reactor period are determined very largely by the small fraction of delayed neutrons rather than by the prompt neutrons.

In the case of an infinite homogeneous thermal reactor, in which the fuel is uniformly mixed with the moderator, the neutron flux is independent of position, therefore the equation of continuity for the thermal flux ($\phi_T(t)$) can be written as (see Eq. 1.33):

$$\frac{1}{v}\frac{d\phi_T(t)}{dt} = S(t) - \bar{\Sigma}_a \phi_T(t) \tag{1.61}$$

According to the thermalization model explained in the previous section, the source term $S(t)$ for thermal neutrons is equal to the thermal slowing-down

density function $q_T(t)$, which represents the number of neutrons per $\mathrm{cm}^3 \cdot \mathrm{s}$ slowed down to thermal energies after some scattering interaction. Moreover, dividing both equation members by the average thermal absorption cross section $\bar{\Sigma}_a$, the term $1/\bar{\Sigma}_a v$ is equal to the mean diffusion time of a neutron before it is absorbed (t_d) and the equation becomes:

$$t_d \frac{d\phi_T(t)}{dt} = \frac{q_T(t)}{\bar{\Sigma}_a} - \phi_T(t) \tag{1.62}$$

The function $q_T(t)$ includes the contributions of both prompt and delayed neutrons. Overall, there are $\epsilon\bar{\Sigma}_f\phi_T(t)$ fissions[6] per $\mathrm{cm}^3 \cdot \mathrm{s}$, of which the fraction $(1-\beta)$ are prompt and β are delayed.

As a result, the total number of fast fission neutrons are produced per $\mathrm{cm}^3 \cdot \mathrm{s}$ is:

$$\nu\epsilon\bar{\Sigma}_f\phi_T(t) \tag{1.63}$$

In an infinite system, the leakage term is zero, therefore the number of neutrons which actually succeed in slowing down to thermal energies is $p\nu\epsilon\bar{\Sigma}_f\phi_T(t)$, where p is the so called *resonance escape probability*, i.e. the probability that a neutron is not absorbed while it is slowed down through the energy region of the cross section resonances. Then, considering that the ratio between the number of thermalized neutrons and the number of absorbed thermal neutrons is equal to the multiplication factor k_∞, we can write the following identity:

$$p\nu\epsilon\bar{\Sigma}_f\phi_T(t) = k_\infty\bar{\Sigma}_a\phi_T(t) \tag{1.64}$$

Therefore, the neutron prompt component of the source term $q_T(t)$ is equal to:

$$(1-\beta)k_\infty\bar{\Sigma}_a\phi_T(t) \tag{1.65}$$

Considering the delayed neutrons, if $C_i(t)$ is the concentration in atoms/cm^3 of the i^{th} precursor group and λ_i the corresponding decay constant, then $\lambda_i C_i(t)$ atoms decay per $\mathrm{cm}^3 \cdot \mathrm{s}$. Hence, one delayed neutron is emitted with the decay of each precursor and will be thermalized with probability p.

Summarizing, the total slowing-down density from both prompt and delayed neutrons is:

$$q_T(t) = (1-\beta)k_\infty\bar{\Sigma}_a\phi_T(t) + p\sum_{i=1}^{6}\lambda_i C_i(t) \tag{1.66}$$

[6] $\bar{\Sigma}_f$ is the average thermal fission cross section, while ϵ is the *fast-fission factor*, i.e. the ratio of the total number of neutrons produced in *all* fission (fast and thermal on both fissile and fissionable nuclei), to the number produced by thermal fissions alone.

Inserting this result into Eq. 1.62 we obtain:

$$[(1-\beta)k_\infty - 1]\,\phi_T(t) + \frac{p}{\bar{\Sigma}_a}\sum_{i=1}^{6}\lambda_i C_i(t) = t_d\frac{d\phi_T(t)}{dt} \tag{1.67}$$

From the above discussion, the rate at which the neutrons of each group are formed is equal to:

$$\beta_i\frac{k_\infty}{p}\bar{\Sigma}_a\phi_T(t) \tag{1.68}$$

Therefore, each group concentration $C_i(t)$ must satisfy the equation:

$$\frac{dC_i(t)}{dt} = \beta_i\frac{k_\infty}{p}\bar{\Sigma}_a\phi_T(t) - \lambda_i C_i(t) \tag{1.69}$$

Equations 1.67 and 1.69 are a set of seven coupled, linear, first-order differential equations with constant coefficients, which must be solved for $\phi_T(t)$.

To solve this system, we look for solution functions of the type:

$$\begin{cases} \phi_T(t) = Ae^{\omega t} \\ C_i(t) = C_i e^{\omega t} \end{cases} \tag{1.70}$$

where A, C_i and ω are constants to be determined. The general solution of the problem will be finally given by the linear combination of all possible solutions.

Substituting the expressions of $\phi_T(t)$ and $C_i(t)$ into Eq. 1.69, the following expression is obtained:

$$C_i = \frac{\beta_i\, k_\infty\, \bar{\Sigma}_a\, A}{p(\omega + \lambda_i)} \tag{1.71}$$

When this result is inserted in Eq. 1.67 together with the expressions in Eq. 1.70, after few calculation steps the following equation is obtained:

$$\frac{k_\infty - 1}{k_\infty} = \frac{\omega t_d}{1+\omega t_d} + \frac{\omega}{1+\omega t_d}\sum_{i=1}^{6}\frac{\beta_i}{\omega+\lambda_i} \tag{1.72}$$

The quantity on the left hand side of this equation is the reactivity ρ of an infinite reactor, therefore this equation is known as the *reactivity equation* or, equivalently, *inhour equation*.

It is possible to analyze the solutions to this equation by plotting ρ versus ω (see Fig. 1.12). In general, there are seven solutions for ω: in the case of positive ρ six solutions are negative and one is positive, while for negative values of ρ all solutions are negative.

The solution for the thermal flux may then be written as:

$$\phi_T(t) = \phi_T(0) \sum_{j=1}^{7} A_j e^{\omega_j t} \tag{1.73}$$

in which the constants A_j can be determined from the initial conditions of the reactor.

Considering for example a step change in reactivity $\Delta k_\infty = 0.001$ in an initially critical infinite ^{235}U-water reactor, it can be noted that the flux rises very suddenly at first, and then more slowly (Fig. 1.13).

Mathematically, this is due to the fact that the exponential functions in Eq. 1.73 that have negative ω_j go through rapid decays and only the term with positive ω_j survives.

Physically, this behavior is due to the fact that as soon as k_∞ is increased above unity the fission rate increases and more prompt neutrons are immediately generated, causing the initial rise in the flux. However, it must be considered that the system is actually *subcritical* as far as the prompt neutrons are concerned. In fact only $(1 - \beta)\, k_\infty$ new prompt neutrons are produced

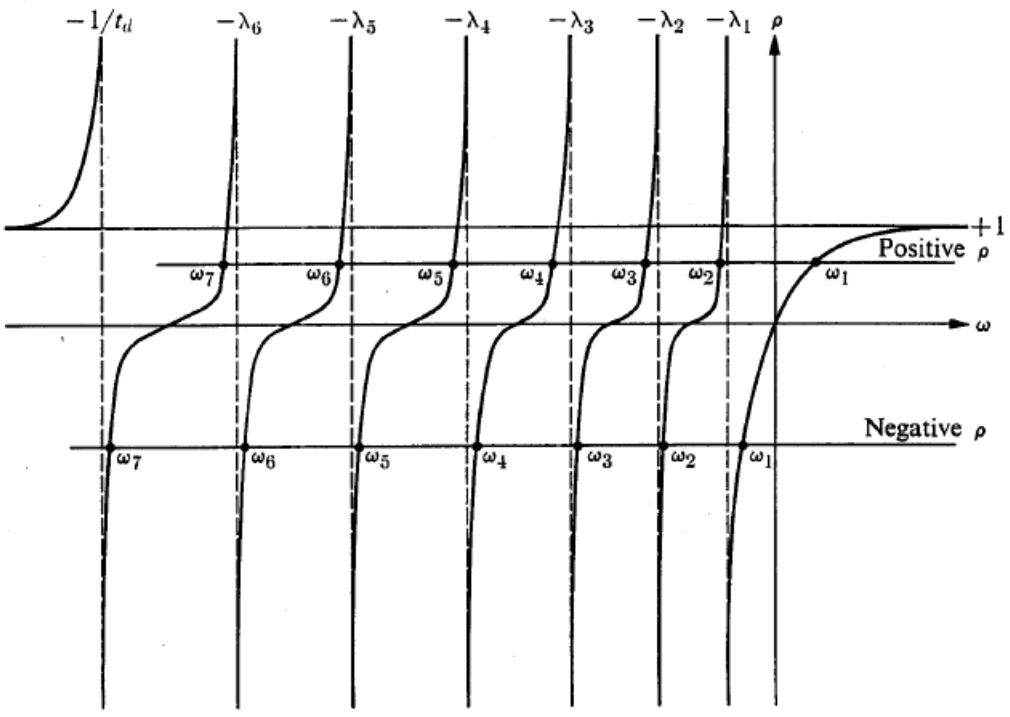

Fig. 1.12: Schematic drawing of the two sides of the inhour equation showing the seven roots for positive and negative ρ values (the figure is not drawn to scale).

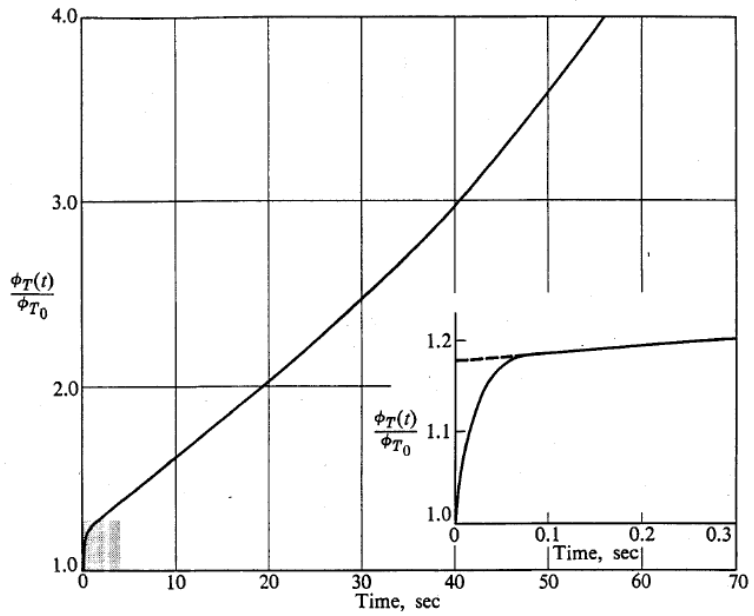

Fig. 1.13: Time behavior of thermal flux in infinite ^{235}U-fueled, H_2O-moderated thermal reactor following step reactivity insertion of 0.001.

per cycle of the chain reaction (in this example $(1-0.0065)\times 1.001 = 0.994$). Therefore, following its initial sudden rise, the flux increases more slowly as the delayed neutrons are emitted.

The results just derived for the infinite reactor also hold with little modification for a finite reactor. In particular, the flux, the slowing-down density and the precursor concentrations, which are all functions of space, are expanded in appropriate eigenfunction series to eliminate the spatial variable. The resulting equations are then identical in form with those for the infinite system and the inhour equation is proved to be valid for finite reactors, provided that the diffusion time parameter t_d is substituted with an *effective prompt neutron lifetime* ($l_{p,\,eff}$), which takes into account the thermal non-leakage probability.

The inhour equation can be applied for measuring the reactivity of the control rods in a reactor, using the so called *stable period method* [7]. This is based on the observation that, after a step reactivity insertion ($\Delta\rho$), the flux

[7] Hystorically, the stable period has been used to define a unit of reactivity called *inhour*, defined as the amount of positive reactivity required to produce a stable period of one hour (inhour stands for *inverse hour*).

eventually behaves as:

$$\phi_T(t) \sim e^{\omega_1 t} \tag{1.74}$$

because all of the exponentials except the first in Eq. 1.73 decrease in time, and the behavior of the reactor is eventually dominated by the first term. Defining the reactor *stable period* as:

$$T = \frac{1}{\omega_1} \tag{1.75}$$

it is possible to rewrite the inhour equation in the following form, taking into account that $T \gg l_p$:

$$\Delta\rho = \frac{\Lambda}{T} + \sum_{i=1}^{6} \frac{\beta_i}{1 + \lambda_i T} \tag{1.76}$$

in which Λ is the neutron invariant mean-life, defined as l_p/k. Eq. 1.76 provides a relation between $\Delta\rho$ and T, that can be used to determine the value of the step reactivity insertion by measuring the reactor period. It is interesting to note that the period is independent of the prompt neutron lifetime for periods longer than about 10 seconds (see Fig. 1.14). Thus, as would be expected, longer periods are determined almost entirely by the delayed neutrons.

In general, the small reactivity values are more conveniently expressed in terms of *pcm*, i.e. percent milli rho ($1\ pcm = 0.00001$).

However, reactivity is also commonly expressed in terms of the delayed neutrons fraction (β) through the unit of *dollars* (\$):

$$\rho\,[\$] = \frac{\rho\,[pcm]}{\beta\,[pcm]} \tag{1.77}$$

By definition, 1\$ is the reactivity necessary for a reactor to become *prompt critical*, which means that the reactor is critical without the contribution of the delayed neutrons. This is normally a dangerous situation, because the delayed neutrons play no role in governing the reactor period and the flux increases in a very short time. It must be noted that the dollar is not an absolute unit of reactivity, but depends upon both the fuel and the neutron leakage from reactors, which influence the value of β.

In this respect, when considering finite reactors, it is important to take into account that the delayed are considerably less energetic than the prompt neutrons. As a consequence, since the average leakage probability is greater for the more energetic prompt neutrons, the fraction of the neutrons slowed down to thermal energies which are delayed is somewhat increased over the fraction emitted per fission. This can be accounted for by simply defining an *effective delayed fraction* β_{eff} to be used in place of β.

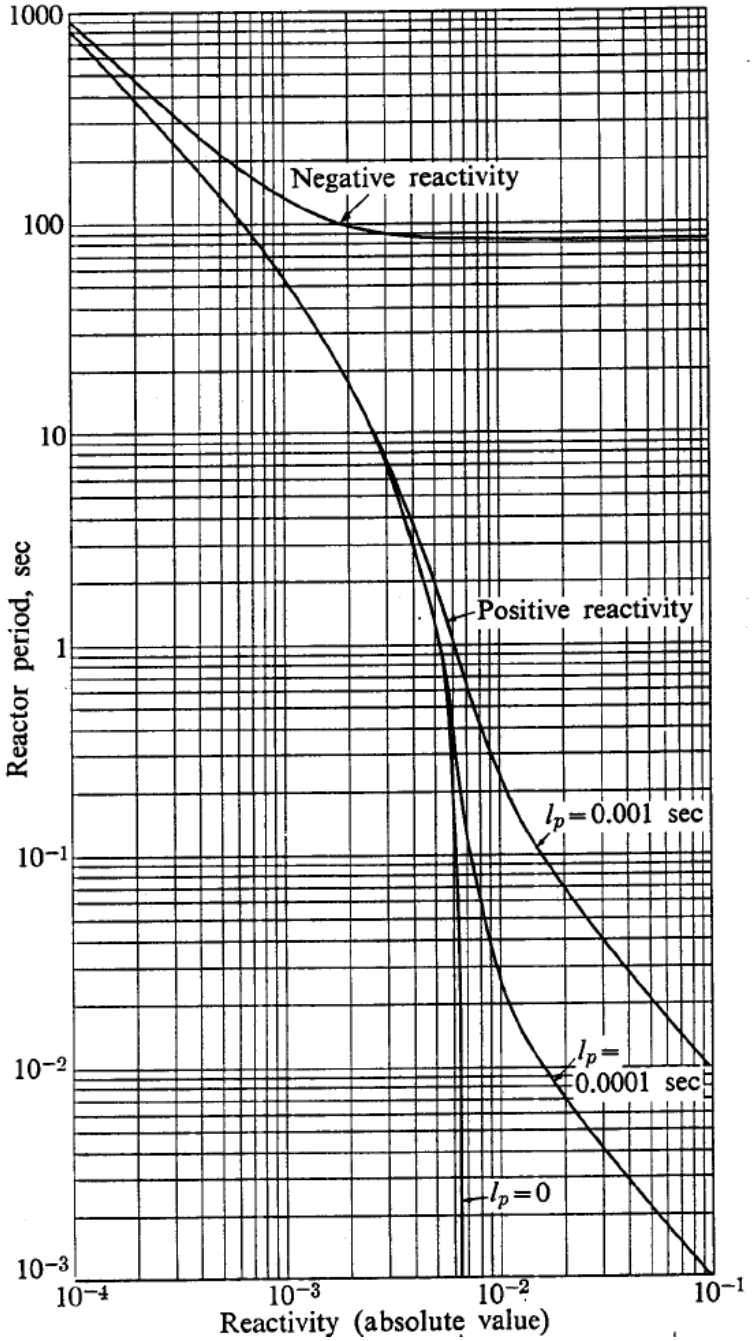

Fig. 1.14: Reactor period as a function of positive and negative reactivity for a ^{235}U-fueled reactor.

Chapter 2

Characterization of the TRIGA reactor first configuration

In this chapter, I present the benchmark analysis performed to develop a detailed Monte Carlo simulation model for the first criticality configuration of the TRIGA Mark II reactor installed at the Applied Nuclear Energy Laboratory (L.E.N.A.) of the University of Pavia.

The reactor was brought to its first criticality in 1965 and since then it has been used for several scientific and technical applications such as production of radioisotopes, nuclear activation analysis, development of boron neutron capture therapy in the medical field and reactor physics studies, thanks to the possibility of performing experimental measurements for the validation of reactor modeling codes.

To fully exploit the reactor performances, a research activity was initiated in 2007 with the aim of implementing a detailed simulation model for the reactor neutronic analysis. The MCNP Monte Carlo code was chosen for its general geometry modeling capability, correct representation of transport effects and continuous-energy cross-sections treatment.

As a first step, it was decided to implement the complete 3D model of the reactor in its first criticality configuration, characterized by "fresh" fuel. This is the reactor simplest configuration, since the fuel is not contaminated with fission reaction products and its original composition is known from the data sheets which accompanied the fuel element shipments.

A preliminary analysis of the TRIGA Mark II reactor of the Pavia University was done in the past [9] with a simplified MCNP model. To evaluate the complete reactor parameters, I have been involved in the development of a new and better refined analysis, in which all information collected in the last few years about the reactor geometries, materials and temperatures

have been introduced in the simulation model.

In the following sections, after describing the TRIGA Mark II reactor and the MCNP simulation code (Sec. 2.1 and 2.2), I will present the benchmark analysis and the experimental measurements that were performed for modeling the reactor in:

- the low power configuration with the fuel-moderator that can be simulated at room temperature, because the fuel elements are in thermal equilibrium with the water around them (Sec. 2.3);
- the full power steady-state condition (250 kW), in which the thermal effects influence the system reactivity and must be taken into account (Sec. 2.4).

2.1 TRIGA Mark II reactor description

The TRIGA (Training Research and Isotope production General Atomics) Mark II is a research reactor designed and manufactured by General Atomics. It is a pool-type reactor cooled and partly moderated by light water, with the fuel consisting of a uniform mixture of uranium (8%wt, enriched at 20%wt in ^{235}U), hydrogen and zirconium. This particular composition has a large, prompt negative thermal coefficient of reactivity, meaning that as the temperature of the core increases, the reactivity rapidly decreases. It is thus highly unlikely, though not impossible, for a nuclear meltdown to occur.

The TRIGA reactor of the University of Pavia has a nominal power of 250 kW in steady-state operation and in the past it was licensed for operating also in pulse mode, reaching the 250 MW peak power for few tens of milliseconds.

The reactor tank, which is filled with demineralized water, has a diameter of 1.98 m and a height of 6.4 m. It is surrounded by a 6.56 m high structure made of borated concrete, that serves as biological shield. The bottom part is a parallelepiped with basis (6.95×8.65) m^2 and height 3.69 m, while the upper part is an octagonal prism 2.87 m high with an apothem of 1.9 m (Fig.2.1).

Fig. 2.1: The TRIGA Mark II reactor at the Applied Nuclear Energy Laboratory of the University of Pavia.

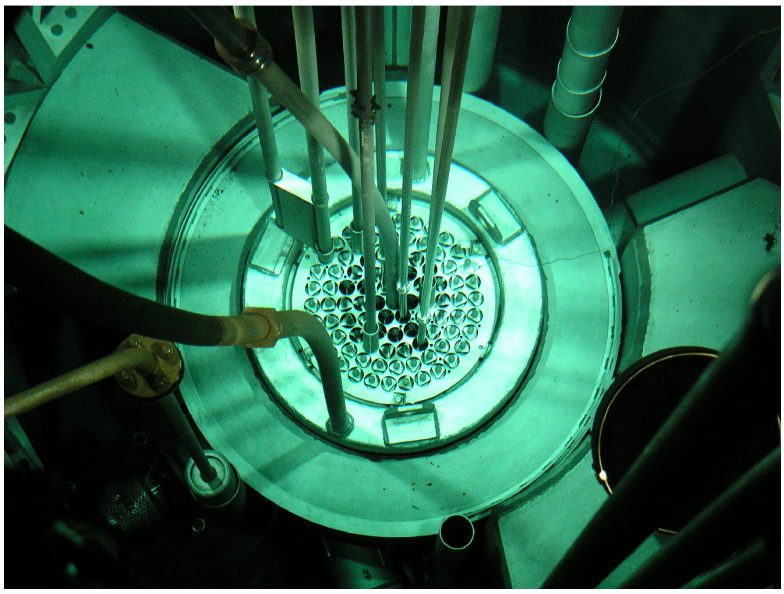

Fig. 2.2: View of the reactor core from the top.

The reactor core is placed at 60 cm from the bottom of the tank and there are about 5 m of water above it, providing an effective vertical shielding (Fig. 2.2).

The core shape is a right cylinder 44.6 cm in diameter, delimited by two aluminum grid plates (64.8 cm vertically spaced and 1.9 cm thick) which provide accurate spacing between the fuel elements (Fig. 2.3). Both grids have 90 symmetric holes distributed along 6 concentric rings labelled as A (*Central Thimble*), B, C, D, E and F, which respectively hold 1, 6, 12, 18, 24 and 30 locations. These locations can be filled either with fuel elements or different core components like *dummy elements* (i.e. graphite elements), control rods, neutron sources and irradiation channels.

A 30 cm thick radial graphite reflector surrounds the core while the axial reflector is provided by the fuel element itself in which two 10 cm thick graphite cylinders are located at the ends of the rod. Light water in the reactor tank also has the effect of a reflector (about 46 cm in the radial direction and 60 cm minimum in the axial downward direction).

2.1.1 Fuel elements

As previously mentioned, the TRIGA reactor uses fuel elements (FE) loaded with uranium and zirconium hydride (ZrH_x), where x is the atomic ratio between hydrogen and zirconium, which can vary from one FE-type to another.

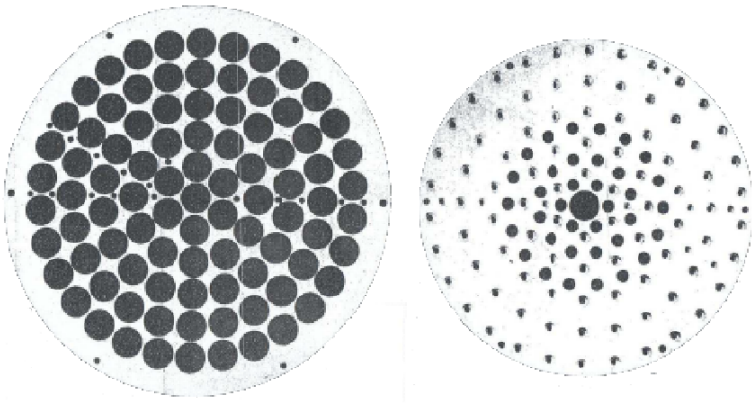

Fig. 2.3: Pictures of the top (left) and bottom (right) aluminum grid plates.

The zirconium hydride provides an effective moderation property strongly dependent on the fuel temperature: the higher the temperature, the less neutrons are moderated. This fact is due to the chemical binding effects which influence the neutron interaction with hydrogen in the crystal lattice structure of ZrH_x (Fig. 2.4).

An important characteristic of neutron inelastic scattering from zirconium hydride is that the scattered neutrons tend to gain or lose energy in amounts which are multiples of energies lying in a band centered around 0.137 eV. This feature can be readily understood qualitatively by modeling the hydrogen nuclei within the lattice as harmonic oscillators characterized by a frequency ω which determines quantum energy transfers equal to multiples of $\hbar\omega$ [10].

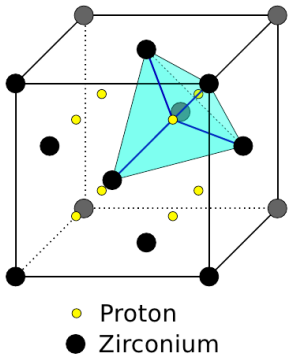

Fig. 2.4: Crystal structure of zirconium hydride. The zirconium atoms (black) are arranged in a face-centred-cubic lattice. The hydrogen atoms (yellow) are at the centre of a tetrahedron formed by atoms of zirconium.

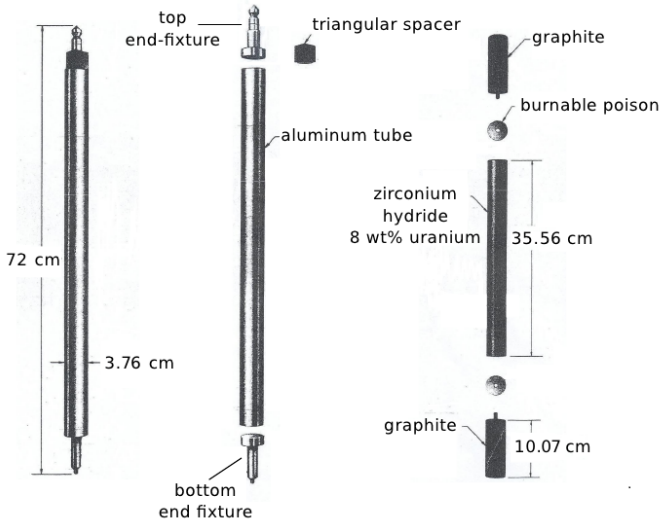

Fig. 2.5: Picture of the original fuel elements 101-type with aluminum cladding.

As the temperature increases, the excited vibrational lattice levels become more populated and, as a consequence, the probability that a neutron receives a quantum of energy is higher. As a result, the neutron flux spectrum is less thermalized and the system reactivity decreases, implying a negative thermal coefficient.

Today, the TRIGA reactor of Pavia University is loaded with fuel elements belonging to three different manufacturing series, that were designed by General Atomics over the years:

- *101-type* FE with aluminum cladding, two burnable poison[1] disks containing samarium and 1:1 atomic ratio between zirconium and hydrogen (Fig. 2.5);
- *103-type* FE with stainless steel cladding, no burnable poison disks and 1:1.6 Zr-H ratio;
- *104-type* FE with stainless steel cladding, one burnable poison disks containing molybdenum and 1:1.6 Zr-H ratio;

In addition, there are some special instrumented FE equipped with thermocouples for monitoring the fuel temperature during the reactor operation.

[1] The burnable poisons have the function of progressively releasing reactivity in the system to partially compensate the fuel burnup. They contain isotopes characterized by high absorption cross section which are progressively consumed by the reactor neutron flux.

The FE structures are described in Fig. 2.6 for the different FE types: the fuel itself is placed at the center [**A**], while the top and the bottom parts of the rod, made of nuclear graphite, play the role of axial neutron reflectors [**B**]. The burnable poison disks [**C**], if present, are placed between the fuel and the axial reflector. Everything is contained by an aluminum (0.076 cm thick) or stainless steel (0.051 cm thick) cladding [**D**] and two endcaps with appropriate pins for positioning and moving the fuel elements [**E**]. Finally, the 103 and 104-type FE have a zirconium rod at the center of the fuel meat [**F**].

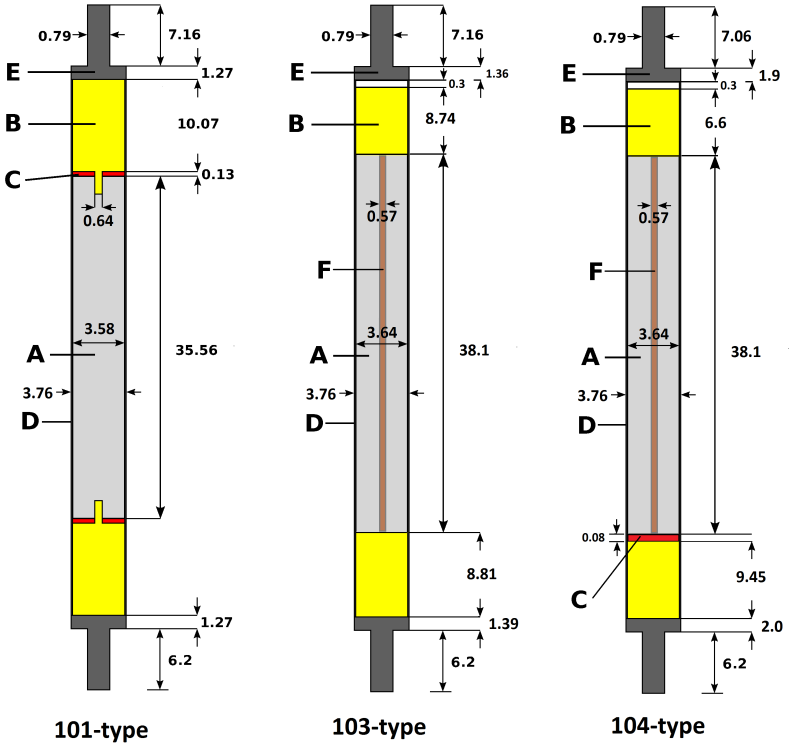

Fig. 2.6: Schematic drawing (not to scale) of the three fuel element types employed in the TRIGA Mark II reactor of the Pavia University (dimensions are given in cm units).

2.1.2 Control rods

The TRIGA Mark II reactivity control is handled by three absorbing rods, named SHIM, Regulating (REG) and Transient (TRANS). During the reactor normal operation, the SHIM rod is used for a coarse reactivity adjustment, while the REG serves to tune the multiplication factor exactly

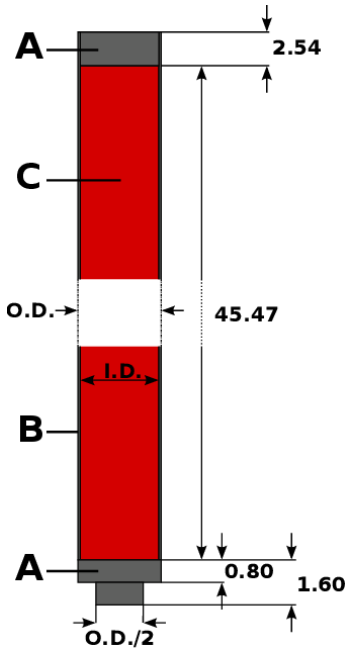

Control Rod	**I.D.** (cm)	**O.D.** (cm)
SHIM	2.85	3.18
REG	1.93	2.22
TRANS	2.21	2.54

Legend	
A	Aluminum caps
B	Aluminum cladding
C	Absorbing material

Fig. 2.7: Control rod structure. All values are measured in centimeters (cm). ***I.D.*** *stands for Inner Diameter,* ***O.D.*** *for Outer Diameter.*

at 1. The TRANS rod was employed in the past for performing the power pulses and nowadays has safety purposes only and is seldomly used during the reactor normal operation.

The three control rods are placed at angles of 120° to each other respect to the center of the core. This allows a better reactor control, because it is possible to symmetrically adjust the neutron flux in the whole reactor volume.

The SHIM and REG control rods are made of hot-pressed boron carbide powder (B_4C), while the TRANS is a solid graphite rod containing 25%wt free boron. The material and geometric descriptions of the control rods are reported in Fig. 2.7 and Tab. 2.1.

Each control rod is enclosed in an aluminum cladding connected to a mechanism which allows to move the rod at the velocity of 29 cm/min along a drilled guide tube. Moreover, an anchoring electromagnetic system allows to unhook the control rods for the rapid reactor shutdown in the case of *scram*[2] signal or plant black-out.

[2] A scram is an emergency shutdown of a nuclear reactor, achieved by inserting neutron-absorbing control rods into the core. In many cases, the scram is part of the routine shutdown procedure as well. Its etymology is usually cited as being an acronym for *safety control rod axe man*.

Boron Carbide (B_4C)	
Element or isotope	*Atomic fraction (%)*
C	20.0%
^{10}B	15.8%
^{11}B	64.2%
Density	2.52 g/cm^3

Borated Graphite	
Element or isotope	*Atomic fraction (%)*
C	72.3%
^{10}B	5.35%
^{11}B	21.7%
Density	2.23 g/cm^3

Tab. 2.1: Control rods composition and density.

2.1.3 Irradiation facilities

The TRIGA Mark II of the Pavia University is equipped with some irradiation facilities which can be used for many different experiments and purposes.

Among them, two are located inside the core: the *Central Thimble*, that is an aluminum pipe 3.8 cm in diameter located at the center of the fuel rings, and the pneumatic irradiation system, named *Rabbit Channel*, in the outer ring, which allows a rapid insertion and extraction of the samples during the irradiation for the analysis of the short-lived activated isotopes.

The *Lazy Susan* facility (Fig. 2.8) is a rotary specimen rack with 40 positions which allows the irradiation of 80 samples at the same time. It is placed in a circular well within the radial reflector and the rotation mecha-

Fig. 2.8: The Lazy Susan rotary specimen rack (left) and the Thermal Channel irradiation facility with a zoom on its internal samples holder (right).

nism allows to homogenize the neutron flux exposure of all the samples.

Recently, a new irradiation facility, named *Thermal Channel* (Fig. 2.8), was added in the pool just outside the graphite reflector (Fig. 2.9). It consists of an aluminum cylindrical container 7 cm in diameter, which can host up to 27 small polyethylene vial samples[3] placed at the core level on three planes 6 cm spaced from each other.

In addition, the TRIGA reactor of the Pavia University disposes of four horizontal beam ports penetrating the concrete shielding and extending inside the pool towards the reflector (see the horizontal section of Fig. 2.10).

Three of these channels are radial, i.e. they are directed towards the center of the core, while the fourth is tangential respect to the core region, thus it is not crossed by the direct flux of neutrons and γ-rays from the core.

Each channel is divided in two parts: the inner one is an aluminum pipe of diameter 15.2 cm, while the outer part is made of a steel tube of diameter 20.3 cm, which can be filled with shutters made of different materials to ensure a proper radiation shielding during the reactor operation.

The radial channels are slightly different to each other to provide varied irradiation conditions: one of them is piercing, i.e. there is a hole penetrating the graphite reflector which allows the sample positioning just outside the core cylinder. Another one joins the reflector in correspondence with a hole drilled in the graphite, while the last one is characterized by a thermalized

[3] The vial dimensions are 0.8 cm in diameter and 3 cm in height.

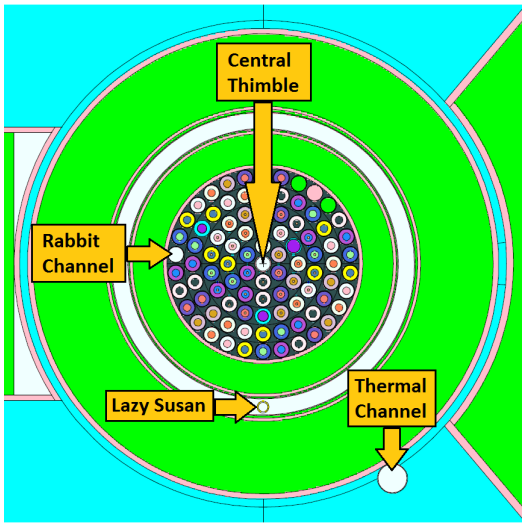

Fig. 2.9: Radial section of the TRIGA reactor core as described in the MCNP simulation model.

neutron flux, because it is in front of a reflector region filled with graphite.

Looking again at Fig. 2.10, at the right side of the reflector there is a graphite *thermal column*, which provides a flux of well-thermalized and isotropic neutrons.

On the other side, there is the *thermalizing column*. It consists of a cavity in which it is possible to insert graphite blocks with different thickness so as to obtain neutron spectra with varying levels of thermalization. The thermalizing column ends in a water pool where the samples are submerged to be irradiated mainly for biological and medical applications.

Finally, in order to perform neutron activation or other measurements within the water filling the volumes between the fuel elements, 16 holes of diameter 8 mm are drilled in the upper grid at different distances from the center of the core. During my Ph.D research activity, we projected and realized two experimental kits consisting of aluminum rods for measuring the neutron flux and the water temperature in these holes. The results of these measurements will be discussed later in this thesis.

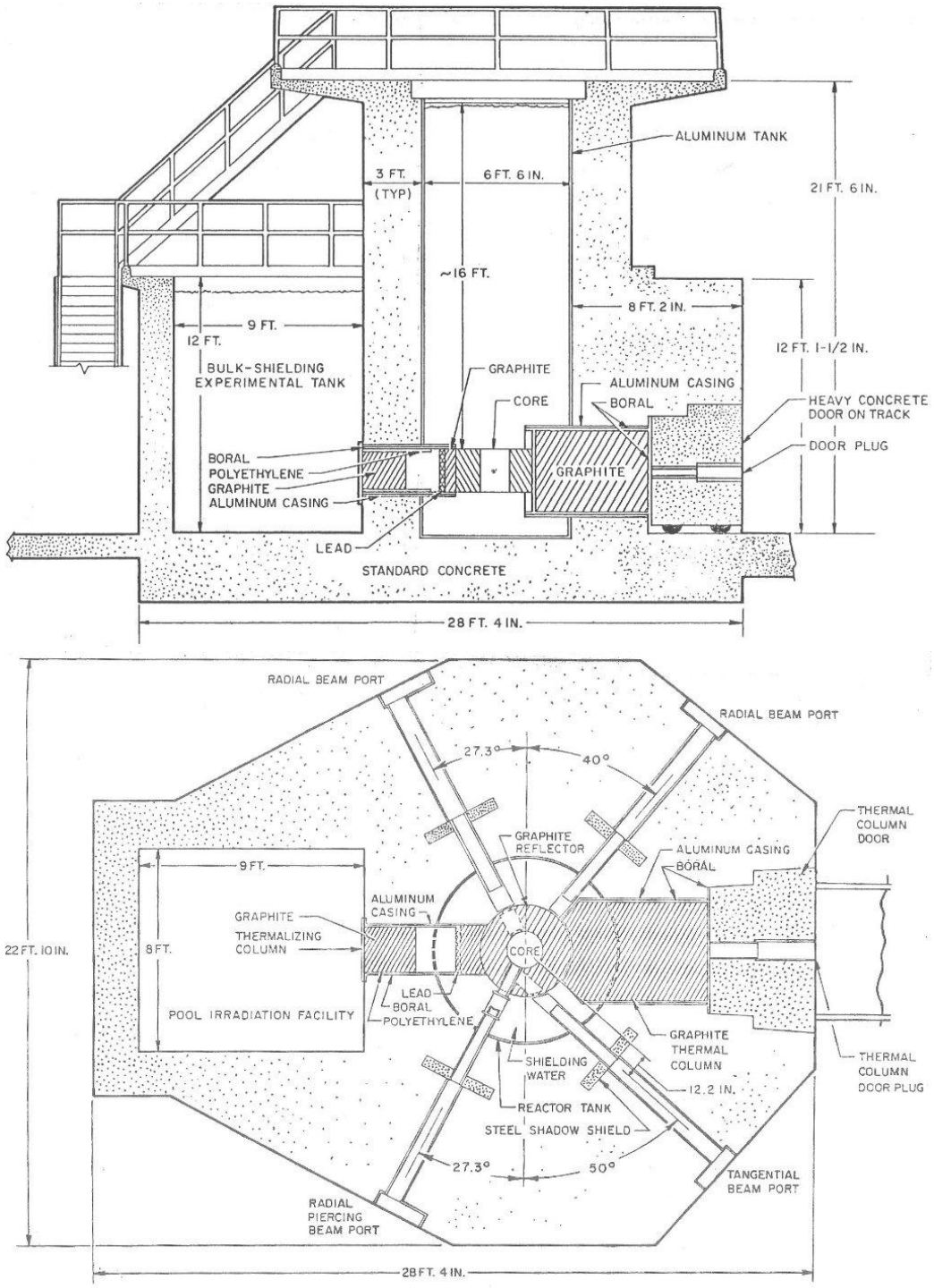

Fig. 2.10: Vertical (top) and horizontal (bottom) sections of the TRIGA Mark II reactor in Pavia.

2.2 The MCNP Monte Carlo simulation code

The simulation code that we used to develop a model for the neutronic analysis of the TRIGA reactor is MCNP (**M**onte **C**arlo **N**-**P**article transport code) [11]. This code, developed at the Los Alamos National Laboratory (LANL), is a general-purpose coupled neutron/photon/electron Monte Carlo transport code. The neutron energy regime is from 10^{-11} MeV to 20 MeV for all isotopes and up to 150 MeV for some isotopes, the photon energy regime is from 1 keV to 100 GeV, and the electron energy regime is from 1 KeV to 1 GeV.

Thanks to the capability to model arbitrary three-dimensional configuration of materials and to simulate the transport effects with a continuous-energy cross sections treatment, MCNP finds several applications in various fields, including particle physics, radiation protection, dosimetry, medical physics, detector analysis and, of course, reactor physics. In particular, MCNP is one of the reference codes in the field of nuclear reactor analysis because of its capability to evaluate the multiplication factor for critical systems.

2.2.1 Monte Carlo methods

Monte Carlo methods are very different from deterministic transport methods. Deterministic methods solve the transport equation for the average particle behavior. By contrast, Monte Carlo obtains answers by simulating individual particles and recording some aspects (*tallies*) of their average behavior. The average behavior of particles in the physical system is then inferred (using the central limit theorem) from the average behavior of the individual simulated particles.

In general, to perform a Monte Carlo simulation, it is necessary to provide the following information:

- the geometry specification;
- the description of materials, including the selection of cross-section evaluations to be used for simulating the radiation interaction with materials;
- the location and characteristics of the particle sources;
- the type of information to *tally* for providing the desired answer.

In particle transport, the Monte Carlo technique is pre-eminently realistic (a numerical experiment). It consists of actually following each of many particles from a source throughout its life to its death in some terminal category

(absorption, escape, etc.). The individual probabilistic events that comprise a transport process are simulated sequentially and the probability distributions governing these events are statistically sampled to determine the outcome at each step. In general, the number of trials necessary to adequately describe the phenomenon is quite large. For this reason, the statistical sampling process, based on the selection of pseudo-random numbers[4], is usually performed on digital computers.

It this way, Monte Carlo methods can "solve" transport problems by simulating *particle histories*, without the need to explicitly solve the transport equation. For this reason, Monte Carlo methods are well suited for solving complicated three-dimensional, time-dependent problems, because they do not require averaging approximations in space, energy, and time (unlike the deterministic methods). This is especially important in allowing detailed representation of all aspects of physical data.

2.2.2 Cross section libraries

MCNP uses continuous-energy nuclear and atomic data libraries in the Evaluated Nuclear Data File (ENDF) format [12] [13]. The ENDF formats were originally developed for use in the US national nuclear data files called ENDF/B, but today this format has become the international standard for storing the evaluated low-energy nuclear physics data and it is used by data centers in US, Europe, Japan, China, Russia, Korea and elsewhere.

The uses of the ENDF formats evolved over the years: the first few versions were largely intended for thermal-reactor applications, while today these libraries are in use for a wide variety of applications that require calculations of the transport of neutrons, photons, and charged-particles through materials. In fact, they describe the nuclear reaction cross sections, the distributions in energy and angle of reaction products, the various nuclei produced during nuclear reactions, the decay modes and product spectra resulting from the decay of radioactive nuclei, and the estimated errors for these quantities.

The modern evaluations are done by combining the experimental data with nuclear model code calculations to extend or interpolate the available data. The requirements for quality control, revision control, peer review, and data testing −that result from the goal of using the data files for calculations that could have major impacts on public health and safety− has led to putting all modern nuclear data evaluation work under the control of a few national and international agencies, including:

[4] The name "Monte Carlo" derives from the drawing of random numbers during the simulations, analogous to throwing dice in a gambling casino.

- the Cross Section Evaluation Working Group (CSEWG), which handles the US **ENDF/B** libraries [14] and the ENDF format. It is coordinated through the National Nuclear Data Center at the Brookhaven National Laboratory;
- the JEFF Working Group, which handles the european Joint Evaluated Fission and Fusion file (**JEFF**) [15]. It is coordinated through the NEA Data Bank, a part of the Nuclear Energy Agency (NEA) of the Organization for Economic Cooperation and Development (OECD);
- the Japanese Nuclear Data Committee (JNDC), which handles the Japanese Evaluated Nuclear Data Library (**JENDL**) [16]. It is coordinated through the Nuclear Data Center at the Japan Atomic Energy Agency (JAEA).

Each of these organizations has adopted the ENDF format as the common method for publishing their nuclear data libraries, but each has been able to define its own procedures for using the formats, reviewing the evaluations, and testing the results.

When performing a MCNP simulation, the user can decide which set of data libraries will be adopted. Moreover, by running parallel simulations with different cross section libraries, it is possible to evaluate if there are significant differences in the results. In any case, it is worth noting that each cross section evaluation is affected by experimental uncertainty, which could result in a systematic error affecting the simulation results. The latest cross section releases are usually accompanied by covariances data to provide information about the uncertainty associated to a specific evaluation.

In order to take into account the effects of chemical binding and crystal structure, MCNP foresees the possibility of using specific cross sections, called $S(\alpha, \beta)$, which are compiled for incident neutron energies below 4 eV and are available for only a limited number of substances and temperatures. Since the use of these cross section libraries is absolutely essential to get correct answers in problems involving neutron thermalization, $S(\alpha, \beta)$ cross sections are available for most of the materials which are usually employed in nuclear reactor cores (H_2O, D_2O, graphite, ZrH, polyethylene, aluminum, beryllium, etc.)

For the other materials, MCNP provides a thermal treatment based on the free-gas approximation, which consists of adjusting the elastic cross section at zero temperature to take into account the velocity of the target nucleus. It is worth noting that the free gas thermal treatment effectively applies to

elastic scattering only and is not used below 4 eV if the $S(\alpha, \beta)$ library is available.

Finally, the MCNP cross section libraries −including the $S(\alpha, \beta)$− are compiled at different temperatures so as to model the Doppler broadening of the resonance peaks and the thermal effects concerning the low-energy neutron interactions. If a cross section is needed for a temperature which is not available in the library, it is possible to generate a new cross section by interpolating the ones at lower and higher temperature respectively.

2.2.3 Tallies

In MCNP simulations, the request of a particular result is achieved by using the so called *tallies*, which can be related to particle current, particle flux, and energy deposition. All tallies are normalized to be per starting particle except for the case of criticality calculations, in which are normalized to be per fission neutron generation.

The definitions of *current* and *flux* used for describing the tallies come from nuclear reactor theory [3] (see also Sec. 1.2.2).

The *current tally* (labelled as F1) keeps track of the particles crossing a surface of area A during the simulation. Therefore, this tally provides an estimate of the following integral:

$$F1 = \int_t dt \int_A dA \int_{E_i} dE \int_{\Omega_j} d\Omega \, |\vec{J}(\vec{r}, E, t, \Omega) \cdot \hat{n}| \tag{2.1}$$

where the integration over time has to be interpreted as the normalization factor which keeps into account the time required for emitting the same number of simulated particles in the real physical system under analysis. The range of integration over energy and angle can be managed so as to tally the results with the desired binning. For example, if the range of integration is over all angles, the F1 tally simply counts the number of particles with any trajectory crossing the surface and thus has no direction associated with it. Alternatively, it is possible to evaluate the partial currents crossing in the positive and negative directions or to define a denser binning for distinguishing more directions.

The *flux tallies* are labelled as F2, F4, and F5 depending on whether they are evaluated for a surface A, a volume V or at a point $\vec{r}_p$. These tallies allow

to evaluate the scalar neutron flux previously defined in Eq. 1.26:

$$\begin{aligned} F2 &= \frac{1}{A}\int_t dt \int_A dA \int_{E_i} dE\, \varphi(\vec{r}, E, t) \\ F4 &= \frac{1}{V}\int_t dt \int_V dV \int_{E_i} dE\, \varphi(\vec{r}, E, t) \\ F5 &= \int_t dt \int_{E_i} dE\, \varphi(\vec{r}_p, E, t) \end{aligned} \tag{2.2}$$

The technique used to evaluate the average flux in a cell of volume V is also referred as *track length estimate*. In fact, the neutron flux, defined as $v\, n(\vec{r}, E, t)$, can be viewed as the sum of the distances travelled by the particles per unit time. Therefore, during a Monte Carlo simulation, tally F4 calculates the sum of the track lengths within the volume V.

Tally F2 evaluates the average flux on a surface with a technique that is similar to tally F4 in the limit that the cell thickness approaches to zero.

Otherwise, the tally F5 is evaluated in a different way, based on the so called *point detector next-event estimator*, which is a sort of *variance reduction* technique. In fact, for each source particle and each collision event, a deterministic estimate is made of the flux contribution by evaluating the probability that the particle will reach the point detector at $\vec{r}_p$.

Moreover, MCNP makes available special tallies for evaluating the *heating* (F6) and the *energy deposition* (F7) in a cell, and a *pulse height tally* (F8) for providing the energy distribution of pulses created in a cell that models a physical detector.

Finally, MCNP offers the opportunity of calculating any quantity of the form:

$$R = C \int \varphi(E)\, f(E)\, dE \tag{2.3}$$

where C is a normalizing factor and $f(E)$ is any product or summation of the quantities in the cross-section libraries or a response function provided by the user. For instance, by setting $f(E)$ equal to the cross section of a certain interaction and C equal to the number of target nuclei in the simulated material, it is possible to directly evaluate the interaction rate.

2.2.4 Criticality Calculations

As previously mentioned, MCNP is a Monte Carlo code which provides the opportunity to perform criticality calculations for evaluating the k_{eff} of multiplying systems. Calculating k_{eff} consists of estimating the mean number of fission neutrons produced in one generation per fission neutron started. A

generation can be thought as the life of an ensemble of neutrons from birth in fission to death by escape, parasitic capture, or absorption leading to fission. In MCNP, the computational equivalent of a fission generation is a k_{eff} cycle: fission neutrons are terminated in each cycle to provide the fission source for the next cycle.

Criticality calculations with MCNP are based on an iterative procedure called *power iteration*, which is activated through the so called *KCODE card*. After assuming an initial guess for the fission source spatial distribution and k_{eff} value, the histories of each cycle are followed to produce a source for the next fission neutron generation and to estimate a new value for k_{eff}. This procedure is repeated until the fission source distribution converges to its stationary state. At this point, tallies for reaction rates and k_{eff} values may be accumulated by running additional cycles until the statistical uncertainties have become sufficiently small.

To evaluate the multiplication factor, MCNP uses three different estimators:

1. Collision Estimator

   k^C_{eff} is evaluated by considering all the collisions occurring in a generation. It is calculated as:

   $$k^C_{eff} = \frac{1}{N} \sum_i W_i \left[\frac{\sum_k f_k \bar{\nu}_k \sigma_{f_k}}{\sum_k f_k \sigma_{t_k}} \right] \tag{2.4}$$

   where N is the nominal number of source neutrons per cycle, W_i is the weight assigned to each neutron[5], i is summed over all collisions in a cycle, k is summed over all nuclides of the material involved in the i^{th} collision and f_k is the atomic fraction for nuclide k. The quantity in square brackets is the expected number of neutrons to be produced from all fission processes in the collision.

2. Absorption Estimator

   k^A_{eff} is evaluated by considering all the absorption reactions with a fissionable nuclide as follows:

   $$k^A_{eff} = \frac{1}{N} \sum_i W_i \frac{\bar{\nu}_k \sigma_{f_k}}{\sigma_{a_k}} \tag{2.5}$$

   where i is summed over each absorption event in the k^{th} nuclide.

[5] The number of neutrons actually generated in a cycle (M) depends on the number of points selected for describing the fission source spatial distribution, which varies from one cycle to another. In order to keep constant the nominal number of source neutrons (N) a weight equal to N/M is assigned to each source particle.

3. Track Length Estimator

   k_{eff}^{TL} is accumulated every time the neutron traverses a distance d in a fissionable material cell with atomic density ρ_a. Since $\rho_a\, d\, \sum_k f_k \bar{\nu}_k \sigma_{f_k}$ is the expected number of fission neutrons produced along trajectory d, the track length estimator is defined as:

$$k_{eff}^{TL} = \frac{1}{N} \sum_i W_i \left[\rho_a\, d \sum_k f_k \bar{\nu}_k \sigma_{f_k} \right] \tag{2.6}$$

Each of these estimators is more suitable for some kind of problems. For instance, k_{eff}^{C} tends to be the best in very large systems, while k_{eff}^{A} is likely to produce the smallest statistical uncertainty of the three estimators for thermal systems with a dominant fissile nuclide. Finally k_{eff}^{TL} tends to display the lowest variance for optically thin fuel cells and fast systems. Anyhow, at the end of the simulation, MCNP provides the best evaluation for k_{eff} and the relative standard deviation by calculating a statistical combination of all three estimators.

2.2.5 Estimation of the Monte Carlo errors

Monte Carlo results represent an average of the contributions from many histories sampled during the numerical simulation of the problem. An important quantity related to the Monte Carlo results is the *statistical error* (or uncertainty). In general, for a well-behaved tally, the statistical error is proportional to $1/\sqrt{(N)}$, where N is the number of simulated histories. Therefore, it is always necessary to consider which is the best compromise between the required precision and the computer time required to simulate a sufficient number of histories.

MCNP tallies report also the estimated relative error (ϵ_r), defined to be one standard deviation divided by the estimated mean. Moreover, with the aim of reporting potential anomalies in the simulation, MCNP calculates a figure of merit (FOM) for each tally as a function of the number of histories, defined as:

$$\text{FOM} = \frac{1}{\epsilon_r^2 T} \tag{2.7}$$

where T is the computer time. The FOM should be approximately constant during the simulation, because ϵ_r^2 is proportional to $1/N$ and T is proportional to N. A sharp decrease in the FOM indicates that a seldom-sampled particle path has significantly affected the tally result and, hence, the relative error estimate. In this case, the Monte Carlo results will not have the correct

expected values and it is necessary to setting up the problem again so as to sample all regions of the phase space adequately.

In the analysis of the Monte Carlo errors, it is extremely important to consider that confidence statements derived from the statistical errors refer only to the *precision* of the Monte Carlo calculation itself and not to the *accuracy* of the result compared to the "true" physical value.

Accuracy is a measure of how close the expected value $E[x]$ is to the true physical quantity x being estimated. The difference between this true value and $E[x]$ is usually called the *systematic error*, whose evaluation requires a detailed analysis of the uncertainties in the physical data, modeling, sampling techniques, and approximations used in a simulation. For this reason, benchmark analysis with available experimental data should always be performed to check the reliability of the simulation results.

2.3 Low power reactor characterization

The first MCNP model of the TRIGA Mark II reactor of the Pavia University was developed in 2007 [17]. The complete structure of the reactor in the first criticality configuration was modeled using all information which was possible to collect from the documents stored in the laboratory where the reactor is installed (Fig 2.11).

Due to the lack of knowledge about certain parameters, some approximations had to be employed in the fuel elements and control rods description, involving both the geometry and the material composition. Moreover, the amount of samarium within the poison disks of the fuel elements was unknown at that time and this parameter was tuned so as to achieve the criticality condition in agreement with the experimental data.

In this way, it was possible to perform a preliminary benchmark analysis [9], evaluating the neutron flux and simulating the experimental tests described in the reactor First Criticality Final Report [18]. Although a good agreement was achieved between the experiments and the corresponding simulations, the approximations employed in that model inhibit the possibility of simulating the system's multiplication factor (k_{eff}) on the absolute scale.

Since this parameter represents an important benchmark in the neutronic analysis, it was necessary to implement a new and better refined model, with the ultimate goal of exploiting MCNP for simulating the full power condition, studying the fuel burnup and describing the current reactor configuration.

2.3.1 The new model for low power reactor in 1965

In the recent years, thanks to the constant interaction with General Atomics, it was possible to obtain very detailed data regarding the core components which are relevant for modeling the system with good accuracy. The technical drawings supplied by the manufacturer were consulted to define the geometry of the fuel elements and control rods. Moreover, focused searches were performed to collect precise information about the isotopic composition and the density of the different materials selected for the core components.

All these data were used to improve the MCNP reactor model of the fresh fuel, low power configuration, with the aim of fully reproducing the experimental results obtained in 1965, during the operations that followed the first reactor start-up. In particular, the analysis was focused on simulating the criticality configurations and the control rod calibrations.

In those experiments, the reactor power was kept at a minimum level (10 W), so it was possible to set the temperature of every core material to around 300 K, neglecting the thermal effects arising at full power condition.

In the original reactor configuration, the core was loaded with 61 fuel elements *101-type* and 23 graphite "dummy" elements. One compartment hosted the neutron source, while one slot was left empty (Fig. 2.12).

With respect to the previous MCNP model, the following changes have been introduced:

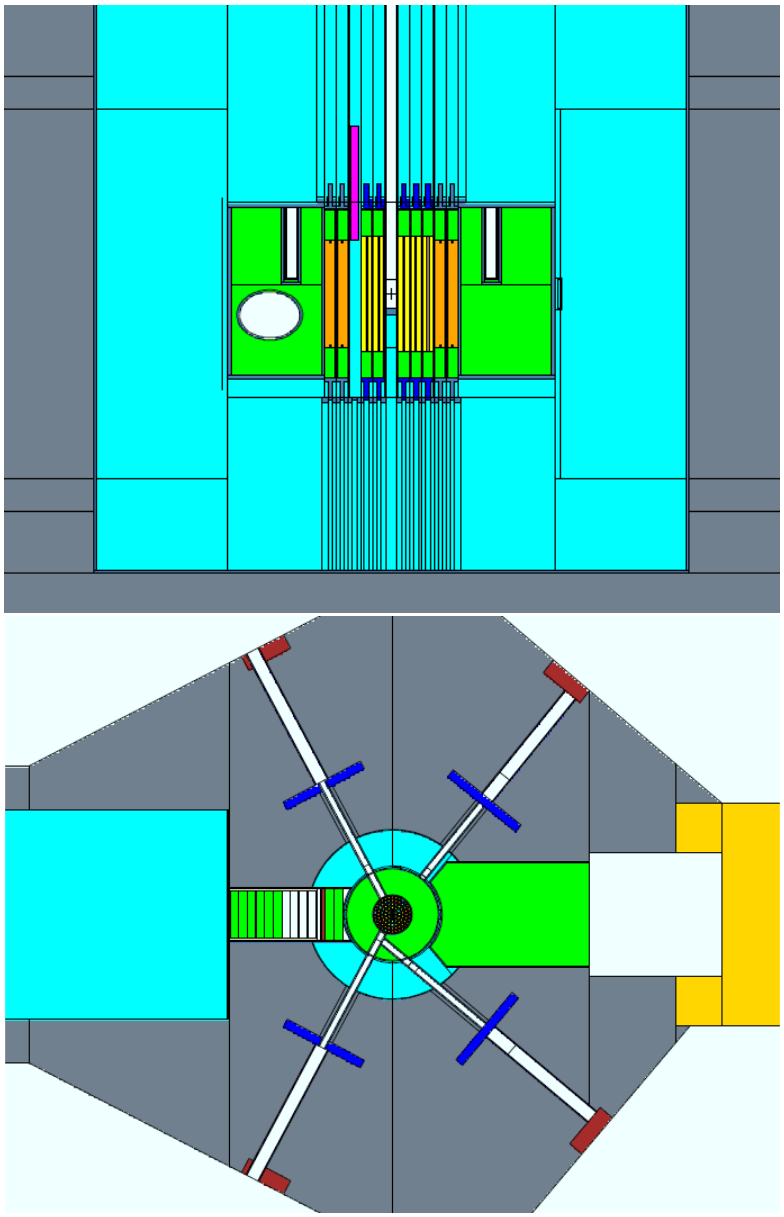

Fig. 2.11: Vertical (top) and horizontal (bottom) sections of the TRIGA Mark II reactor in Pavia as described in the MCNP simulation model.

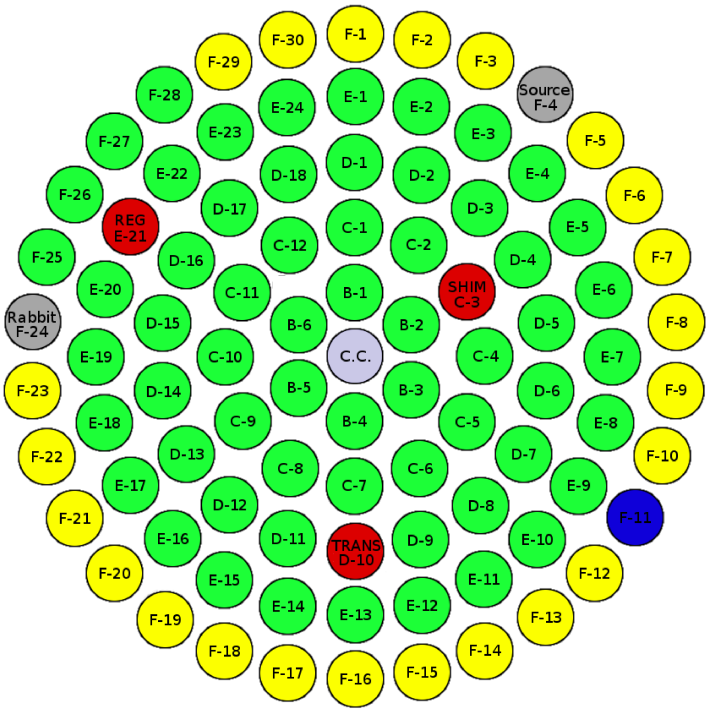

Fig. 2.12: Original core configuration. Fuel elements are represented in green, graphite rods in yellow, control rods in red and the empty slot in blue.

- the fuel enrichment in ^{235}U has been corrected so as to be $(19.75 \pm 0.05)\%$ instead of the previous 20% approximated value;
- using the data by General Atomics, the samarium mass in each poison disk has been set to 21.2 mg, corresponding to 2.90 mg of ^{149}Sm (the samarium isotope with the largest capture cross section); moreover, the disk composition has been updated so as to be a matrix of Al_2O_3 loaded with Sm_2O_3;
- the geometry of each control rod has been redefined adding the cladding and the guiding pipe; moreover, the material composition and density is now set to the nominal values reported in Tab. 2.1;
- instead of using average values, the fuel composition is defined element by element with the exact masses of uranium, zirconium and hydrogen as reported in the data sheets accompanying the fuel shipments;
- impurities have been added to the aluminum 1100F used for the cladding and to the nuclear graphite employed in the reflectors (see Tab. 2.2).

The k_{eff} variations were analyzed when changing one by one each of these parameters in the simulations. In particular, significant differences (greater than 0.5 \$) were observed when updating the uranium enrichment and the samarium content in the poison disks. The other changes caused minor variations of the order of few tenths of a dollar or less; however, when added together, they allowed to significantly increment the accuracy of the model in the evaluation of the k_{eff}.

Aluminum 1100F impurities						
Element	Si	Cu	Ga	Fe	Mg	V
%wt fraction	0.13	0.1	0.1	0.1	0.1	0.1
Element	Cr	Mn	Pb	Ca	Zr	
%wt fraction	0.02	0.01	0.01	0.001	0.001	

Nuclear graphite impurities						
Element	Fe	O	Ti	Na	Mg	Cu
%wt fraction	0.8	0.13	0.1	0.01	0.01	0.01
Element	Co	H	F	Cl	B	
%wt fraction	5.0E-3	3.7E-3	2.5E-3	2.5E-3	5.0E-5	

Tab. 2.2: Weight fractions of the impurities simulated in aluminum and nuclear graphite.

2.3.2 Criticality reactor configurations

With the aim of checking the capability of the new MCNP model to evaluate the system's k_{eff} on the absolute scale, a set of critical reactor configurations was simulated, corresponding to different positions of the control rods inside the core. In these configurations the expected value for the reactivity is $\rho = 0$ \$ ($k_{eff} = 1$).

In each simulation, the MCNP *KCODE card* was used to run criticality calculations, setting 1000 cycles (representing the neutron generations) with 10000 neutrons each, for a total of 10 million simulated neutrons. The JEFF 3.2 cross section libraries were employed and the $S(\alpha, \beta)$ thermal treatment at 300 K was used for simulating the low-energy inelastic scattering on zirconium hydride, water and graphite.

The documentation about the first criticality tests reported three sets of experimental measurements: 8 critical configurations were obtained by using the three control rods at the same time, 8 involved the SHIM and

Regulating control rods only and 11 involved the Transient and SHIM rods. The control rod positions are reported in Tab. 2.3 as they appear in the reactor equipment: each step corresponds to about 0.05 cm displacement from the bottom of the reactor core, while the distance spanned by the rods from the full inserted to the full withdrawn position is equal to 38.1 cm for SHIM and REG and 47.2 cm for TRANS. In 1965, the step digits ranged from 116 to 821 in the case of REG, from 130 to 835 in the case of SHIM and from 53 to 926 in the case of TRANS control rod.

The simulation results for all the configurations are reported in Tab. 2.3 and presented in Fig. 2.13, 2.14 and 2.15.

Most of the criticality values fall in the $\pm 2\sigma$ range from the expected value ($\rho = 0\$$), showing a good agreement between the simulated and the experimental data. The reported uncertainty values include only the statistical component, evaluated at 1σ. If one considers a systematic error $\sigma_{sys} \sim 0.25$ \$ (derived with detail in Sec. 2.3.4), an even better agreement with the experimental results is found.

It is worth noting that the configurations where the Transient rod is involved show a slightly worse behavior with respect to the others. This is most probably due to the fact that the documentation available about the Transient rod is poorer respect to the SHIM and Regulating rods and some approximations had to be applied for describing it.

This clearly underlines that the accuracy employed in reproducing the geometries, the materials and the positions of the control rods is fundamental for a correct evaluation of the system's k_{eff}. In fact, this parameter is very sensitive to small changes in the system and a poor description of the core components can lead to significant systematic errors.

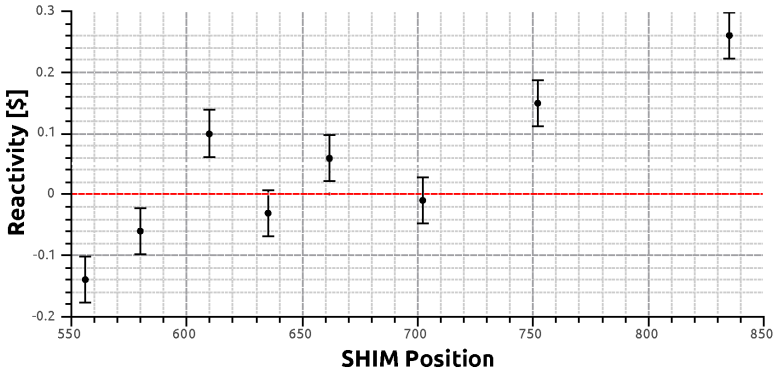

Fig. 2.13: Simulation results of the critical configurations obtained by inserting the three control rods simultaneously.

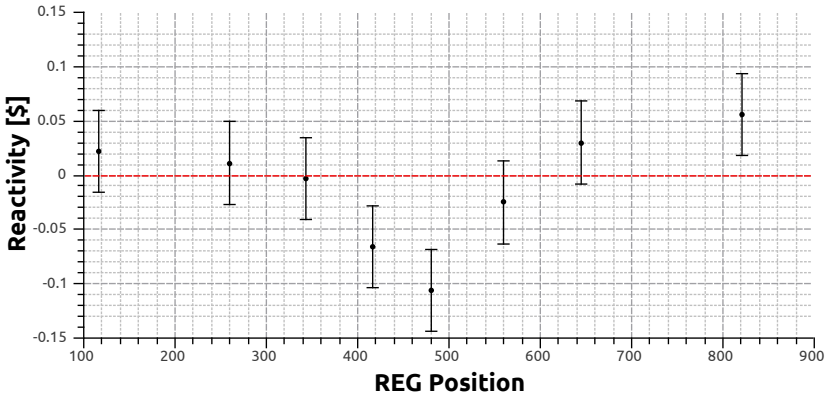

Fig. 2.14: Simulation results of the critical configurations obtained by inserting the REG and SHIM control rods.

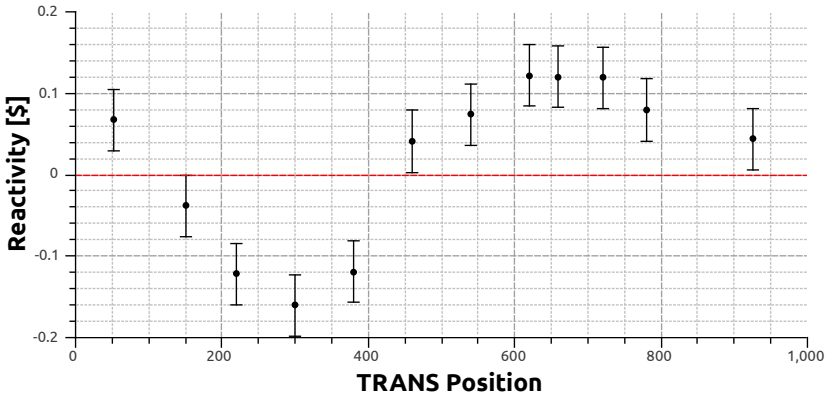

Fig. 2.15: Simulation results of the critical configurations obtained by inserting the TRANS and SHIM control rods.

2.3.3 Control rod calibration

The next step in the benchmark analysis was the check of the simulation model to reproduce the experimental control rod calibration curves, which represent the reactivity variations as a function of the rod positions inside the core.

The experimental procedure used to obtain the TRIGA calibration curves is the *reactor stable period method* (see Sec. 1.2.4), which can be used to calculate the reactivity insertion induced by a control rod step ($\Delta\rho$) via the *inhour* equation (Eq. 1.76).

At first, the reactor is brought to a critical state at low power level be-

Control Rod Positions (digit)			k_{eff}	ρ (\$)
TRANS	SHIM	REG	[± 0.00028_{stat}]	[± 0.04_{stat}]
433	556	503	0.99898	-0.14
433	580	440	0.99959	-0.06
53	610	821	1.00074	0.10
53	635	664	0.99975	-0.03
53	662	592	1.00043	0.06
53	702	527	0.99995	-0.01
53	752	469	1.00108	0.15
53	835	428	1.00193	0.26
out	386	821	1.00041	0.06
out	410	645	1.00022	0.03
out	436	559	0.99982	-0.02
out	462	480	0.99923	-0.11
out	485	417	0.99952	-0.07
out	511	344	0.99998	0.00
out	534	260	1.00008	0.01
out	556	116	1.00016	0.02
53	607	out	1.00049	0.07
150	583	out	0.99972	-0.04
220	562	out	0.99911	-0.12
300	535	out	0.99883	-0.16
380	503	out	0.99913	-0.12
460	476	out	1.00030	0.04
540	447	out	1.00054	0.07
620	425	out	1.00089	0.12
660	417	out	1.00088	0.12
720	403	out	1.00087	0.12
780	393	out	1.00058	0.08
926	386	out	1.00032	0.04

Tab. 2.3: Results of the k_{eff} and corresponding reactivity values obtained by simulating the criticality control rod positions.

tween 1 and 10 W, then one of the control rods is moved up by a small step. After the initial transitory phase, the reactor power increases over time following an exponential law with stable period T:

$$P = P_0 \, e^{\,t/T} \tag{2.8}$$

The time t taken by the system to increase its power output by 50% is then

measured to evaluate the period T:

$$T = \frac{t}{ln\left(\frac{P}{P_0}\right)} = \frac{t}{\ln(1.5)} \tag{2.9}$$

The measurement of t is repeated more than once after the reactivity insertion so as to control that the system has reached the stable period condition when the data are taken.

This procedure is repeated several times, until the entire length of the control rod is analyzed. The calibration curve is then obtained by adding up all the reactivity steps, which are usually calculated using the \$ units, so that the inhour equation becomes:

$$\Delta\rho[\$] = \frac{\Lambda}{\beta_{eff}T} + \sum_{i=1}^{6} \frac{f_i}{1+\lambda_i T} \tag{2.10}$$

where $f_i \equiv \beta_i/\beta_{eff}$ represents the fraction of each delayed group over the total delayed neutrons.

Unlike the β_{eff} parameter, the fractions f_i can be assumed independent of the reactor geometry and their values are well known for ^{235}U thermal fissions. Moreover, since the β_{eff} is declared to be 0.0073 for the TRIGA Mark II reactor [9] and the neutron invariant mean life (Λ) is of the order of the prompt neutron lifetime ($l_p \approx 10^{-4}$ seconds, see Sec. 1.2.4), the first term in Eq. 2.10 is found to be negligible for reactor periods longer than 1 second.

This condition is widely respected in the measurements for calibrating the control rods and, as a consequence, the evaluation of the reactivity step in dollars is not affected by the uncertainties associated with Λ and β_{eff}. The experimental error on the reactivity is then dominated by the uncertainty linked to the measurement of the period T.

The available documentation does not contain any reference to the experimental errors regarding these measurements; however, it is stated that each reported period value was obtained by averaging a set of 3 or 4 measurements. Relying on some measurements, which were recently performed with the same experimental procedure, the period uncertainty σ_T/T has been estimated to be around 5%.

This uncertainty can then be used to evaluate the one associated to $\Delta\rho$:

$$\sigma_{\Delta\rho} = \left|\frac{\partial\Delta\rho}{\partial T}\right| \sigma_T. \tag{2.11}$$

In this way, the experimental uncertainty related to every step in the control rod calibration procedure was finally estimated between 2.5% and 4.5%.

In order to reconstruct the control rod calibration curves with the MCNP model, for each reactivity step two simulations are performed with the control rods in the positions assumed before and after the step insertion respectively. The $\Delta\rho$ value is then evaluated from the difference of the resulting criticality coefficients (k_{eff}) and converted in \$ units by using the declared β_{eff} value (730 pcm).

The comparison between the experimental data and the Monte Carlo simulation results is reported in Fig. 2.16. The error value associated with the Monte Carlo results is given by the statistical component alone and it will be noted that the uncertainty increases at each subsequent calibration point in both the experimental and simulation curves. This is due to the fact that the calibration procedure implies that each reactivity step is summed to the previous ones.

In order to verify the goodness of the simulations, the experimental and Monte Carlo results were compared with a chi-squared test. The χ^2 variable, whose expected value is the number of *degrees of freedom* ν, is defined by:

$$\chi^2 = \sum_{i=1}^{N} \left(\frac{x_i - \mu_i}{\sigma_i} \right)^2 \tag{2.12}$$

where x_i is the Monte Carlo result, μ_i the experimental value and σ_i is given by the combination of the experimental and Monte Carlo uncertainties [6]. The sum is performed over the N calibration points [7], which in this case are also equal to the number of *degrees of freedom* ν. The values of χ^2 and ν related to the three calibration curves are reported in Tab. 2.4, together with the corresponding *p-value*, i.e. the probability of obtaining a χ^2 value at least as big as the one that was actually observed.

By taking a significance level $\alpha = 5\%$, it is observed that the Regulating calibration curve is more accurate than the others. This can be explained by considering that it is the only curve obtained without inserting the Transient rod, which could be modeled only approximatively.

In general, despite the presence of some systematic error associated with the Transient rod description, we can argue that the simulation results are in good agreement with the experimental data for all calibration curves, providing further evidence of the model reliability.

[6] The χ^2 was calculated using the experimental and the Monte Carlo data referring to the $\Delta\rho$ values, which are independent statistical variables.

[7] The first point is excluded because it is conventionally set to zero in both curves.

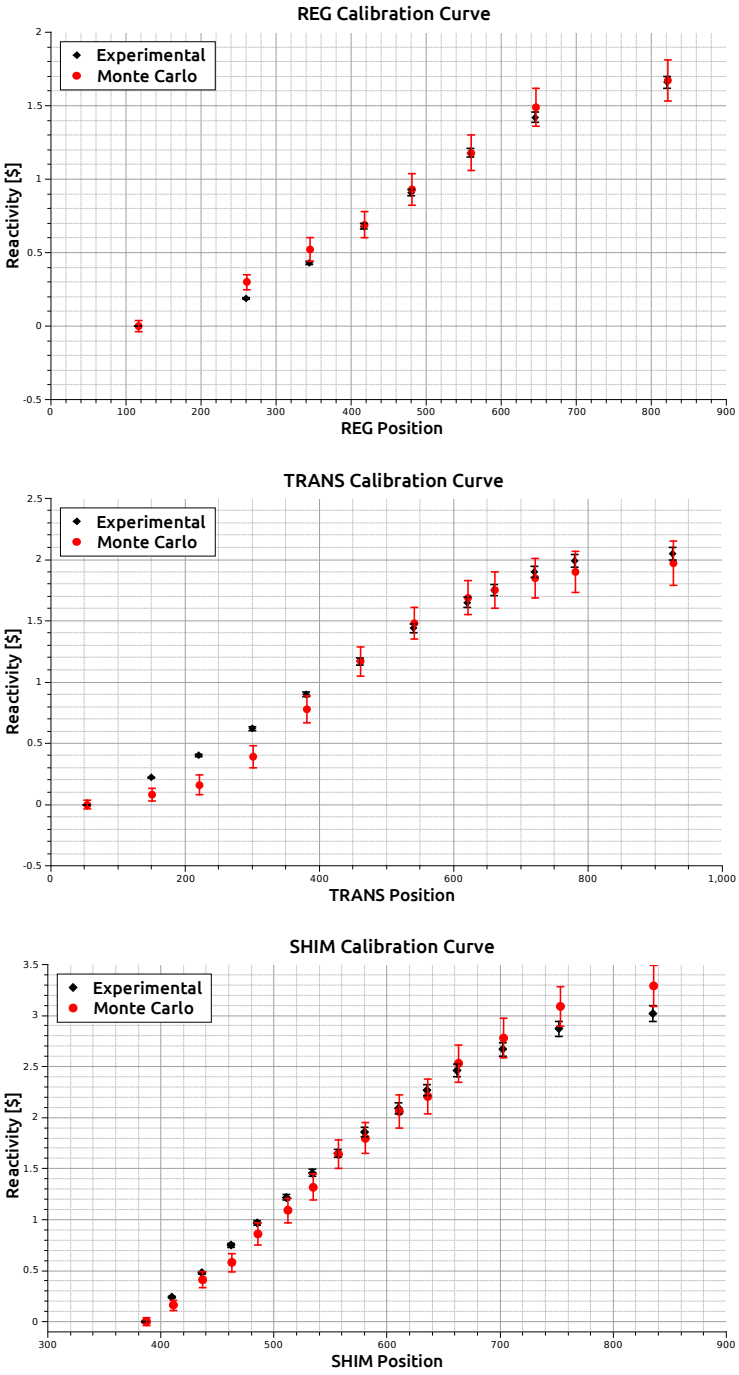

Fig. 2.16: Comparison between experimental and Monte Carlo calibration curves of the control rods.

	χ^2	ν	*p-value*
REG	8.85	7	26%
TRANS	19.93	11	4.6%
SHIM	24.37	14	4.1%

Tab. 2.4: χ^2, ν and p-values for the three calibration curves.

2.3.4 Systematic errors analysis

Finally, the systematic errors associated to some of the reactor parameters have been evaluated to better characterize the MCNP model. In particular, the effects of fuel enrichment and nuclear graphite density have been analyzed separately, in order to quantify each individual effect. Moreover, a different set of cross section libraries was tested to check the model dependence on this choice.

Fuel Enrichment The enrichment in ^{235}U of the TRIGA fuel elements is equal to $(19.75 \pm 0.05)\%$. If every fuel element had a different enrichment falling in this interval, the global effect on reactor criticality would be completely negligible, because the average enrichment would be very close to 19.75%. However, since the serial numbers of most of the fuel elements are sequential, it is reasonable to assume that most of them were manufactured from the same batch of ZrH-U fuel. In this situation, the enrichment percentage is the same for each fuel element and a variation within the range $\pm 0.05\%$ around the central declared value can lead to a significant systematic effect.

In order to quantify this component of systematic uncertainty, a set of 100 simulations was performed, in which the enrichment percentage was randomly picked from the documented interval and assigned to every fuel element in the reactor core.

The standard deviation of the resulting k_{eff} distribution includes both the statistical and the systematic error component. After subtracting the statistical uncertainty, which is directly obtained from the simulation results, the systematic error related to the fuel enrichment has been estimated equal to 0.22 \$.

Nuclear Graphite Density Another parameter which was considered is the density of the nuclear graphite. Since its nominal value is not reported on the official reactor documentation, a value equal to 1.70 g/cm^3

was employed, according to the data found in various reports on AGOT-grade nuclear graphite [19] [20] [21]. However, other bibliographic sources report different values, with the density ranging from 1.62 g/cm^3 [22] to 1.77 g/cm^3 [23].

Therefore, 100 simulations with the graphite density varying in the 1.62 − 1.77 g/cm^3 interval, were performed in order to evaluate the systematic error component with the same procedure as before. In this case, a systematic uncertainty equal to 0.14 \$ was obtained.

Since this uncertainty is not correlated with that of fuel enrichment, the total systematic error was finally calculated by combining the two errors in quadrature and resulted to be $\sigma_{sys} \sim 0.26$ \$.

Cross Section Libraries In order to test the model dependence on the choice of the cross section library, some simulations were run by using the ENDF/B-VII.1 instead of the JEFF-3.2 libraries. The cross sections of the core elements were changed one by one and the differences of the resulting k_{eff} were analyzed.

Looking at the results reported in the second column of Tab. 2.5, it will be noted that there are no significant differences when using either the ENDF/B-VII.1 or the JEFF-3.2 libraries, except for the case of zirconium. In this case, a relatively large reactivity variation equal to ∼0.6 \$ is observed. This anomalous behavior was also recorded in another work [24] and could be caused by an improper compilation of the new ENDF/B-VII zirconium libraries.

As a further investigation on this aspect, a new set of simulations was performed by changing the ENDF/B-VII cross sections with the previous release of the same libraries: the ENDF/B-VI. Looking at the third column of Tab. 2.5, it is interesting to note that the reactivity variation due to zirconium is completely balanced, confirming that a review of the ENDF/B-VII cross section data of zirconium is needed.

Finally, it is interesting to note that a reactivity variation of about 0.25 \$ is recorded for the case of uranium when changing the ENDF/B-VII with the ENDF/B-VI cross section. This finding is consistent with the fact that the simulation model is sensitive to relatively small variations in the uranium description, as found in the analysis of the fuel enrichment. As a consequence, since the uranium cross sections are known with a relative uncertainty of few percent in the thermal and resonance energy region [25], the reactivity can significantly vary when using different releases of the same cross section, especially when new experimental data are used for their evaluation.

Element	JEFF-3.2 → ENDF/B-VII	ENDF/B-VII → ENDF/B-VI
	$\Delta\rho$ (\$) $[\pm\ 0.05_{stat}]$	$\Delta\rho$ (\$) $[\pm\ 0.05_{stat}]$
H	-0.01	-0.03
O	0.01	-0.07
Al	-0.02	0.04
C	-0.01	0.05
Zr	**0.62**	**-0.64**
U	-0.02	**-0.25**
Sm	0.02	0.01
B	0.07	-0.03

Tab. 2.5: Reactivity variations while substituting the JEFF-3.2 with the ENDF/B-VII cross section libraries (second column) and the ENDF/B-VII with the ENDF/B-VI cross section release (third column).

2.4 Full power reactor characterization

After the good agreement of the results obtained in the benchmark analysis of the first reactor configuration with the fuel-moderator at room temperature, it is now possible to adapt the MCNP model for simulating the full power condition. The ultimate goal of the thermal effects analysis is to reconstruct a mapping of the fuel and moderator temperature distribution to be introduced in the MCNP model through the use of the cross section thermal treatments. In this way, it will be possible to check if the simulation model is able to predict the expected k_{eff} value for the criticality configurations which were recorded in 1965, when the reactor was brought to the full power steady-state condition for the first time.

The main challenge in this kind of analysis is the reconstruction of the temperature distribution within the core. In fact, only two fuel elements in the reactor were equipped with thermocouples for the measurement of the fuel temperature and the available data are not sufficient to characterize the temperature profiles in the axial and radial directions of the core. Moreover, there are no available data concerning the temperature of water between the fuel elements.

The strategy pursued to overcome this lack of information was:

- measuring the temperature of water between the fuel elements;
- evaluating the distribution of the power release in the fuel elements through the MCNP simulations;
- exploiting a thermal-hydraulic simulation model of the TRIGA reactor to reconstruct the in-core thermal map from the power release data and the experimental measurements of water and fuel temperatures.

This approach involves some approximations, like the use of the present water temperatures and the evaluation of the power distribution with the MCNP simulation model at room temperature.

However, we can reasonably assume that the water temperature has not significantly changed over time, because the power is kept constant at 250 kW and the core dimensions are about the same except for the outer ring, which has been progressively filled with more fuel elements.

Regarding the approximation in the evaluation of the power distribution, in principle it would be possible to recursively repeat the analysis updating each time the temperature profile in the MCNP model. Anyway, the expected correction with respect to simulating a constant room temperature value in the core is negligible, because the evaluation of the power release depends on the fission rate distribution, which is not significantly affected by temperature variations [26].

2.4.1 Temperature measurements within the core

In order to measure the temperature of water within the core, we designed and built an experimental kit consisting of a set of aluminum rods, the last one being equipped with Pt1000 *Resistance Temperature Detectors* (RTDs). These sensors are platinum resistors, whose resistance changes linearly with temperature and is equal to about 1000 Ω at 0°C. The Pt1000 RTDs were chosen for the fast time response and the sensitivity for temperature evaluation: in fact, a resistance variation of 1 Ω corresponds to about 0.25°C. Moreover, the small RDTs size −of the order of few mm− allows their insertion through the holes (8 mm in diameter) drilled in the top grid of the core (Fig 2.17).

A total of 7 Pt1000 RTDs were mounted on a rod 6 mm in diameter and 88 cm long, made of nuclear aluminum, a material characterized by high purity which facilitates compliance with the radiation protection requirements. For the same reason, the amount of copper used to connect the RTDs was minimized using thin wires 50 μm in diameter. All the electrical

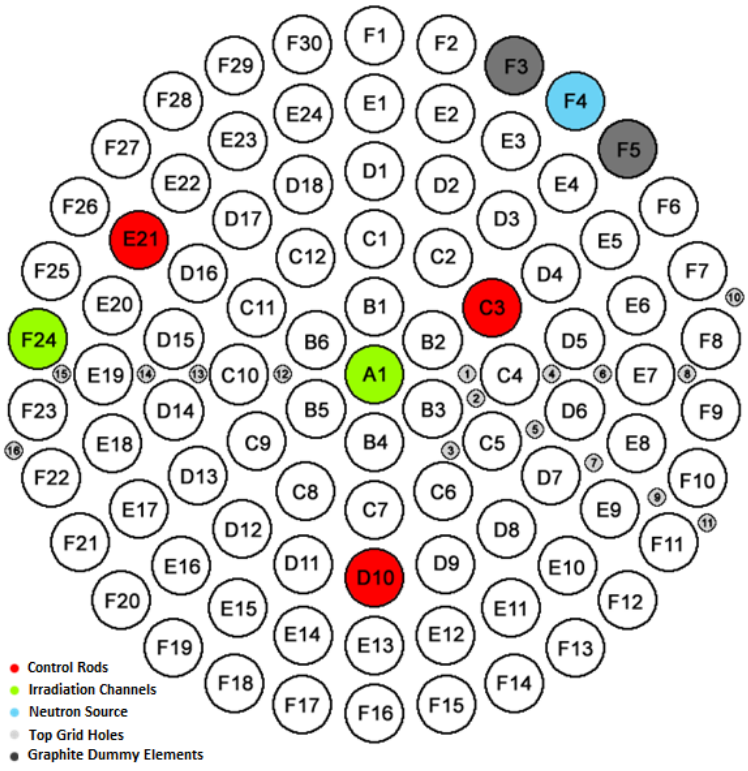

Fig. 2.17: The core scheme with the positions of the top grid holes.

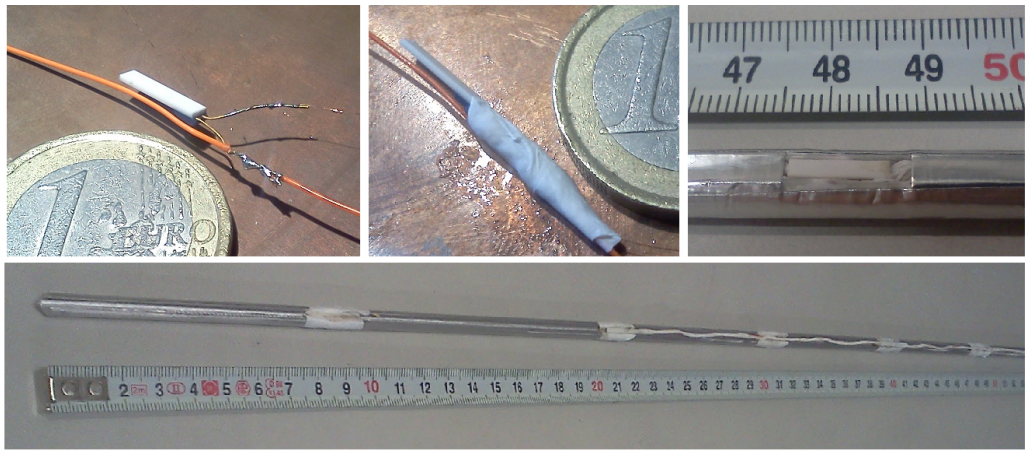

Fig. 2.18: Top (from left to right): a Pt1000 RTD (viewed before and after the electrical insulation) and its final installation on the supporting rod. Bottom: the aluminum rod with the Pt1000 RTDs installed on it.

connections were insulated using a teflon tape and the 7 Pt1000 RTDs were finally positioned in two opposite grooves along the rod, so as to measure the temperature at different core heights (Fig. 2.18).

Before the in-core measurements, the RTDs were calibrated by immersing the rod in a container filled with water which was progressively heated from 17.2°C to 72.6°C. The temperature was measured with a reference digital thermometer (0.1°C sensibility) which was previously inter-calibrated with two mercury thermometers, finding a systematic error of about 0.2°C. At the same time, the resistance values of the Pt1000 were measured with a digital multimeter (1Ω precision).

RTD	m (°C/Ω)	q (°C)
1	0.2571±0.0003	-260.5±0.3
2	0.2568±0.0004	-259.8±0.4
3	0.2569±0.0004	-260.0±0.4
4	0.2576±0.0005	-260.2±0.6
5	0.2580±0.0004	-260.8±0.4
6	0.2583±0.0003	-260.8±0.3
7	0.2575±0.0008	-259.8±0.6

Tab. 2.6: Coefficients of the RTDs' calibration lines.

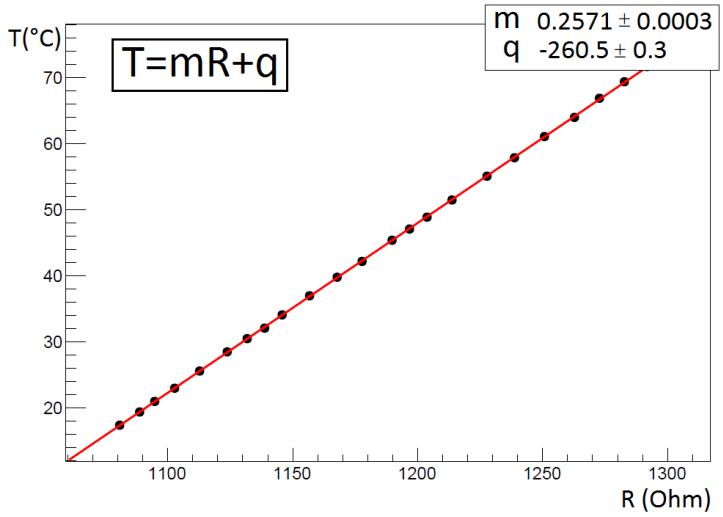

Fig. 2.19: Calibration line of the RTD number 1, obtained by fitting the experimental data with a first degree polynomial.

The experimental points were then fitted with a straight line (Fig.2.19) to find the calibration coefficients (Tab 2.6). With such procedure, the temperature can be evaluated with about 1°C accuracy, which is enough for our purposes.

Finally, the experimental apparatus was installed on the top of the reactor (Fig. 2.20), inserting the rod in the hole number 13, which is located between ring C and D. The wires welded to the Pt1000 RTDs were connected to a dedicated module for the digital acquisition of all sensors resistance data with a sampling step which was fixed to be 1 second.

In order to extract the maximum information on the TRIGA reactor thermal-hydraulics, two kind of measurements were planned:

1. with the cooling system ON: this is the normal configuration at steady-state operation (250kW), which we aim to model in the full power MCNP simulations. Although the inlet water temperature is kept constant, the TRIGA cooling system is somehow peculiar, because the water is injected above the core, making it impossible to fix a boundary condition to the inlet temperature below the core (Fig. 2.21);

2. with the cooling system OFF: this condition allows to study the natural circulation regime for analyzing the system's dynamics in the absence of external perturbations.

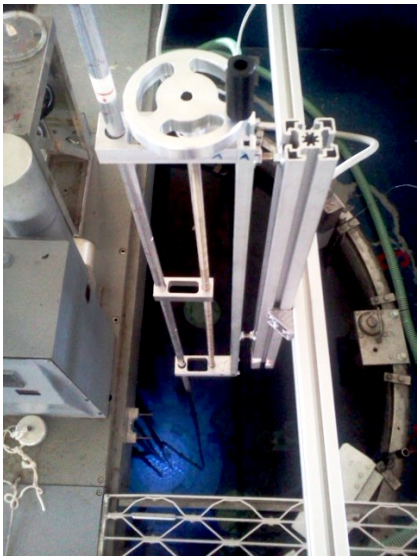

Fig. 2.20: The temperature sensor rod installed in the core as viewed from the reactor top during a measurement.

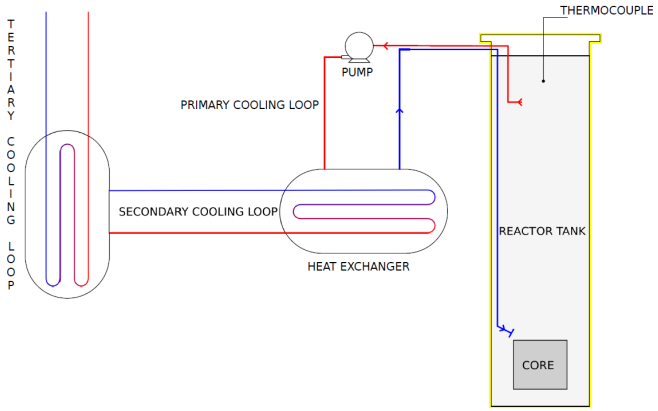

Fig. 2.21: Scheme of the TRIGA Mark II reactor cooling system.

At the beginning, the measurements were planned to be performed in different core positions, to reconstruct the temperature field within the core. However, after three measurements in the hole number 13 with the rod positioned at different heights, the wires insulation was damaged by neutron irradiation and the resistance values were no more measurable.

Anyway, the results of the three measurement campaigns are very interesting and provided enough information to improve the TRIGA reactor thermal-hydraulic modeling.

In the first measurement, the cooling system was held ON and the rod was positioned so that the RTD 7 was above the top grid. Looking at the experimental data reported in Fig. 2.22, one can see that the in-core water temperature increases almost instantly during the rising phase at full power. When the reactor operates at 250 kW, the average in-core temperature is between 45°C and 55°C, while it is around 30°C in the region above the core. It is worth noting that in this condition, with the cooling ON, the data profiles are very noisy, especially those corresponding to the RTDs closest to the top grid: for example, the RTD 6, which is just below the grid, exhibits sudden and large drops in temperature. This behavior can be attributed to the action of the cooling system, which injects cold water from the top of the core.

The second measurement was performed while keeping the cooling system OFF during the first 15 minutes. The rod was moved 12 cm down so that the RTD 1 was below the fuel active region (Fig. 2.23). In the first part of the measurement, the RTD 1 temperature is constant and equal to the value recorded before the reactor startup, while the other RTDs temperatures were quite stable around different values depending on the sensor position. This configuration is perturbed when the cooling system is switched on: in particular, the RTD 1 starts to record increasing temperatures, while the

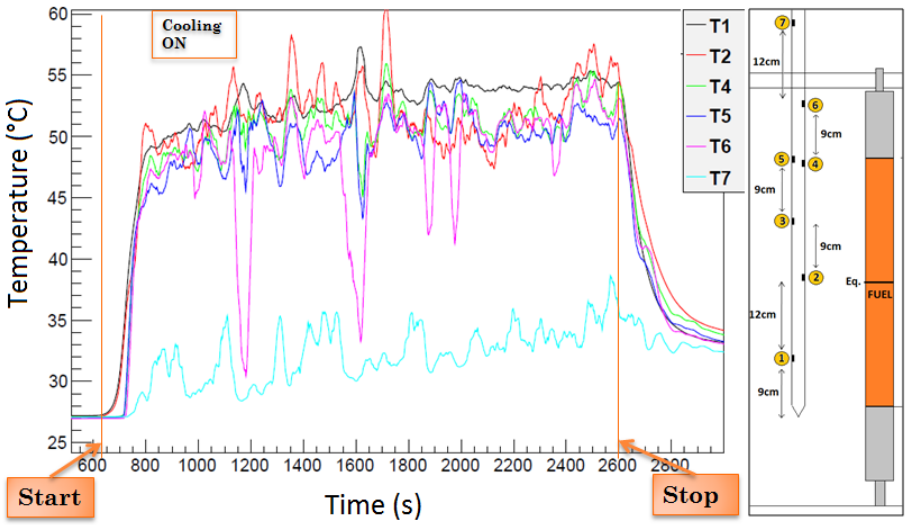

Fig. 2.22: Temperature data recorded in the first measurement (left) and scheme of the positions occupied by the Pt1000 sensors (right). The start and stop labels indicate the instants in which the reactor is switched ON *and* OFF*, respectively.*

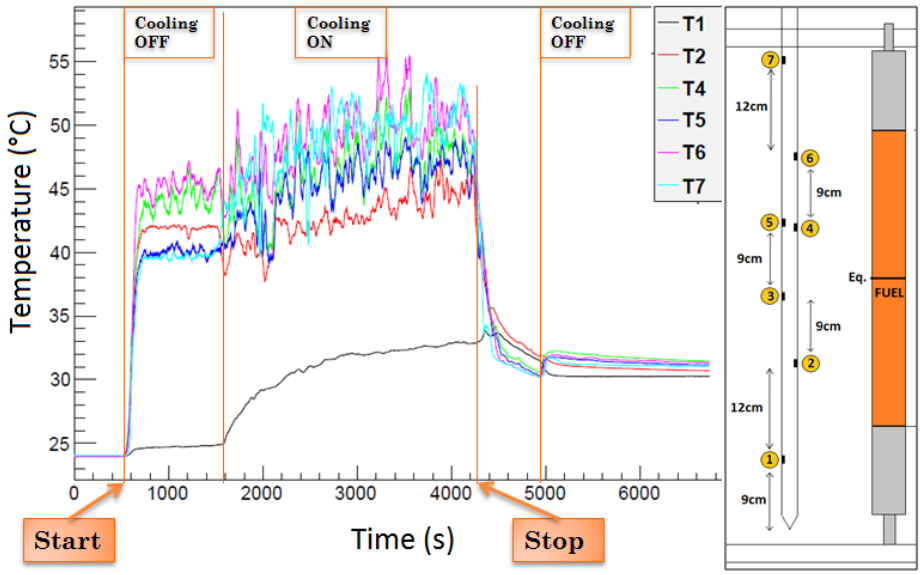

Fig. 2.23: Temperature data recorded in the second measurement (left) and scheme of the positions occupied by the Pt1000 sensors (right).

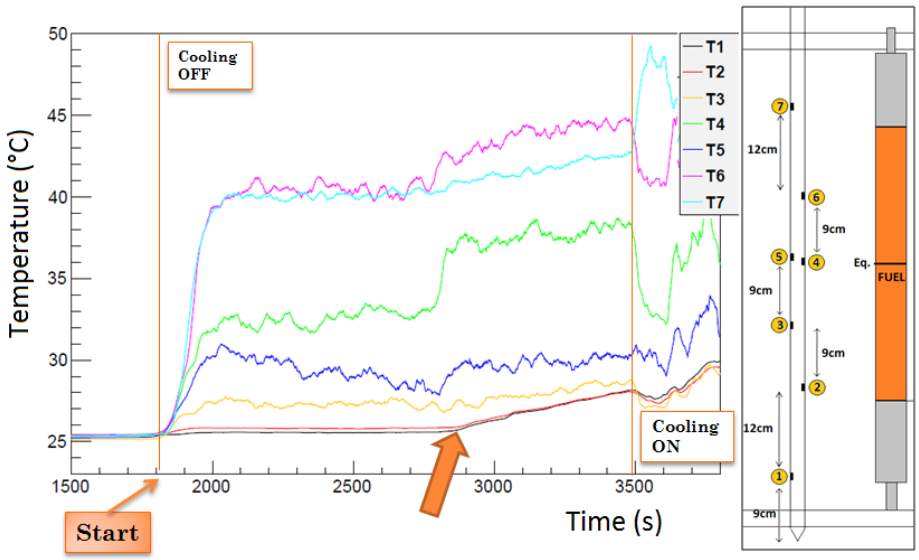

Fig. 2.24: Temperature data recorded in the third measurement (left) and scheme of the positions occupied by the Pt1000 sensors (right). The arrow indicates the instant in which the sensors below the fuel active region start to record higher temperature values.

others reproduce the situation of the first measurement.

Finally, in the third measurement, the cooling system was held OFF for a longer time (25 minutes) and the rod was moved further down by 6 cm. In this case it is interesting to note that about 1000 seconds after reaching the full power condition, the sensors below the fuel active region (RTDs 1 and 2) start to record higher temperature values. At the same time, the RTDs 4 and 6 exhibit a sharp increase in the temperature, while the data recorded by RTDs 3 and 5 are unreliable, because their connections were probably already damaged, as it was verified in the subsequent measurement tests. Anyway, the data collected with the properly working sensors show that after 1000 seconds the whole pool is heated and the hot water reaches the region under the core, modifying the inlet temperature boundary condition.

Although new measurements are required for a complete characterization of the in-core water temperature distribution, these data allowed to evaluate the average water temperature during the full power reactor operation. Moreover, the observed phenomena related to turbulent motions and pool global warming are being studied by our colleagues at Polytechnic University of Milan, which are working on the development of thermal-hydraulic models for the TRIGA Mark II reactor [27].

2.4.2 Fuel temperature distribution evaluation

In order to reconstruct the distribution of the fuel temperatures, the simulation package COMSOL Multiphysics 4.3a [28] (Finite Elements) have been used by our colleagues at Polytechnic University to develop a thermal-hydraulic model for the TRIGA Mark II reactor. The experimental data collected in the measurement campaigns and the temperature values recorded by the thermocouples in the instrumented fuel elements were used as a benchmark for this simulation model.

The reactor core was modeled as a cylinder limited to the active fuel region ($\sim$36 cm in height), containing water and fuel elements. The FE claddings were modeled as equivalent thermal resistances and appropriate boundary conditions were fixed for the water temperatures and velocities. Moreover, in order to take into account the 5 m of water above the core, the pressure was fixed at 1.5 bar and the water boiling temperature at 111°C.

The system's thermal-hydraulics was modeled using the *Computational Fluid Dynamics* (CFD), which is a branch of fluid mechanics that uses numerical methods and algorithms to solve and analyze problems that involve fluid flows. This approach is based on the Navier-Stokes equations and allows to model the convective and conductive heat transfers within the core.

In this way, by providing the power distribution in the fuel elements, it

is possible to obtain a 3D mapping of their temperatures.

The MCNP simulation model of the 1965 reactor configuration was exploited to evaluate the power release in the fuel elements. Each FE was subdivided into 8 sections to take into account the neutron flux inhomogeneity along the vertical axis and tally F4 were used to estimate the average fission interaction rate (R_f) in each fuel volume, according to the formula:

$$R_f = N_{235} \int \varphi(E)\, \sigma_f(E)\, dE \tag{2.13}$$

where N_{235} is the number of ^{235}U atoms per fuel section. The MCNP neutron flux was normalized to the total number of neutrons which are produced per unit time in the reactor when it operates at 250 kW[8]. The power release was thus estimated by multiplying R_f by the effective energy released per ^{235}U fission (192.9 MeV). The results are presented in Tab. 2.7, where for brevity the average power values of the FE belonging to the same ring are reported.

Fuel	Released Power (W)				
Section	Ring B	Ring C	Ring D	Ring E	Ring F
1	561	485	427	362	298
2	703	608	526	432	338
3	826	712	614	496	376
4	879	760	657	528	404
5	830	720	626	515	394
6	722	632	548	463	347
7	589	514	443	386	280
8	443	391	341	308	229
Total	5553	4824	4183	3491	2666

Tab. 2.7: Average power release in the 8 sections of the fuel elements (1→8 from top to bottom) as a function of the core ring in which are located. The Monte Carlo statistical error component was reduced so it can be considered negligible.

[8] The normalization factor ($\mathcal{N}$) for the neutron flux is obtained as follows:

$$\mathcal{N} = 3.24 \times 10^{10}\, \frac{\text{fissions}}{\text{J}}\; 250\,\text{kW}\; 2.43\, \frac{\text{neutrons}}{\text{fission}} = 1.96 \times 10^{16}\, \frac{\text{neutrons}}{\text{s}}$$

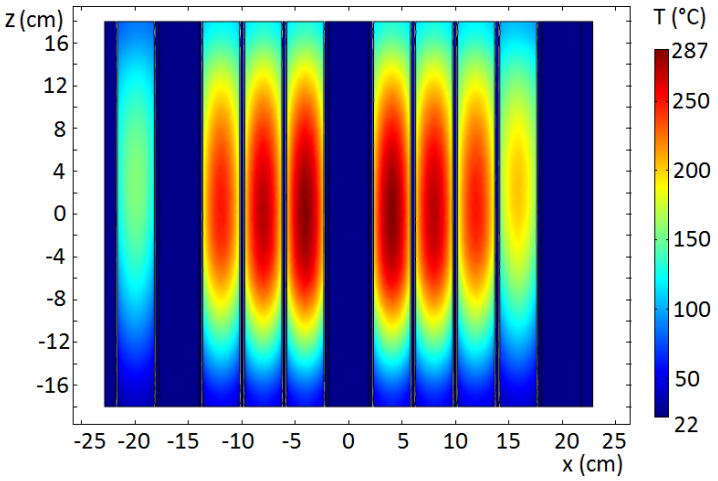

Fig. 2.25: Vertical section of fuel temperature distribution in the diagonal plane intersecting the REG control rod.

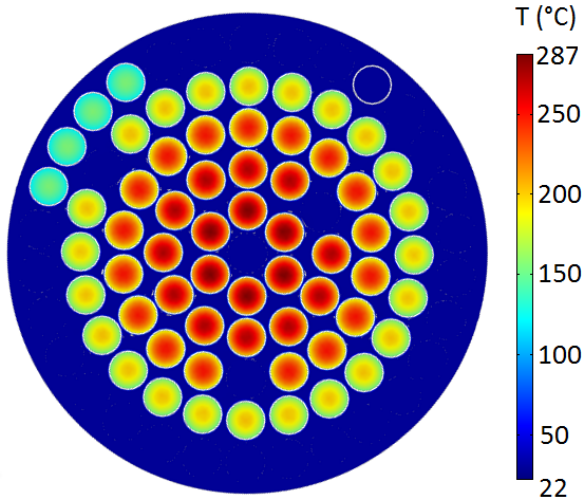

Fig. 2.26: Horizontal section of fuel temperature distribution in the equatorial core plane.

Finally, through the COMSOL thermal-hydraulic simulation, the complete fuel temperature 3D map was evaluated for the TRIGA Mark II reactor core. Looking at the vertical and horizontal sections presented in Fig. 2.25 and 2.26 respectively, it is interesting to note that the thermal distributions are characterized by large temperature variations, passing from about 280°C in the center of the inner FEs to about 50°C in the peripheral core regions.

2.4.3 Full power simulation model

In order to model this thermal distribution in the full power MCNP simulations, the fuel elements were subdivided into 5 sections (1→5 from top to bottom), to which cross sections at different temperatures were assigned, depending on the occupied position along the vertical and radial core axes (Tab. 2.8).

For this purpose, new cross sections values were generated for ZrH and uranium every 10°C, because the original libraries provided cross sections with a too coarse discretization step (100°C) for describing the in-core thermal distribution.

In this way, it has been possible to approximate the average temperature in each fuel section to the closest one available in the new cross section list, allowing an accurate modeling of the thermal effects which influence the low-energy scattering on ZrH and the interactions with uranium. In addition, the water between the fuel elements was simulated at an averaged temperature of 330 K, according to the experimental data collected in the measurement campaigns.

The new full power MCNP model was finally benchmarked using the data available in the First Criticality Final Report [18] concerning four different control rods critical configurations at 250 kW power.

Experimentally, the decrease of reactivity due to the thermal effects is compensated by withdrawing the control rods: using the calibration curves and comparing the criticality positions at full power with those at low power, the experimental reactivity loss has been estimated to be (1.36±0.06)$.

Similarly, in the MCNP simulations, we can check that the effect of introducing the thermal distribution in the model is properly counterbalanced

Fuel	Core Ring				
Section	B	C	D	E	F
1	430	420	410	390	380
2	490	480	460	430	400
3	500	500	480	430	400
4	480	460	440	400	370
5	370	360	350	360	330

Tab. 2.8: Temperature values (in K degrees) employed to model the thermal distribution in the full power MCNP simulations.

by moving the control rods in the full power positions, reaching again the $\rho = 0\,\$$ criticality condition.

The simulation results presented in Fig. 2.27 show that the reactivity variation due to the thermal effects is properly quantified in the full power MCNP simulations. In fact, taking into account that the average value of the results is 0.16 \$ with a standard deviation of 0.16 \$, the obtained reactivity values are in good agreement with the 0 \$ criticality condition.

Looking at the data in more detail, it will be noted that the third result is significantly different compared to the others. In this respect, it is worth saying that the corresponding 250 kW criticality configuration is the first one reported in the historical documentation, while the other configurations refer to an experimental test performed 12 days later. Therefore it is reasonable to assume that a systematic uncertainty due to ^{135}Xe poisoning could affect these results, providing a possible explanation for the differences observed in the data.

In conclusion, considering the experimental uncertainties affecting the historical data and the possible systematic errors, it can be stated that the (1.36±0.06)\$ reactivity variation due to thermal effects is correctly simulated in the MCNP model which was developed for the full power TRIGA reactor.

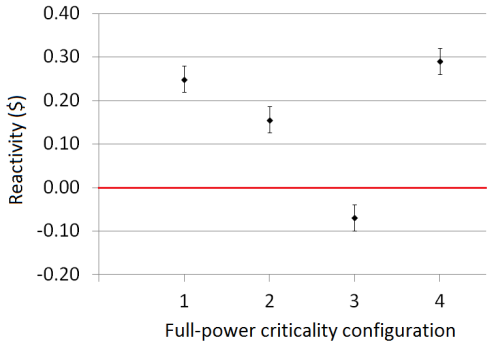

Cfg.	Position (digit)		ρ (\$)
#	SHIM	REG	[± 0.03_{stat}]
1	524	818	0.25
2	556	605	0.16
3	588	557	-0.07
4	673	350	0.29

Fig. 2.27: Results of the full power reactor simulations with the control rods in the experimental criticality configurations measured in 1965.

Chapter 3

Neutron flux measurement and analysis

The neutron flux is a crucial parameter for the analysis of nuclear reactors, because it affects the reaction rate and thus the fuel burnup. Moreover, an accurate and precise knowledge of the flux within the core is very helpful for benchmarking the simulation models of the reactor, especially the MCNP model described in the previous chapter. For this reason, some measurement campaigns have been performed at the TRIGA Mark II reactor, with the aim of evaluating the integral neutron flux and its energy spectrum in the main irradiation facilities and mapping its spatial distribution within the core.

The neutron activation technique, which involves the irradiation of samples containing a known amount of elements and the subsequent γ-ray spectroscopy analysis with HPGe detectors, has been chosen to perform this kind of measurements. In order to evaluate the activation rate with good accuracy, Monte Carlo models based on the GEANT4 simulation toolkit [29] are implemented to estimate the γ-ray detection efficiency for every radioisotope of interest.

The neutron flux is subsequently calculated from the activation rate data by using *effective cross sections*, which correspond to the average values of the activation cross sections over the neutron energy distribution. For this purpose, the MCNP reactor model is exploited for its capability of simulating the neutron flux spectra in the irradiation positions and a specific benchmark analysis is performed to check the reliability of the simulations in evaluating the neutron energy distributions.

In the first section of this chapter, I present the data analysis for the evaluation of the integral neutron flux in four irradiation positions using different activated isotopes. Particular care will be devoted to the analysis

of the possible systematic errors, in order to assess the reliability and the repeatability of this measurement technique.

In Sec. 3.2, the experimental data of the many different activated isotopes are combined through a Bayesian statistical approach to characterize the neutron flux spectra of the four irradiation facilities, providing a benchmark for the MCNP simulations used to evaluate the neutron energy distributions.

Finally, the measurement of the integral and fast neutron flux spatial distribution within the core are presented and discussed in Sec. 3.3.

3.1 Integral neutron flux measurement

The physical quantity to be measured in an activation experiment for the evaluation of the neutron flux is the *activation rate* R, i.e. the number of radioisotopes that are created each second by neutron-induced reactions. In fact, the activation rate is related to the neutron flux through the following equation:

$$R = \mathcal{N} \int \varphi(E)\, \sigma(E)\, dE \tag{3.1}$$

where $\mathcal{N}$ is the number of precursor isotopes in the irradiated sample and $\sigma(E)$ is the activation cross section. The effective cross section (σ_{eff}), i.e. the mean value of the cross section weighted by the neutron energy distribution, can be introduced to calculate the integral flux: $\Phi_{\text{tot}} \equiv \int \varphi(E)\, dE$.

$$\sigma_{\mathit{eff}} = \frac{\int \varphi(E)\, \sigma(E)\, dE}{\int \varphi(E)\, dE} \qquad \Rightarrow \qquad \Phi_{\text{tot}} = \frac{R}{\mathcal{N}\sigma_{\mathit{eff}}} \tag{3.2}$$

The effective cross section depends on the neutron spectrum distribution, which can vary in the different core positions and irradiation facilities.

For this purpose, we decided to exploit the MCNP model of the TRIGA reactor, that can be considered a reliable tool for simulating the neutron flux spectrum. The effective cross sections of the different activated isotopes were numerically calculated combining the neutron spectrum evaluation by MCNP simulations with the $\sigma(E)$ data published in the ENDF/B-VII and JEFF-3.1 cross section repositories. Some tests were performed to check that the number of bins (135) used for the integral calculation is large enough to obtain σ_{eff} values that are not significantly affected by the binning choice. Moreover, the σ_{eff} results obtained using the ENDF/B-VII or the JEFF-3.1 cross section data were compared, finding only negligible differences.

With neutron activation, radioisotopes are mostly produced by neutron capture and they usually β^- decay with simultaneous emission of γ-rays, even if different types of reactions and decays are possible.

The activation rate is then evaluated measuring the γ-rays emitted by the isotopes to assess their activity. If the isotope after the first decay is stable, the differential equation that describes the time evolution of the radioisotope production during the irradiation is:

$$dN = Rdt - N\lambda dt \tag{3.3}$$

where λ is the decay constant and N the number of radioisotopes in the sample. After the irradiation, the activity of the sample is described by the

following law:

$$A(t) = R\left(1 - e^{-\lambda t_{irr}}\right) e^{-\lambda t} \tag{3.4}$$

where t_{irr} is the irradiation time. Finally, if the measurement of a sample starts after a time t_{wait} and lasts a time t_{meas}, the number of decays that occur is expected to be on average:

$$n_{dec} = \frac{R}{\lambda}\left(1 - e^{-\lambda t_{irr}}\right) e^{-\lambda t_{wait}} \left(1 - e^{-\lambda t_{meas}}\right) \tag{3.5}$$

Gamma-ray spectroscopy with High Purity Germanium (HPGe) detectors allows to evaluate n_{dec} once the detection efficiency is known for the γ-rays emitted by each radioisotope. In order to evaluate the efficiency for each experimental configuration, we decided to exploit a Monte Carlo tool, based on the GEANT4 code, for its accuracy and flexibility in simulating the particle transportation and detection.

The Monte Carlo output provides a simulated γ-ray detector spectrum for a fixed number of decay events (n_{sim}) in the simulated source. In this way, the efficiency can be evaluated for each γ-ray of interest as the ratio between the photopeak counts in the simulated spectra (C_{sim}) and n_{sim}. Then, the number of decays (n_{dec}) can be calculated for each γ line observed in the experimental spectra through the following relation:

$$n_{dec} = \frac{C_{meas}}{C_{sim}} n_{sim} \tag{3.6}$$

where C_{meas} are the photopeak counts in the recorded spectra.

3.1.1 Samples irradiations and measurements

The irradiation campaigns were performed between November 2011 and July 2012[1] to measure the neutron flux in four irradiation facilities characterized by different neutron flux spectra and intensities: Central Thimble, Rabbit Channel, Lazy Susan, and Thermal Channel (see Sec. 2.1.3).

Samples containing many different elements to be activated were prepared with a dual purpose:

- testing the methodology of analysis with isotopes characterized by different activation cross sections;
- collecting the activation rate data from different isotopes for a subsequent analysis of the neutron flux spectra.

Standard Name	Elements	Concentration ($\mu g/mL$)
STD 2	Sc, La, Sm, Eu, Tb, Ho, Lu, Th	10.0 ± 1%
STD 3	Cr, Co, Ga, As, Se, Ag, Cd, In, Cs, U	10.0 ± 1%
STD 4	Ru, Sb, Hf, Ir, Au	10.0 ± 1%

Tab. 3.1: List of the elements in the standard solutions and mass concentration of each element.

	Central Thimble	Rabbit Channel
Sample	Mass (mg)	Mass (mg)
STD 2	9.25	10.38
	51.69	51.01
STD 3	9.79	9.71
	51.41	50.76
STD 4	10.29	10.34
	50.90	47.98
Ge	77.46	68.39
	57.32	78.42
Fe	25.38	26.31
Ni	38.42	44.29
In	21.25	39.80

	Lazy Susan	Thermal Channel
Sample	Mass (mg)	Mass (mg)
STD 2	100.8	102.4
STD 3	102.3	100.9
STD 4	101.7	101.0
Ge	98.80	114.1
Fe	24.60	26.60
Ni	38.80	53.00
In	43.10	48.30
Al-Co	-	22.50

Tab. 3.2: Masses of the irradiated samples; the experimental error is the balance sensitivity, i.e. the last decimal place.

With the aim of identifying the possible systematic errors affecting the measurements, the following precautions have been adopted:

- the geometry and the matrix of samples were diversified using both liquid solutions and solid foils;
- samples containing different masses of the same solutions were prepared to control the errors related to the weighting operations;
- the γ-ray spectroscopy measurements were repeated using three HPGe detectors with different characteristics to verify the correct evaluation of the detection efficiency parameter.

The liquid samples were prepared using three different Multi-element Calibration Standard solutions by PerkinElmer, containing many elements with concentrations certified within 1% accuracy (Tab. 3.1). The solutions were put in polyethylene vials filled with blotting paper to confine the liquid at the bottom and their masses were measured using an analytical balance. Thin solid foils of different materials were also prepared and the list of all samples with the corresponding masses is presented in Tab. 3.2.

The irradiations of samples lasted different times depending on the intensity of the flux in the facility (Tab. 3.3). The reactor power level was 250 kW in all cases except for the irradiation of the indium foil in the Central Thimble: in this case the power was decreased by a factor 100 to avoid excessive activation of the sample.

The HPGe detectors used for the γ-ray spectroscopy measurements are:

- a coaxial Germanium with a Beryllium window ($GePV$);
- a coaxial Germanium with an Aluminum end-cap ($GeGem$);
- a well-type detector with a thin Aluminum end-cap ($GePoz$).

The $GePV$ detector is installed in a shielded laboratory next to the TRIGA reactor and was used for the short measurements of the irradiated samples just after the extraction from the TRIGA reactor. The $GeGem$ and $GePoz$ detectors are located in the underground Radioactivity Laboratory of Milano-Bicocca University and were used for the medium and long term measurements in a low background environment [30]. In particular, $GePoz$ is

[1] At that time, the reactor core was loaded with 83 fuel elements: in particular, the outer rings E and F contained 49 FE(s) with aluminum cladding, while the inner rings hosted 34 FE(s) with stainless steel cladding.

Facility	Date	t_{irr}	Power [kW]	Samples
Central Thimble	21 Nov 2011	2h	250	STD, Fe, Ni, Ge
	22 Nov 2011	2h	2.5	In
Rabbit Channel	21 Nov 2011	2h	250	STD, Fe, Ni, Ge
	10 Apr 2012	2h	250	In
Lazy Susan	11 Apr 2012	6h	250	STD, Fe, Ni, Ge, In
Thermal Channel	31 Jul 2012	3h	250	STD, Fe, Co, Ni, Ge, In

Tab. 3.3: List of the irradiations performed in the different facilities of the reactor. STD refers to all the multi-element standard solutions used: STD2, STD3, and STD4.

characterized by a high detection efficiency thanks to the well configuration where the irradiated samples are located.

Depending on the sample activity, the measurements were performed at different source-detector distances, interposing up to five hollow boxes (each 1.9 cm high), in order to have a very low dead time and limit the pile-up counts. The measurements were repeated with different delays after the irradiation, in order to be sensitive to the elements with lower activity and longer decay time.

3.1.2 Activation rate evaluation

The first step in the data analysis is the evaluation of the activation rate for all the identified isotopes in the many collected spectra[2,3].

In order to validate the GEANT4 simulation tool implemented for evaluating the detection efficiency, preliminary tests were performed for every detector in the different measurement configurations. The experimental efficiency was evaluated through specific measurements performed with certified calibrated radioactive multi-γ sources and Monte Carlo simulations were run

[2] With respect to Eq.3.3 different formulas were used to describe the activation of ^{76}Ge, because ^{77}Ge decays with half-live 11.3 h on ^{77}As, that is not stable. In this case, the activities of ^{77}Ge and ^{77}As were measured and both data were used to calculate the activation rate of ^{76}Ge, finding in general a good agreement.

[3] When analyzing metastable isotopes, the probability of metastable state population after neutron capture must be introduced in the calculation of R. This probability was evaluated from the data on the website http://www-nts-iaea.org/ngatlas and resulted 62.5% for ^{77m}Ge, 35.9% for ^{152m}Eu, 5.17% for ^{110m}Ag, and 56.2% for ^{114m}In.

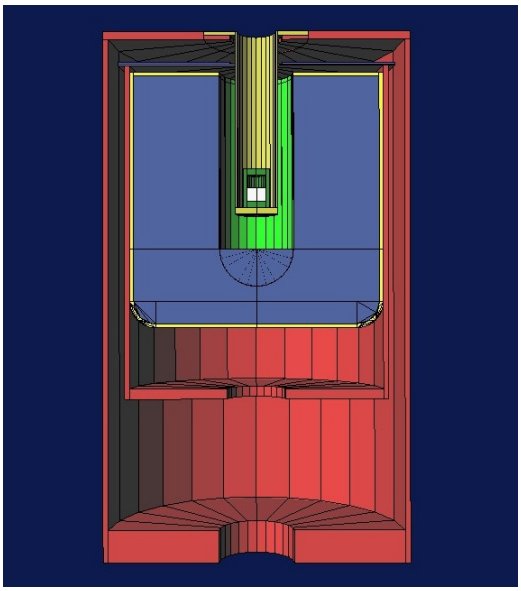

Fig. 3.1: The geometric reconstruction of GePoz detector in GEANT4 *simulations.*

to evaluate the simulated efficiency in the corresponding configuration. The two efficiencies, evaluated independently, were then compared and the detector simulation models were refined until an agreement of the order of 5% was reached.

After that, the source-detector configurations used for measuring the irradiated samples were modeled paying attention to the details which are important to achieve an accuracy in the order of the experimental one, that is related to the repeatability of the measurements (Fig. 3.1). Some simulation and experimental tests show that variations of few mm in the positions or dimensions of the samples significantly affects the efficiency parameter, because a different solid angle is subtended between the γ-ray source and the detector. For this reason, all the samples were prepared in view that a simple simulation of their shape was possible and that the systematic errors related to the source position were minimized. In particular, for liquid solutions, the blotting paper was used to confine the source in the lower part of the vial. Moreover, the distance between the source and the detector was measured with good accuracy and reproduced in the simulations.

The GEANT4 toolkit includes all the isotope decay schemes, so that the relative intensities of the many γ-rays emitted and the coincidence summing effect due to the γ cascades can be correctly simulated. This feature was fundamental to analyze the measurements performed with the samples close to the detector window or inside the well of the *GePoz*, since in those config-

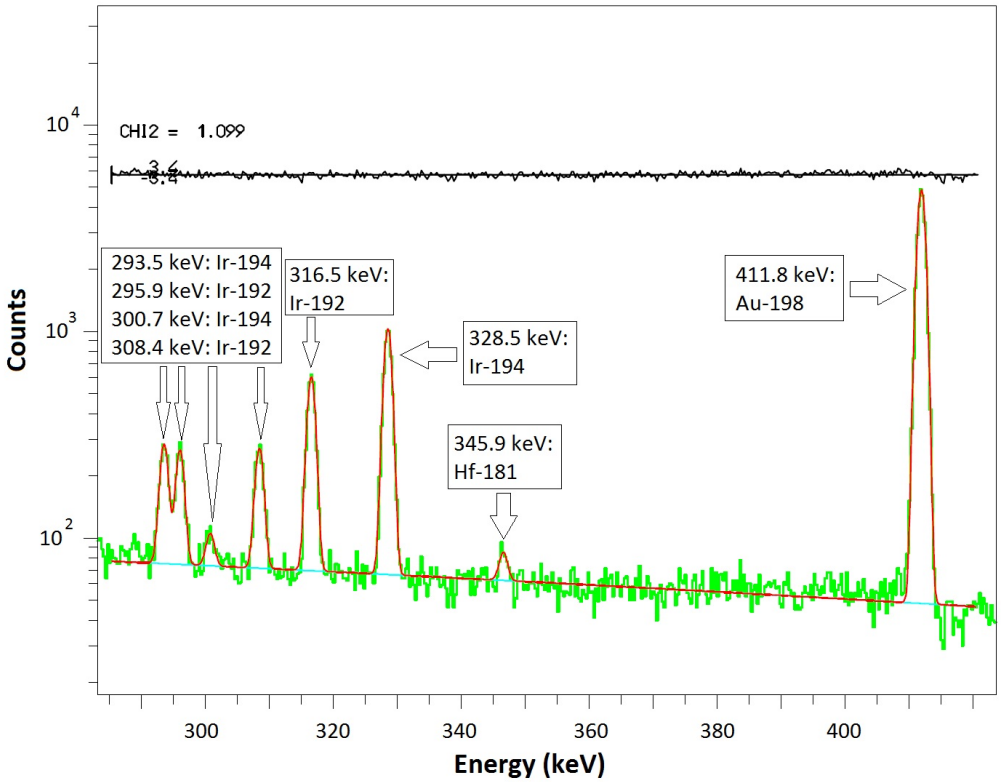

Fig. 3.2: Gaussian fit with background subtraction of some peaks in a STD4 spectrum.

urations the probability of coincidence summing peaks is not negligible at all.

Both the experimental and the simulation spectra were then analyzed using a software which allows to evaluate the number of counts in each observed γ line; in particular, the corresponding peak is fitted with a Gaussian function, which is summed to a polynomial that is used to subtract the underlying background (Fig. 3.2).

In γ-ray spectroscopy, it is possible that different radioisotopes emit γ-rays with the same energy, thus causing peak overlapping. In order to identify these cases and correctly quantify the peak counts, I developed a graphical tool to visualize the relative intensities of the γ lines observed in the experimental and simulation spectra. In this way, when a discrepancy exceeding the possible statistical fluctuations was found for the relative intensity of a certain peak, it was possible to investigate the cause (peaks overlapping, poor statistics, Monte Carlo errors in the description of the decay schemes) and

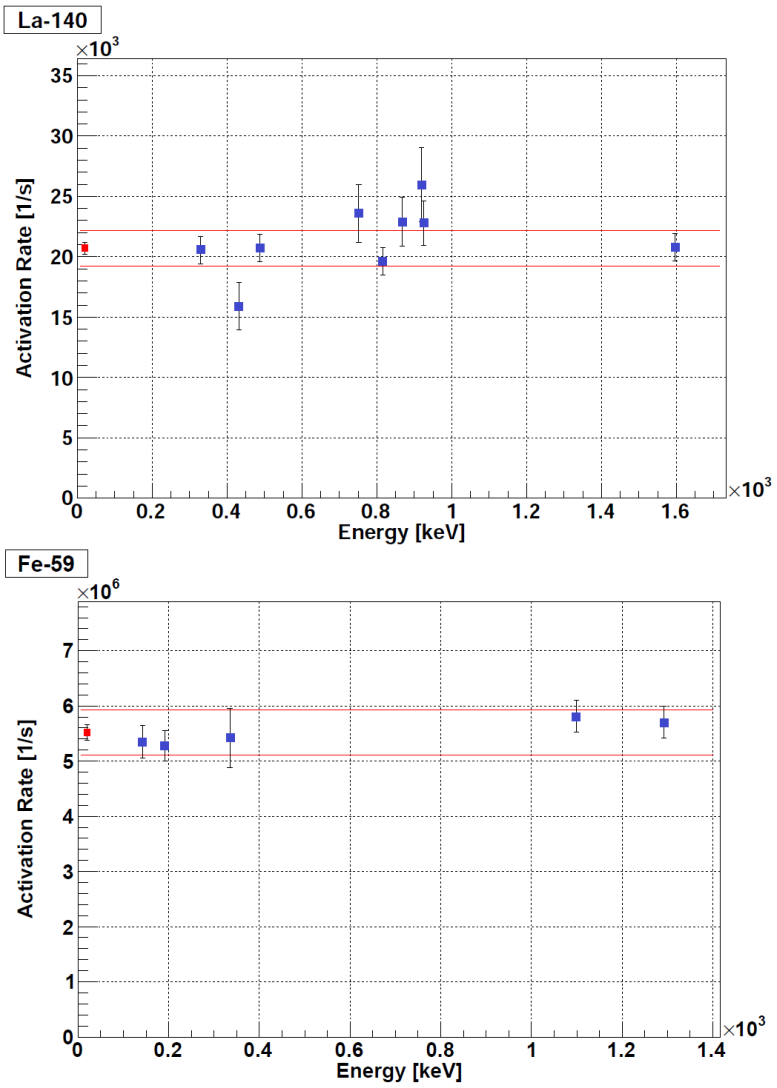

Fig. 3.3: Comparison of the results of ^{140}La and ^{59}Fe activation rate, calculated from the many peak data. The red point is the weighted average value, while the red lines indicate the $\pm 3\,\sigma$ range, where σ is the uncertainty associated with the average.

eventually exclude that peak from the analysis. Anyway, the number of the excluded peaks is small compared to the total and the discrepancy causes have always been identified.

Finally, when multiple γ lines referred to the same radioisotope were observed in a spectrum, their data were combined together to get a more

accurate evaluation of R. In this respect, it is important to consider that the γ-rays are usually emitted with different intensities and the peak counts are known with different precision according to Poisson statistics. For this reason, the uncertainty affecting the evaluation of R from each line was calculated by combining the statistical errors in the measurement and in the simulation, plus a 5% error to keep into account the accuracy level of the HPGe detector Monte Carlo model. The activation rate for a given isotope was thus estimated as the weighted average of the different values obtained from each line in the corresponding spectrum (Fig. 3.3).

3.1.3 Measurement repeatability tests

Before calculating the integral flux results, the reliability of the adopted methodology of analysis was tested by comparing the results of the activation rates measured with different detectors or evaluated from the activation of samples containing a different mass of the same element.

In this respect, it is worth noting that the measurements on different detectors are independent, because the geometries and the Monte Carlo models are different. As a consequence, their comparison can be used to quantify the systematic error associated with a single detector and its corresponding Monte Carlo model.

Comparison of different detectors measurements

To perform this test, the activation rates of the isotopes were firstly evaluated for each detector, averaging the results of the measurements repeated on the same HPGe with different configurations or measuring times. After that, when it was possible to measure the activation rate of an isotope with more than one detector, the independent evaluations of R were compared.

In general, a good agreement was found among the results, confirming the reliability of the GEANT4 Monte Carlo models and of the analysis method. After that, the standard deviation of the R values was used as an evaluation of the systematic error component associated with each detector model. Finally, the mean value of R was calculated for each isotope and the absolute error was estimated by matching the statistical and the systematic errors.

Comparison of samples with different masses

The compatibility of the results from samples containing different amounts of the same element was also investigated. For this purpose, the activation rate per unit mass was calculated. This quantity is equal to the *specific*

SPECIFIC SATURATION ACTIVITY (Bq/g)				
	Central Thimble		Rabbit Channel	
Isotope	Sample 1	Sample 2	Sample 1	Sample 2
	STD2		STD2	
^{46}Sc	$(1.99 \pm 0.10)10^{12}$	$(2.03 \pm 0.15)10^{12}$	$(8.76 \pm 0.49)10^{11}$	$(9.20 \pm 0.51)10^{11}$
^{140}La	$(2.30 \pm 0.05)10^{11}$	$(2.29 \pm 0.04)10^{11}$	$(1.03 \pm 0.03)10^{11}$	$(1.10 \pm 0.04)10^{11}$
^{152}Eu	$(6.02 \pm 0.20)10^{13}$	$(5.79 \pm 0.99)10^{13}$	$(2.80 \pm 0.54)10^{13}$	$(2.80 \pm 0.28)10^{13}$
^{152m}Eu	$(3.34 \pm 0.42)10^{13}$	$(3.22 \pm 0.15)10^{13}$	$(1.43 \pm 0.10)10^{13}$	$(1.45 \pm 0.12)10^{13}$
^{153}Sm	$(2.36 \pm 0.14)10^{12}$	$(2.37 \pm 0.11)10^{12}$	$(9.91 \pm 0.62)10^{11}$	$(1.10 \pm 0.08)10^{12}$
^{154}Eu	$(4.60 \pm 0.12)10^{12}$	$(4.60 \pm 0.36)10^{12}$	$(1.76 \pm 0.18)10^{12}$	$(2.88 \pm 0.25)10^{12}$
^{160}Tb	$(1.12 \pm 0.10)10^{12}$	$(1.11 \pm 0.06)10^{12}$	$(4.86 \pm 0.62)10^{11}$	$(4.85 \pm 0.38)10^{11}$
^{166}Ho	$(2.36 \pm 0.17)10^{12}$	$(2.27 \pm 0.08)10^{12}$	$(9.86 \pm 0.83)10^{11}$	$(1.05 \pm 0.04)10^{12}$
^{177}Lu	$(2.28 \pm 0.21)10^{12}$	$(2.28 \pm 0.22)10^{12}$	$(8.99 \pm 0.88)10^{11}$	$(9.77 \pm 0.72)10^{11}$
^{233}Pa	$(2.14 \pm 0.15)10^{11}$	$(2.01 \pm 0.13)10^{11}$	$(8.50 \pm 0.72)10^{10}$	$(9.20 \pm 0.81)10^{10}$
	STD3		STD3	
^{51}Cr	$(4.68 \pm 0.45)10^{10}$	$(5.67 \pm 0.62)10^{10}$	$(2.24 \pm 0.19)10^{10}$	$(2.87 \pm 0.17)10^{10}$
^{60}Co	$(2.50 \pm 0.24)10^{12}$	$(2.88 \pm 0.26)10^{12}$	$(1.09 \pm 0.12)10^{12}$	$(1.46 \pm 0.42)10^{12}$
^{72}Ga	$(1.27 \pm 0.05)10^{11}$	$(1.31 \pm 0.05)10^{11}$	$(5.58 \pm 0.28)10^{10}$	$(5.09 \pm 0.14)10^{10}$
^{75}Se	$(3.37 \pm 0.25)10^{10}$	$(3.29 \pm 0.48)10^{10}$	$(1.48 \pm 0.17)10^{10}$	$(1.41 \pm 0.13)10^{10}$
^{76}As	$(3.59 \pm 0.21)10^{11}$	$(3.67 \pm 0.11)10^{11}$	$(1.55 \pm 0.09)10^{11}$	$(1.41 \pm 0.09)10^{11}$
^{110m}Ag	$(1.29 \pm 0.13)10^{11}$	$(1.24 \pm 0.06)10^{11}$	$(5.11 \pm 0.11)10^{10}$	$(5.32 \pm 0.62)10^{10}$
^{114m}In	$(2.65 \pm 0.27)10^{10}$	$(3.19 \pm 0.16)10^{10}$	$(1.21 \pm 0.13)10^{10}$	$(1.24 \pm 0.07)10^{10}$
^{115}Cd	$(1.04 \pm 0.09)10^{10}$	$(1.16 \pm 0.05)10^{10}$	$(4.67 \pm 0.51)10^{9}$	$(3.70 \pm 0.30)10^{9}$
^{134}Cs	$(1.38 \pm 0.04)10^{12}$	$(1.51 \pm 0.12)10^{12}$	$(6.12 \pm 0.28)10^{11}$	$(5.69 \pm 0.61)10^{11}$
^{239}Np	$(2.60 \pm 0.19)10^{11}$	$(2.82 \pm 0.16)10^{11}$	$(1.14 \pm 0.06)10^{11}$	$(1.07 \pm 0.09)10^{11}$
	STD4		STD4	
^{103}Ru	$(1.43 \pm 0.05)10^{10}$	$(1.78 \pm 0.12)10^{10}$	$(7.95 \pm 0.81)10^{9}$	$(8.25 \pm 0.43)10^{9}$
^{122}Sb	$(3.12 \pm 0.09)10^{11}$	$(3.33 \pm 0.19)10^{11}$	$(1.45 \pm 0.10)10^{11}$	$(1.55 \pm 0.05)10^{11}$
^{124}Sb	$(1.40 \pm 0.06)10^{11}$	$(1.61 \pm 0.21)10^{11}$	$(6.49 \pm 0.51)10^{10}$	$(6.82 \pm 0.43)10^{10}$
^{175}Hf	$(1.63 \pm 0.09)10^{10}$	$(1.82 \pm 0.12)10^{10}$	$(8.26 \pm 0.47)10^{9}$	
^{181}Hf	$(1.07 \pm 0.12)10^{11}$	$(1.31 \pm 0.37)10^{11}$	$(5.69 \pm 0.91)10^{10}$	$(5.49 \pm 0.89)10^{10}$
^{192}Ir	$(7.05 \pm 0.27)10^{12}$	$(7.52 \pm 0.41)10^{12}$	$(3.51 \pm 0.26)10^{12}$	$(3.70 \pm 0.21)10^{12}$
^{194}Ir	$(2.19 \pm 0.09)10^{12}$	$(2.29 \pm 0.12)10^{12}$	$(1.05 \pm 0.05)10^{12}$	$(1.10 \pm 0.04)10^{12}$
^{198}Au	$(3.43 \pm 0.21)10^{12}$	$(3.53 \pm 0.31)10^{12}$	$(1.61 \pm 0.13)10^{12}$	$(1.68 \pm 0.14)10^{12}$
	Germanium		Germanium	
^{77}As	$(7.84 \pm 0.31)10^{8}$	$(7.93 \pm 0.26)10^{8}$	$(3.13 \pm 0.14)10^{8}$	$(3.67 \pm 0.13)10^{8}$
^{77}Ge	$(7.23 \pm 0.57)10^{8}$	$(7.50 \pm 0.37)10^{8}$	$(2.84 \pm 0.27)10^{8}$	$(3.42 \pm 0.28)10^{8}$

Tab. 3.4: Comparison of the SSA of the isotopes activated in the replicated samples irradiated in Central Thimble and Rabbit Channel. In the couple of data the ones at left refer to the samples with higher mass.

saturation activity[4] (SSA), i.e. the activity per unit mass which would be reached at saturation, when $t_{irr} \gg \tau_{\frac{1}{2}}$.

The results of this analysis are presented in Tab. 3.4 for the cases of Central Thimble and Rabbit Channel, where replicated samples with the same elemental composition but different masses were irradiated. Since it was found a very good agreement in the results, it was not necessary to prepare replicated samples for the irradiations which were performed a few months later in Lazy Susan and Thermal Channel.

3.1.4 Integral flux results

Finally, in order to evaluate the integral neutron flux, for each isotope activated through (n,γ) capture reaction, the best estimate of the specific saturation activity was calculated as the weighted average of the SSA results from the replicated samples (if available). The results of the SSA measured in all the samples activated in the four irradiation facilities are reported in appendix (Tab. A.1).

The neutron flux was then evaluated from Eq. 3.2 combining the activation rate data with the effective cross sections values, that were calculated thanks to the MCNP simulations of the neutron spectrum distributions in the four irradiation facilities. In this respect, it is worth saying that, at the moment, only the statistical error component from Monte Carlo simulations was included in the evaluation of the effective cross section uncertainty[5].

The neutron flux results, obtained from all the analyzed radioisotopes using the ENDF/B-VII cross sections, are reported in appendix (Tab. A.2) and presented in Fig. 3.4.

For most isotopes, there is good agreement among the results: this means that the neutron energetic distributions estimated through MCNP simulations are correct and allow a precise evaluation of the effective cross sections.

However, for some isotopes, significant deviations are observed with respect to the mean value. Several factors may act to produce these errors: in some cases it was not possible to measure an isotope with all three detectors and the error bar does not include the systematic component, in other cases there could be uncertainties related to the isotopic abundance, the metastable state activation probability, the self-shielding effect [31] or the activation cross section. In this respect, it is important to point out that

[4] This is the name conventionally adopted to refer to the activation rate per unit mass in neutron activation analysis.

[5] A refined analysis, which also includes the cross section uncertainties published in the data repositories, will be presented in the next section.

this analysis was performed including all the measured isotopes, even those that are not considered as *standard* in nuclear activation.

Anyway, taking into account these observation, it can be stated that all the measurements and the analysis were performed with particular care to minimize the possible systematic errors, as demonstrated through the use of three different HPGe detectors and replicated samples. The individual results from the 30 analyzed isotopes show that the remaining uncertainties, that are not attributable to the γ-ray spectroscopy analysis and sample preparation, are of the order of 10%. In fact, taking the standard deviation of the flux evaluations with different isotopes as the overall uncertainty, the relative errors of the integral fluxes in the four irradiation facilities are between 10% and 14% (Tab. 3.5).

In the next section, it will be shown that it is possible to improve the precision of the integral flux evaluation by using a refined analysis model in which the flux is subdivided in energy groups and the neutron cross section uncertainties are included in the calculation.

Irradiation facility	Measured Flux $[n/(s \cdot cm^2)]$	Relative error
Central Thimble	$(1.72 \pm 0.17)\, 10^{13}$	10%
Rabbit Channel	$(7.40 \pm 0.95)\, 10^{12}$	13%
Lazy Susan	$(2.40 \pm 0.24)\, 10^{12}$	10%
Thermal Channel	$(2.52 \pm 0.36)\, 10^{11}$	14%

Tab. 3.5: Mean values and standard deviations of the integral neutron flux results in the four irradiation facilities.

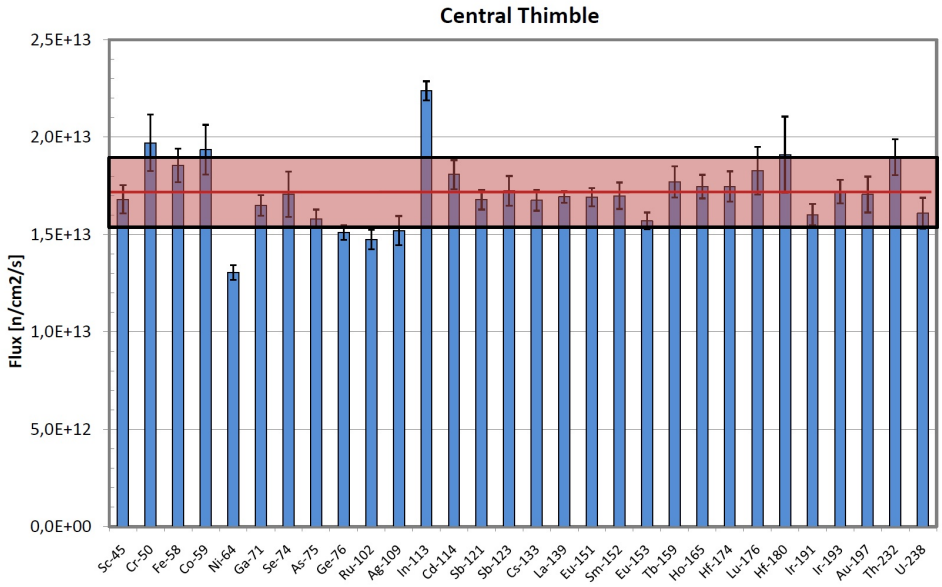
Central Thimble
Flux [n/cm2/s]
2,5E+13
2,0E+13
1,5E+13
1,0E+13
5,0E+12
0,0E+00
Sc-45
Cr-50
Fe-58
Co-59
Ni-64
Ga-71
Se-74
As-75
Ge-76
Ru-102
Ag-109
In-113
Cd-114
Sb-121
Sb-123
Cs-133
La-139
Eu-151
Sm-152
Eu-153
Tb-159
Ho-165
Hf-174
Lu-176
Hf-180
Ir-191
Ir-193
Au-197
Th-232
U-238

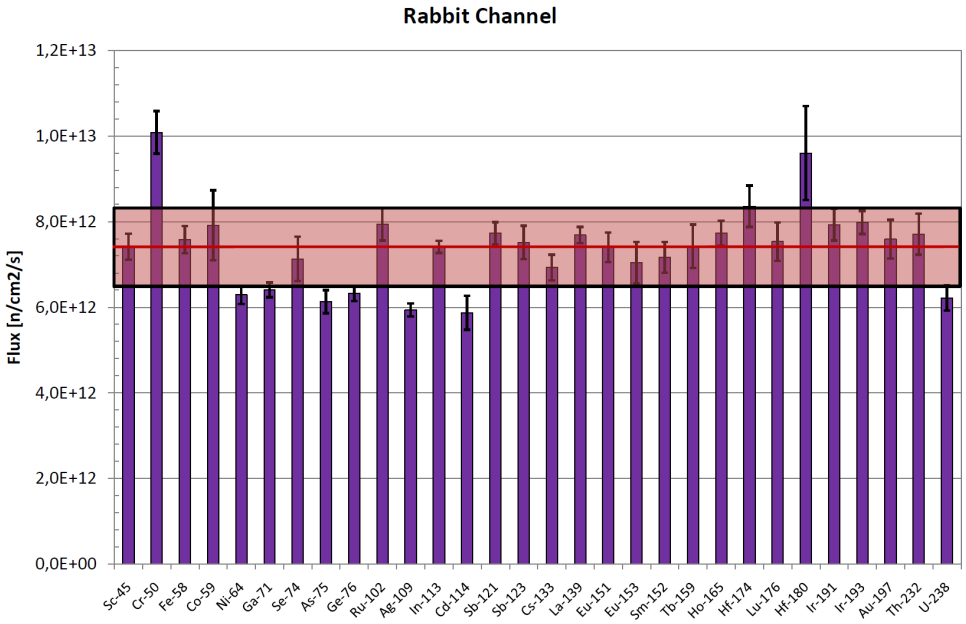
Rabbit Channel
Flux [n/cm2/s]
1,2E+13
1,0E+13
8,0E+12
6,0E+12
4,0E+12
2,0E+12
0,0E+00
Sc-45
Cr-50
Fe-58
Co-59
Ni-64
Ga-71
Se-74
As-75
Ge-76
Ru-102
Ag-109
In-113
Cd-114
Sb-121
Sb-123
Cs-133
La-139
Eu-151
Eu-153
Sm-152
Tb-159
Ho-165
Hf-174
Lu-176
Hf-180
Ir-191
Ir-193
Au-197
Th-232
U-238

Fig. 3.4: Comparison of the neutron flux results evaluated from the data of each precursor isotope in the four irradiation facilities. The shadowed area corresponds to $\pm 1\,\sigma$ range from the mean value, where σ is the standard deviation of the results.

3.2 Neutron flux spectrum analysis using Bayesian statistics

Radioactivation techniques are commonly applied for different applications, concerning not only reactor physics, but also other fields of analysis which require that a sample is irradiated with a neutron flux[6].

As shown in the previous section, when performing a neutron activation experiment, the spectrum distribution is a crucial information to know for a correct interpretation of the experimental data, because the interaction cross sections depend on the neutron energy. In order to provide a benchmark for the models implemented to calculate the effective cross sections, the experimental data of different activated isotopes can be combined to analyze the neutron flux spectrum.

In mathematical terms, the flux spectrum has to be subdivided into n energy groups ($\phi_i^{gr} \equiv \int_{E_i}^{E_{i+1}} \varphi(E)\, dE$) and a linear system of m activation equations must be solved:

$$\frac{R_j}{\mathcal{N}_j} = \sum_{i=1}^{n} \sigma_{ij}^{gr}\, \phi_i^{gr} \quad j = 1, \ldots, m \tag{3.7}$$

where m represents the number of different activated isotopes and σ_{ij}^{gr} are the *group effective cross sections*, defined by limiting the integrals in Eq. 3.2 to the i-th group energies. Theoretically, with a set of m linearly independent equations and the groups chosen such that σ_{ij}^{gr} have little dependence on the neutron flux spectrum, it is possible to determine up to m energy group fluxes.

However the experimental errors, associated with uncertainties both in available cross section data and in the measured values of the activation rates, introduce limitations on the mathematical techniques that can be successfully adopted to solve Eq. 3.7. Computer codes based on automated iterative perturbation methods have been developed in the past to deal with this problem [33]. These codes provide a "best fit" neutron flux spectrum for a given input set of activated isotope data, using a *guess spectrum* as starting point for the subsequent iterations. However, with this approach, it is difficult to assess the final uncertainties associated with the energy group fluxes and their possible correlations; furthermore, the dependence of the obtained results on the guess spectrum must be evaluated.

[6] For example, the neutron activation can be used for analyzing the contaminants in high purity materials or the trace elements in environmental matrices [30]; moreover, the TRIGA Mark II reactor in Pavia has been recently exploited for producing *Neutron Transmutation Doped* (NTD) germanium thermistors used in particle physics experiments [32].

In order to overcome this problem, I proposed to apply the Bayesian inference technique to sample the *joint probability distribution function* (JPDF) of the energy group fluxes ϕ_i^{gr}, given the experimental data and the uncertainties of reaction rates and group cross sections. This method allows to determine the group flux mean values and uncertainties by analyzing each ϕ_i^{gr} probability distribution function (*pdf*), obtained by marginalizing the JPDF. The advantage of this approach is that the analysis model intrinsically includes the uncertainties and combines all experimental data with the correct weights. Moreover, if the group subdivision is properly chosen, the initial spectrum that must be used to calculate the group effective cross sections, has negligible influence on the results.

Bayesian statistical analysis

Bayesian statistics [34] are based on the following interpretation of the Bayes' theorem, which is usually written in the form:

$$P(\theta|data) = \frac{P(data|\theta)}{P(data)} P(\theta) \tag{3.8}$$

where θ is some parameter (or a set of parameters) that we want to determine by doing an experiment which has as outcome some *data*. The meaning of the terms is the following:

- $P(data|\theta)$ is the *Likelihood* distribution, i.e. the probability of getting a certain experimental result (*data*), given the value of θ;
- $P(\theta)$ is the so-called *Prior*, a distribution that describes the knowledge about the parameter θ before doing the measurement;
- $P(data)$ is a normalization factor which corresponds to the probability of measuring that particular *data* irrespective of θ value;
- $P(\theta|data)$ is the *Posterior* distribution, that describes the probability of θ, given the measurement results and the *a priori* information.

The purpose of the Bayesian analysis is to determine the Posterior distribution, because it summarizes the knowledge about θ after the measurement, by matching the Prior and the Likelihood distributions. Within this paradigm, the Prior distribution plays a key role. In fact, when performing a measurement, there is always some *a priori* information about θ which can be included in the analysis to help find the solution (for example a range of possible outcomes or the exclusion of negative values for positive physical quantities).

If there is no particular *a priori* information about a parameter, the usual prescription is to use *non-informative* Prior distributions by taking all possible θ values as equiprobable [35]. In this case, if the experimental information included in the Likelihood are truly dominant, it can be shown that the choice of different Prior functions −which assign non-zero probability to the range of possible outcomes− does not affect the Posterior determination, thus supporting the objectivity of the analysis.

In Bayesian data analysis, the Posteriors are usually most conveniently determined through computational techniques based on Markov Chain Monte Carlo (MCMC) simulations [34]. This method consists of drawing sequential values of θ from approximate distributions, that are improved at each step in the sense of converging to the Posterior *pdf*. The key to the method's success is to create a Markov process whose stationary distribution is the specified $P(\theta|data)$ and run the simulation long enough that the distribution of the draws is a good approximation of the Posterior. The Gibbs sampler [36] and the Metropolis-Hastings [37] algorithm allow to generate such Markovian chains and are exploited in different Bayesian inference software. With such approach, the Posterior evaluation is simplified, because no complex multi-variables calculations nor normalization operations are needed: in fact, the marginal distributions are directly obtained from the draw series of each parameter, without the need to calculate integrals. Therefore, it is sufficient to define the statistical model of the problem (by choosing the Likelihood and the Prior distributions) and provide the experimental data and uncertainties.

Statistical model definition

In this paragraph, I will present the statistical model that I used to evaluate the neutron flux spectrum from the activation data of different isotopes. In order to define the problem and solve it, I used JAGS (Just Another Gibbs Sampler) [38], a program for the analysis of Bayesian models which makes use of the Gibbs sampler to perform MCMC simulations. In this program, the Likelihood and Prior distributions of the unknown variables are defined using some basic *pdf* such as the Gaussian, the Uniform and some other distributions. The experimental data, which are treated as random draws from the Likelihoods, are then combined to sample the Posterior JPDF.

The statistical model of the problem was implemented starting from Eq. 3.7: the energy group fluxes (ϕ_i^{gr}) and the group effective cross sections (σ_{ij}^{gr}) are the unknown variables to be determined from the *observed* experimental data of $R_j/\mathcal{N}_j$ (obs_K_j) and σ_{ij}^{gr} ($obs\_\sigma_{ij}^{gr}$). The Likelihoods

were defined using Gaussian distributions $-dnorm(\mu, \sigma)-$ as follows:

$$\begin{aligned} obs\_K_j &\sim dnorm\left(\sum_{i=1}^{n} \sigma_{ij}^{gr}\ \phi_i^{gr}, sigmaK_j\right) \\ obs\_\sigma_{ij}^{gr} &\sim dnorm\left(\sigma_{ij}^{gr}, sigmaXS_j\right) \end{aligned} \tag{3.9}$$

where $sigmaK_j$ are the experimental uncertainties of $R_j/\mathcal{N}_j$, while $sigmaXS_j$ the ones derived from the experimental covariance data associated with cross sections [25]. The symbol $\sim$ defines a stochastic relation: the observed data on the left side are treated as random draws from the Gaussian distributions defined on the right side.

The choice of Gaussian distributions for describing the Likelihoods follows from the Central Limit Theorem, because both the activation and the cross section data are obtained by averaging the results of independent measurements. Moreover, by considering the cross sections as observed experimental data, it is worth noting that their uncertainties are directly included in the model.

Regarding the Prior definition, uniform *non-informative* distributions $-dunif(x^{min}, x^{max})-$ were chosen for both ϕ_i^{gr} and σ_{ij}^{gr} variables:

$$\begin{aligned} \phi_i^{gr} &\sim dunif(\phi_i^{min}, \phi_i^{max}) \\ \sigma_{ij}^{gr} &\sim dunif(0, \sigma_i^{max}) \end{aligned} \tag{3.10}$$

In particular, ϕ_i^{min} and ϕ_i^{max} were set two orders of magnitude smaller and greater than the expected values of ϕ_i^{gr}. Similarly, σ_i^{max} was chosen to include all the σ_{ij}^{gr} values of the different isotopes within a large margin.

Finally, once the experimental data are provided, it is possible to run a MCMC simulation for evaluating the *pdf* of each ϕ_i^{gr} by sampling the Posterior JPDF: $P\left(\phi_i^{gr} | obs\_K_j, obs\_\sigma_{ij}^{gr}\right)$.

3.2.1 Analysis of the neutron spectrum in the TRIGA Mark II reactor facilities

The statistical model described above was then applied to analyze the neutron flux spectra in the four irradiation facilities of the TRIGA Mark II reactor where the activation experiments were performed. In this way, the Bayesian analysis has been tested with different neutron spectra: in fact, in Central Thimble and Rabbit Channel, the fast neutrons with $E > 1$ MeV are a considerable fraction of the integral flux, while in the other two positions the spectrum is expected to be more thermalized depending on the thickness of graphite interposed between the facility and the core region.

Threshold reaction	Central Thimble *SSA* (Bq/g)	Rabbit Channel *SSA* (Bq/g)	Lazy Susan *SSA* (Bq/g)	Thermal Channel *SSA* (Bq/g)
^{70}Ge(n,2n)^{69}Ge	$(4.34 \pm 0.17)10^5$	$(1.43 \pm 0.06)10^5$	$(1.97 \pm 0.20)10^4$	$(8.5 \pm 1.8)10^2$
^{58}Ni(n,pn)^{57}Co	$(8.4 \pm 1.9)10^6$	$(2.72 \pm 0.43)10^6$	$(2.90 \pm 0.15)10^5$	$(1.48 \pm 0.08)10^4$
^{58}Ni(n,2n)^{57}Ni	$(1.26 \pm 0.10)10^5$	$(4.12 \pm 0.43)10^4$	$(5.66 \pm 0.97)10^3$	–
^{204}Pb(n,2n)^{203}Pb	$(4.74 \pm 0.39)10^5$	$(1.29 \pm 0.23)10^5$	$(1.64 \pm 0.14)10^4$	$(1.06 \pm 0.18)10^3$
^{72}Ge(n,p)^{72}Ga	$(7.27 \pm 0.37)10^5$	$(2.54 \pm 0.10)10^5$	$(3.4 \pm 1.1)10^4$	–
^{56}Fe(n,p)^{56}Mn	$(3.92 \pm 0.20)10^7$	$(1.31 \pm 0.08)10^7$	$(2.14 \pm 0.14)10^6$	–
^{60}Ni(n,p)^{60}Co	$(2.85 \pm 0.29)10^7$	$(7.01 \pm 0.93)10^6$	$(1.04 \pm 0.04)10^6$	$(8.87 \pm 0.98)10^4$
^{54}Fe(n,p)^{54}Mn	$(1.75 \pm 0.09)10^8$	$(6.16 \pm 0.40)10^7$	$(9.61 \pm 0.43)10^6$	$(3.67 \pm 0.22)10^5$
^{58}Ni(n,p)^{58}Co	$(2.62 \pm 0.08)10^9$	$(9.12 \pm 0.21)10^8$	$(1.22 \pm 0.06)10^8$	$(5.18 \pm 0.49)10^6$
^{115}In(n,n')^{115m}In	$(3.96 \pm 0.25)10^9$	$(1.25 \pm 0.03)10^9$	$(1.95 \pm 0.06)10^8$	$(8.32 \pm 0.48)10^6$

Tab. 3.6: Specific saturation activities of isotopes produced through threshold reactions.

The *specific saturation activity* data of the 30 isotopes activated though (n, γ) reactions −previously exploited for the integral flux evaluation (Tab. A.1)− were used together with the ones of 10 threshold reactions which provided fundamental information to determine the fast spectrum component (Tab. 3.6).

The Bayesian analysis of the neutron flux spectrum was developed in the following three steps:

A. *fast neutrons* analysis: the spectrum component above 0.5 MeV is separately analyzed with a subdivision in three groups, exploiting the threshold reaction data;

B. *three-group* whole spectrum analysis: the main flux components (thermal, resonance-intermediate and fast) are evaluated by matching the (n, γ) reactions data and the fast spectrum analysis results;

C. *multi-group* spectrum analysis: the number of energy group fluxes is increased for a finer spectrum analysis.

A. Fast Neutrons Analysis

As a first step, I decided to separately analyze the fast component of the neutron spectra. A three-group Bayesian model was implemented with JAGS for the fast spectrum region, with the following energy subdivisions:

$$(0.5 \rightarrow 4 \rightarrow 10 \rightarrow 20) \text{ MeV},$$

chosen to exploit the different thresholds of the reactions.

In order to calculate the group effective cross sections, a spectrum described by the function $\varphi_{fast}(E) = Ae^{-\alpha E}$ was assumed in the energy range under analysis. This assumption is a good approximation for describing the right tail of the prompt neutron energy distribution (see Fig. 1.8) and was also verified by fitting the MCNP flux spectra in the fast region. In particular, the α coefficients obtained for the different irradiation position resulted between 0.65 and 0.82 (in the case of Central Thimble and Lazy Susan, respectively). Anyway, this difference in the α values was verified to be negligible in the evaluation of the fast neutron flux. The group effective cross sections ($obs\_\sigma_{ij}^{gr}$) were then numerically calculated by combining the exponential spectrum with the $\sigma(E)$ data published in the ENDF/B-VII cross section libraries.

After running the JAGS simulations, the marginal Posterior distributions of the group fluxes were drawn in histogram plots and resulted with a well-defined Gaussian shape, as expected by the combination of uniform Priors and Gaussian Likelihoods (Fig. 3.5). Scatter plots were also drawn

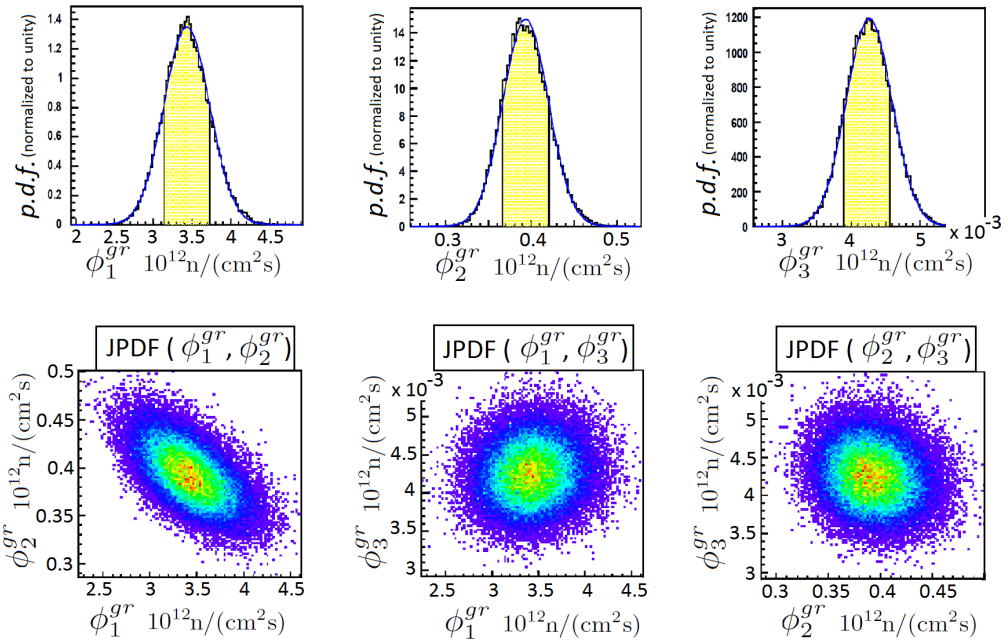

Fig. 3.5: Marginal distributions and scatter plots of the Posterior JPDF obtained for the Central Thimble fast neutron groups (automatic different axis scales). The yellow regions highlight the $\pm 1\,\sigma$ range centred on the mean value of the pdf. Similar plots were obtained from the analysis of the other irradiation facilities.

to analyze the correlation between each couple of variables. In particular, some degree of anti-correlation was observed between the first and the second group, meaning that the sum of these two groups is known more precisely than the single group alone. Finally, the mean and the standard deviation of each group distribution were calculated together with the total fast flux (ϕ_{fast}), that was defined in the simulation as the sum of each drawing triplet of energy group fluxes (Table 3.7).

These first results show that the Bayesian methodology allows to combine experimental data from different threshold reactions and to analyze the fast neutron fluxes with great flexibility and accuracy. The uncertainties obtained for the total fast flux are between 7% and 9% and all the group fluxes resulted with errors less than 13% also for the Thermal Channel, where a reduced number of threshold reactions was observed due to the lower fast neutrons component.

It is worth noting that the errors associated with the fluxes are evaluated by calculating the standard deviation of the corresponding Posterior *pdf*. With this statistical approach, the experimental uncertainties of the activation data and the errors associated with the cross section libraries are both included in the analysis.

Energy Limits (MeV)	Central Thimble Flux $[n/(cm^2s)]$	Rabbit Channel Flux $[n/(cm^2s)]$	Lazy Susan Flux $[n/(cm^2s)]$	Thermal Channel Flux $[n/(cm^2s)]$
$0.5 \rightarrow 4$	$(3.43 \pm 0.30)10^{12}$	$(1.24 \pm 0.11)10^{12}$	$(1.83 \pm 0.17)10^{11}$	$(6.88 \pm 0.86)10^{9}$
$4 \rightarrow 10$	$(3.93 \pm 0.27)10^{11}$	$(1.32 \pm 0.10)10^{11}$	$(2.49 \pm 0.17)10^{10}$	$(1.05 \pm 0.12)10^{9}$
$10 \rightarrow 20$	$(4.26 \pm 0.34)10^{9}$	$(1.52 \pm 0.14)10^{9}$	$(2.80 \pm 0.26)10^{8}$	$(1.27 \pm 0.13)10^{7}$
ϕ_{fast}	$(3.83 \pm 0.28)10^{12}$	$(1.38 \pm 0.10)10^{12}$	$(2.08 \pm 0.16)10^{11}$	$(7.94 \pm 0.79)10^{9}$

Tab. 3.7: Results of the fast neutron spectrum Bayesian analysis with a subdivision in three groups.

B. Three-Group Whole Spectrum Analysis

The second step of the analysis concerned the study of the whole spectrum subdivided in the three main components: thermal, resonance-intermediate and fast neutrons. First of all, the spectra in the four irradiation facilities were analyzed through MCNP simulations in which 135 energy bins were used to tally the neutron flux (Fig. 3.6).

The energy ranges where the spectra show similar shapes were identified to define the main flux groups:

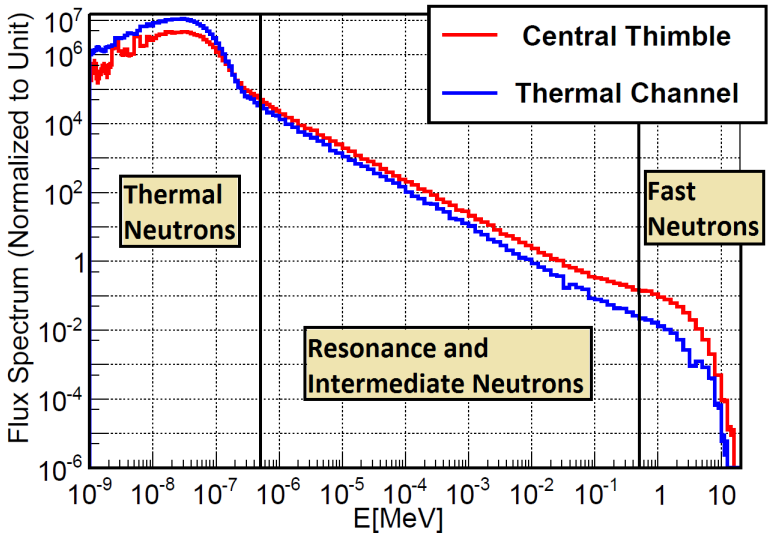

Fig. 3.6: MCNP evaluation of the neutron flux spectrum (normalized to unity) in Central Thimble and Thermal Channel.

- $E < 0.5$ eV: thermal neutrons (Maxwellian spectrum);
- 0.5 eV$< E <$ 0.5 MeV: resonance-intermediate neutrons ($E^{-\beta}$ dependence, with β close to 1);
- $E >$ 0.5 MeV: fast neutrons (approximately $e^{-\alpha E}$ dependence).

It is worth noting that the simulation results are in good agreement with the predictions from the theoretical models describing the diffusion of neutrons in thermal reactors [3]. Therefore, the spectrum shape characterizing each of these three groups is, as a first approximation, something well-known and with poor dependence on the neutron thermalization level in the irradiation position.

This is a crucial point in the analysis, because the calculation of the group effective cross sections (σ_{ij}^{gr}) does not depend on the fraction of flux belonging to each group, but depends on the flux shape within each group. However, it has just been shown that, with this subdivision, the group fluxes are characterized by similar trends even if the irradiation positions are different. For this reason, we can combine the MCNP simulation $\varphi_i^{gr}(E)$ data with the ENDF/B-VII $\sigma(E)$ data to calculate σ_{ij}^{gr}, being poorly dependent on the simulation results used to describe the spectrum distribution.

Afterwards, a three-group JAGS model was implemented to analyze the whole spectrum using the set of 30 (n, γ) activation rate data, referring to an equal number of different isotopes. The results of the fast neutrons Bayesian

analysis were used to define a Gaussian Prior for the 3^{rd} group of neutrons:

$$\phi_3^{gr} \sim dnorm(obs\_\phi_{fast}, sigma\phi_{fast}) \tag{3.11}$$

where $sigma\phi_{fast}$ are the uncertainties associated with the experimental results of the total fast flux (obs_ϕ_{fast}). In this way, the Bayesian analysis returned well-determined results for all three groups (Tab. 3.8), showing how the Prior can be used to flexibly include some experimental results, essential for the problem solution. The Posterior marginal *pdf* show again a Gaussian shape with different widths reflecting the precision of the flux determination for each energy group (Fig. 3.7).

Some degree of anti-correlation was observed between the thermal and the resonance-intermediate neutron groups. The corresponding correlation coefficients, defined by the formula[7]:

$$corr(\phi_i, \phi_j) = \frac{cov(\phi_i, \phi_j)}{\sigma_i \, \sigma_j} \tag{3.12}$$

resulted between -0.51 and -0.64 in the different channels. This is due to the fact that these two groups are the real independent variables of the system: in fact, the group of fast neutrons is constrained by the Prior and resulted completely uncorrelated with the others.

[7] where *cov* is the covariance of two random variables and σ the standard deviation.

	Central Thimble		Rabbit Channel	
	Flux $[n/(cm^2 s)]$	$\%_{gr}$	Flux $[n/(cm^2 s)]$	$\%_{gr}$
ϕ_1^{gr}	$(6.66 \pm 0.09) \times 10^{12}$	39.2%	$(3.14 \pm 0.05) \times 10^{12}$	45.3%
ϕ_2^{gr}	$(6.49 \pm 0.17) \times 10^{12}$	38.3%	$(2.41 \pm 0.08) \times 10^{12}$	34.8%
ϕ_3^{gr}	$(3.81 \pm 0.28) \times 10^{12}$	22.5%	$(1.38 \pm 0.10) \times 10^{12}$	19.9%
Φ_{tot}	$(1.70 \pm 0.03) \times 10^{13}$		$(6.92 \pm 0.12) \times 10^{12}$	
	Lazy Susan		Thermal Channel	
	Flux $[n/(cm^2 s)]$	$\%_{gr}$	Flux $[n/(cm^2 s)]$	$\%_{gr}$
ϕ_1^{gr}	$(1.16 \pm 0.02) \times 10^{12}$	51.7%	$(2.14 \pm 0.06) \times 10^{11}$	88%
ϕ_2^{gr}	$(8.74 \pm 0.32) \times 10^{11}$	39.0%	$(2.11 \pm 0.36) \times 10^{10}$	8.7%
ϕ_3^{gr}	$(2.09 \pm 1.16) \times 10^{11}$	9.3%	$(7.94 \pm 0.79) \times 10^{09}$	3.3%
Φ_{tot}	$(2.24 \pm 0.03) \times 10^{12}$		$(2.43 \pm 0.04) \times 10^{11}$	

Tab. 3.8: Results of whole spectrum Bayesian analysis with a subdivision in three groups.

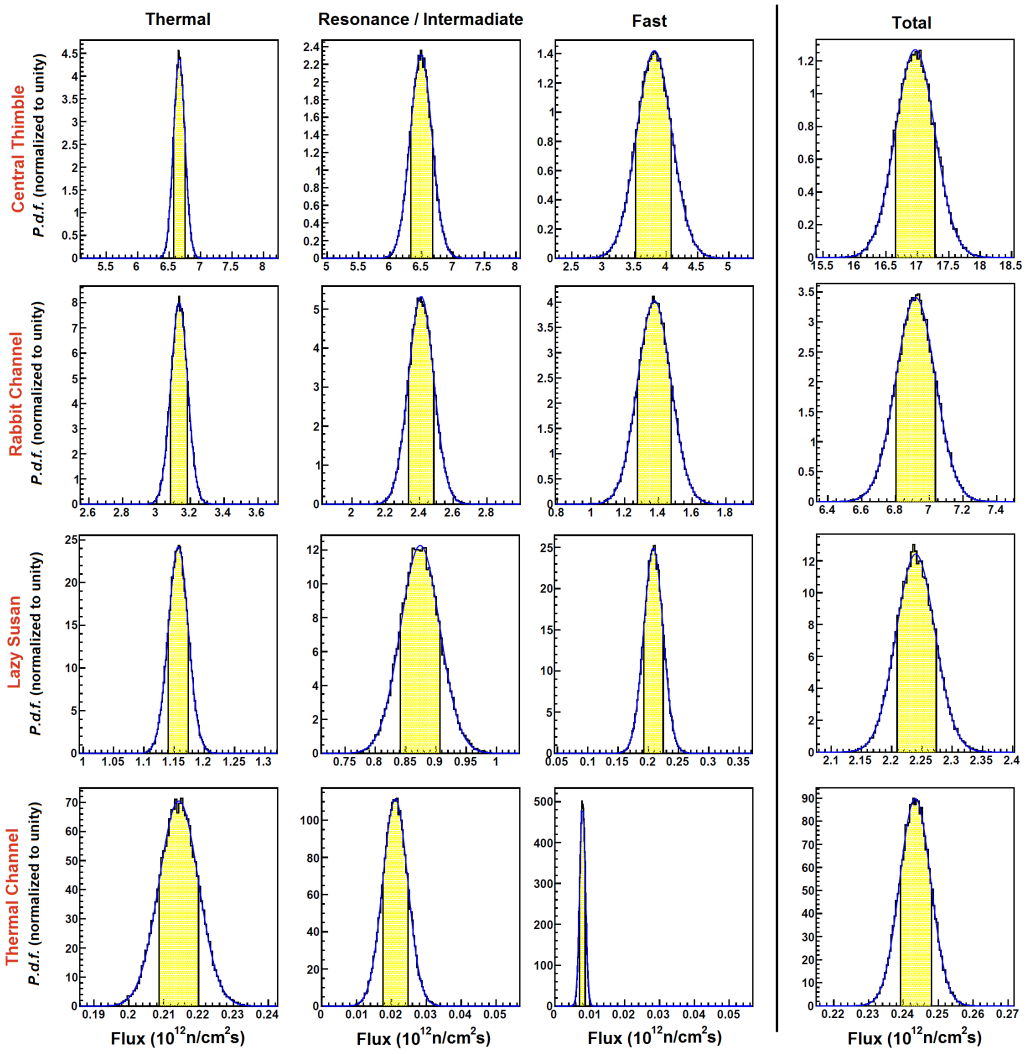

Fig. 3.7: Marginalized distributions of the JPDF Posterior obtained from the three-group whole spectrum Bayesian analysis.

The anti-correlation between the first two groups results in a more precise determination of the integral fluxes, which are reported in Tab. 3.8 together with the group percentages of the total flux. As expected, the thermalization levels are different in each irradiation facility, showing how this methodology can be applied to analyze different neutron spectra.

Finally, in order to test possible dependences on the Prior choice, the analysis was repeated setting uniform Priors on the variables' logarithms, thus assigning equal probability to each order of magnitude. The obtained

results are fully compatible with the previous ones, proving that in this analysis the Likelihood is truly dominant in the Posterior determination.

C. Multi-Group Spectrum Analysis

As a final step in the analysis, I tried to increase the number of energy group intervals in the reconstructed energy spectrum, with the aim of testing the capability of the Bayesian method to converge to well-determined solutions when the unknown variables in the system are augmented. This is possible because we analyzed many isotopes, characterized by different neutron cross sections with extremely large variations in the energy dependence. Therefore, through an appropriate selection of the group energies, it is possible to obtain a system of linearly independent equations in which each isotope provides different information.

For this reason, the cross sections of the activated isotopes were carefully analyzed. At energies below 0.05 eV, all (n,γ) cross sections have $1/v$ dependence, where v is the neutron velocity. This entails that if one tried to separate different groups under this energy, they would result fully correlated and undetermined, because all isotopes provide the same information for this spectrum part. Conversely, at higher energies, the (n,γ) cross sections exhibit resonances at different energies for each isotope, providing the opportunity to define many groups in the resonance region. The group sep-

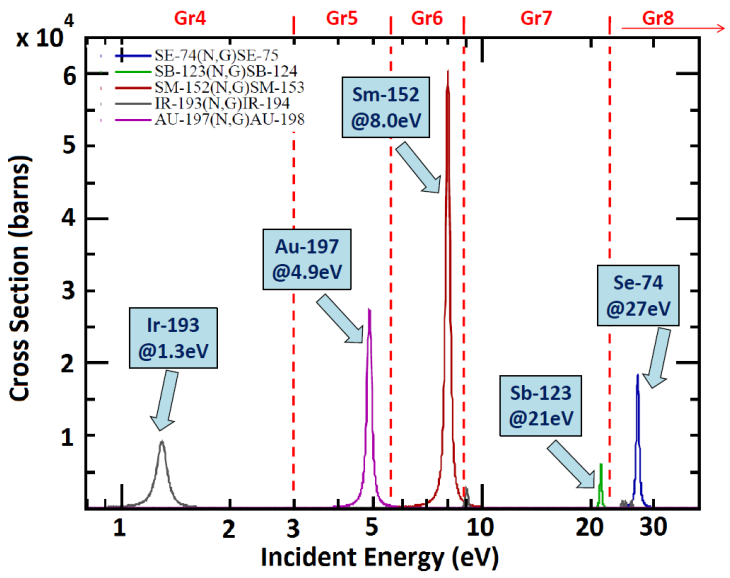

Fig. 3.8: Analysis of the cross section resonances to identify a good set of group separation energies.

aration energies were then carefully chosen so that the highest resonance of each isotope was entirely included in a single group, as shown by way of example in Fig. 3.8 for a subset of isotopes.

In order to check that the subdivisions were properly chosen, the activation percentages due to each group were calculated by combining the cross section data with the neutron spectrum distributions evaluated through the

	Gr. 1	Gr. 2	Gr. 3	Gr. 4	Gr. 5	Gr. 6	Gr. 7	Gr. 8	Gr. 9	Gr. 10
Sc45	63.4%	29.1%	5.2%	1.1%	0.3%	0.2%	0.3%	0.2%	0.3%	0.0%
Cr50	63.3%	29.0%	5.2%	1.1%	0.3%	0.2%	0.3%	0.2%	0.5%	0.0%
Ni64	62.8%	28.8%	5.1%	1.1%	0.3%	0.2%	0.3%	0.2%	1.1%	0.2%
Hf174	63.6%	27.3%	4.0%	0.4%	0.1%	0.0%	1.4%	1.7%	1.4%	0.0%
Lu176	31.3%	57.6%	9.7%	0.7%	0.1%	0.1%	0.1%	0.2%	0.2%	0.0%
Eu151	70.0%	18.7%	9.8%	0.4%	0.4%	0.2%	0.2%	0.2%	0.2%	0.0%
Ir191	51.8%	23.2%	19.3%	0.8%	1.3%	1.7%	0.5%	0.8%	0.7%	0.0%
Ir193	35.1%	17.3%	4.7%	34.0%	0.1%	1.2%	1.7%	3.3%	2.6%	0.0%
Eu153	52.7%	22.5%	3.3%	6.9%	5.2%	1.1%	3.3%	2.2%	2.9%	0.0%
In113	22.1%	10.7%	2.5%	30.1%	2.2%	0.1%	16.9%	8.1%	7.0%	0.4%
Tb159	29.3%	13.5%	2.5%	1.4%	10.7%	0.4%	21.3%	7.4%	13.3%	0.2%
Ho165	37.5%	17.1%	3.1%	1.0%	20.1%	0.3%	8.1%	5.5%	7.3%	0.1%
Au197	30.9%	14.5%	2.8%	1.3%	44.1%	3.8%	0.1%	1.2%	1.4%	0.0%
Ag109	31.7%	14.8%	2.9%	1.2%	24.4%	21.4%	0.1%	2.0%	1.5%	0.0%
Cs133	32.8%	15.2%	2.8%	0.9%	17.4%	21.1%	1.9%	3.1%	4.8%	0.1%
Sb121	18.1%	8.4%	1.6%	0.5%	14.1%	23.8%	19.8%	5.2%	8.2%	0.3%
Sm152	33.0%	15.3%	2.9%	0.9%	0.8%	30.4%	15.6%	0.1%	1.0%	0.0%
U238	8.3%	3.8%	0.7%	0.2%	0.3%	39.7%	11.6%	25.3%	9.9%	0.2%
Sb123	20.8%	9.5%	1.7%	0.4%	0.1%	0.1%	33.4%	24.7%	8.9%	0.4%
Th232	36.4%	16.3%	2.7%	0.4%	0.1%	0.0%	12.5%	15.6%	15.7%	0.5%
Se74	37.2%	17.1%	3.1%	0.7%	0.3%	0.2%	1.2%	38.6%	1.6%	0.0%
As75	32.5%	14.9%	2.7%	0.6%	0.2%	0.1%	0.2%	28.8%	19.9%	0.1%
Ru102	49.2%	22.5%	4.0%	0.9%	0.3%	1.0%	1.3%	6.0%	13.3%	1.6%
La139	60.1%	27.5%	5.1%	1.0%	0.3%	0.1%	0.2%	3.8%	2.0%	0.1%
Hf180	56.5%	25.8%	4.6%	0.9%	0.3%	0.1%	0.2%	5.3%	6.3%	0.1%
Ga71	43.3%	19.9%	3.6%	0.8%	0.2%	0.1%	0.2%	0.2%	31.6%	0.1%
Cd114	15.6%	7.1%	1.3%	0.3%	0.1%	0.1%	0.1%	0.6%	73.4%	1.6%
Ge76	39.6%	18.2%	3.3%	0.7%	0.2%	0.1%	0.2%	0.1%	37.1%	0.6%
Co59	57.1%	26.2%	4.7%	1.0%	0.3%	0.2%	0.3%	0.4%	9.8%	0.0%
Fe58	59.7%	27.4%	4.9%	1.1%	0.3%	0.2%	0.3%	0.2%	6.0%	0.1%

0% 10% 20% 30% 40% 50% 60% 70% 80%

Tab. 3.9: Activation percentages due to each group relating the isotopes activated by (n, γ) reactions in the Central Thimble.

MCNP simulations. In particular it was verified that for each group there was at least one isotope contributing to the activation with a significant percentage, because this condition ensures a better convergence of the equations system. In Tab. 3.9 is shown the case of the Central Thimble with 10 groups subdivided with the following energy intervals:

$$0 \text{ eV} \rightarrow 0.05 \text{ eV} \rightarrow 0.15 \text{ eV} \rightarrow 0.8 \text{ eV} \rightarrow 3 \text{ eV} \rightarrow 5.6 \text{ eV} \rightarrow$$
$$\rightarrow 9 \text{ eV} \rightarrow 23 \text{ eV} \rightarrow 75 \text{ eV} \rightarrow 0.5 \text{ MeV} \rightarrow 20 \text{ MeV}$$

Afterwards, a JAGS model was implemented to solve the system with the aforementioned group subdivision. As in the case of the three-group whole spectrum analysis, a constraining Gaussian Prior was defined for the 10^{th} group of fast neutrons with energies above 0.5 MeV. The group effective cross sections were calculated again using the ENDF/B-VII cross section data and the MCNP simulation results for the $\varphi_i^{gr}(E)$ distributions. In this case, the dependence of the group flux results on the MCNP spectrum is further reduced, because a finer energy subdivision is used and the system has more degrees of freedom.

The results of the 10 groups Bayesian analysis of Central Thimble and Rabbit Channel spectra are shown in Fig. 3.9 and listed in Tab. 3.10, where the relative percent errors associated with each group are also reported. This analysis model allowed to determine with good precision (around 10%) most of the group fluxes and anyway the uncertainties −equal to the standard deviation of the Posterior distributions− did not exceed 26%. Moreover, the reliability of the results is supported by the fact that all the Posterior marginal *pdf* resulted with a well-defined Gaussian shape and that the in-

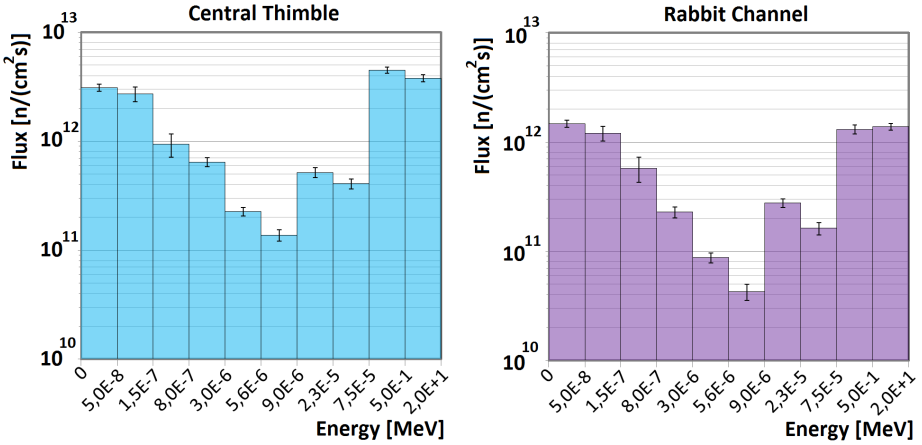

Fig. 3.9: Central Thimble and Rabbit Channel multi-group analysis results.

Energy Limits (eV)	Central Thimble Flux $[n/(cm^2s)]$	$\epsilon_r\%$	Rabbit Channel Flux $[n/(cm^2s)]$	$\epsilon_r\%$
$0 \rightarrow 0.05$	$(3.09 \pm 0.23)10^{12}$	7.5	$(1.47 \pm 0.11)10^{12}$	7.2
$0.05 \rightarrow 0.15$	$(2.72 \pm 0.42)10^{12}$	15	$(1.21 \pm 0.19)10^{12}$	16
$0.15 \rightarrow 0.8$	$(9.43 \pm 2.27)10^{11}$	24	$(5.77 \pm 1.50)10^{11}$	26
$0.8 \rightarrow 3$	$(6.45 \pm 0.62)10^{11}$	9.7	$(2.28 \pm 0.26)10^{11}$	11
$3 \rightarrow 5.6$	$(2.27 \pm 0.21)10^{11}$	9.1	$(8.76 \pm 0.92)10^{10}$	10
$5.6 \rightarrow 9$	$(1.38 \pm 0.16)10^{11}$	12	$(4.27 \pm 0.73)10^{10}$	17
$9 \rightarrow 23$	$(5.17 \pm 0.55)10^{11}$	10	$(2.77 \pm 0.25)10^{11}$	9.1
$23 \rightarrow 75$	$(4.07 \pm 0.44)10^{11}$	11	$(1.62 \pm 0.21)10^{11}$	13
$75 \rightarrow 0.5M$	$(4.50 \pm 0.31)10^{12}$	6.8	$(1.31 \pm 0.13)10^{12}$	9.6
$0.5M \rightarrow 20M$	$(3.80 \pm 0.28)10^{12}$	7.4	$(1.38 \pm 0.10)10^{12}$	7.2
Φ_{tot}	$(1.70 \pm 0.05)10^{13}$	2.8	$(6.74 \pm 0.19)10^{12}$	2.9

Tab. 3.10: Central Thimble and Rabbit Channel multi-group analysis results.

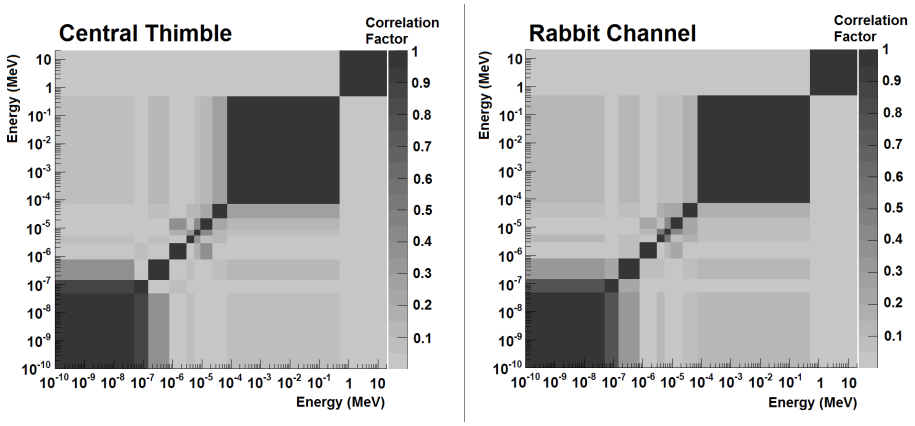

Fig. 3.10: Correlation matrices of Central Thimble and Rabbit Channel multi-group spectrum analysis.

tegral flux values are compatible with the ones evaluated with the previous three-group analysis.

In order to analyze the correlations, matrices were drawn representing the absolute values of the correlation coefficients calculated for each couple of group fluxes (Fig. 3.10). In both cases, a significant correlation was observed between the first two groups of thermal neutrons, while in the resonance energy region the correlation coefficients are generally low, confirming that the Bayesian methodology succeeded in solving the system by exploiting the experimental data from isotopes characterized by resonances at different energies.

The multi-group Bayesian analysis was also applied to the Lazy Susan and Thermal Channel data. In these cases, the 10 groups subdivision did not succeeded in determining all the group fluxes, due to the higher thermalization level in these irradiation positions.

Particularly, when using the 10 groups model in the case of Lazy Susan, the 3^{rd} group between 0.15 eV and 0.8 eV was not well determined. In fact, its Posterior distribution resulted with a standard deviation around 33% and the left tail of the Gaussian was cut off for negative values, as forced by the Prior. Therefore, 9 group JAGS model was implemented with a unique group between 0.15 eV and 3 eV. With this change, all the Posterior marginal

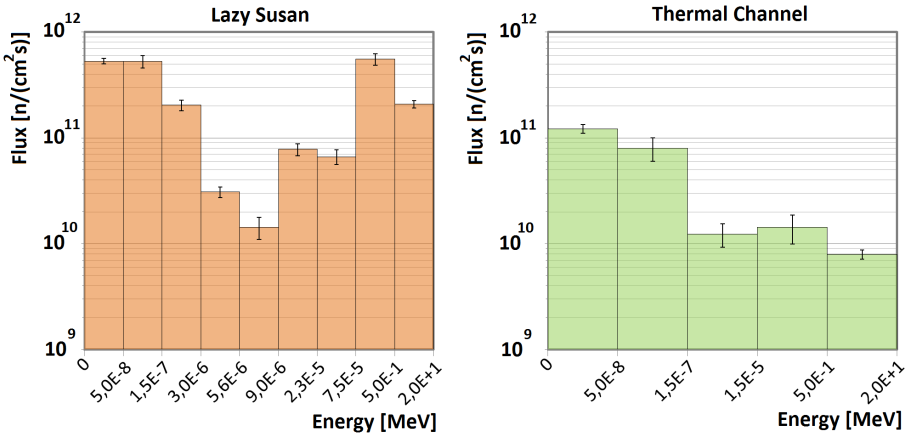

Fig. 3.11: Lazy Susan and Thermal Channel multi-group analysis results.

Energy Limits (eV)	Lazy Susan Flux $[n/(cm^2s)]$	$\epsilon_r\%$
$0 \rightarrow 0.05$	$(5.30 \pm 0.31)10^{11}$	5.8
$0.05 \rightarrow 0.15$	$(5.29 \pm 0.70)10^{11}$	13
$0.15 \rightarrow 3$	$(2.04 \pm 0.24)10^{11}$	12
$3 \rightarrow 5.6$	$(3.08 \pm 0.35)10^{10}$	11
$5.6 \rightarrow 9$	$(1.43 \pm 0.33)10^{10}$	23
$9 \rightarrow 23$	$(7.80 \pm 1.02)10^{10}$	13
$23 \rightarrow 75$	$(6.64 \pm 1.05)10^{10}$	16
$75 \rightarrow 0.5M$	$(5.54 \pm 0.70)10^{11}$	13
$0.5M \rightarrow 20M$	$(2.08 \pm 0.16)10^{11}$	7.7
Φ_{tot}	$(2.21 \pm 0.07)10^{12}$	3.1

Energy Limits (eV)	Thermal Channel Flux $[n/(cm^2s)]$	$\epsilon_r\%$
$0 \rightarrow 0.05$	$(1.22 \pm 0.11)10^{11}$	9.4
$0.05 \rightarrow 0.15$	$(8.01 \pm 2.00)10^{10}$	25
$0.15 \rightarrow 15$	$(1.24 \pm 0.31)10^{10}$	25
$15 \rightarrow 0.5M$	$(1.43 \pm 0.44)10^{10}$	31
$0.5M \rightarrow 20M$	$(7.94 \pm 0.79)10^{9}$	9.9
Φ_{tot}	$(2.36 \pm 0.10)10^{11}$	4.4

Tab. 3.11: Lazy Susan and Thermal Channel multi-group analysis results.

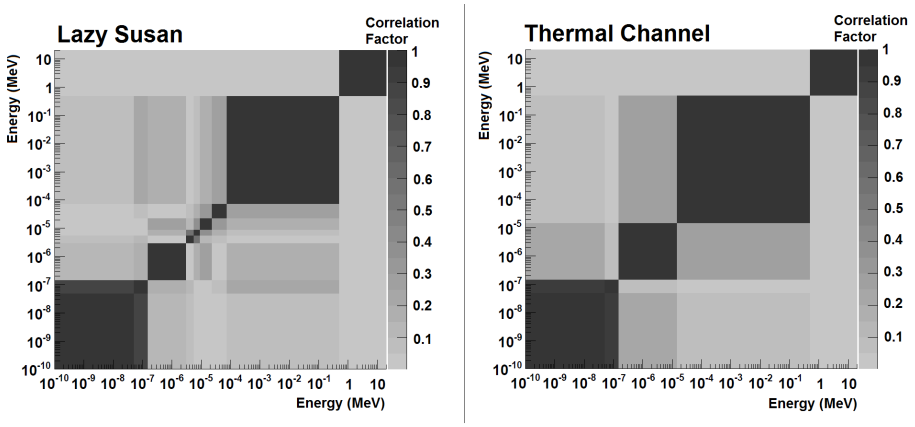

Fig. 3.12: Correlation matrices of Lazy Susan and Thermal Channel multi-group spectrum analysis.

distributions resulted with a symmetric Gaussian shape and all the group fluxes were determined with good precision.

In the case of the Thermal Channel −in which the resonance-intermediate flux component was evaluated to be only the 8.7% of the total flux− it was possible to determine at most five groups. The results of both analysis are presented in Tab. 3.11 and in Fig. 3.11, while the correlation matrices can be viewed in Fig. 3.12.

These results show that the Bayesian approach can be successfully applied to analyze different spectra, provided that the group fluxes are properly chosen. If the degrees of freedom are too many, the equation system is undetermined and the analysis model does not converge to precise solutions. In this way, the Bayesian methodology highlights which is the maximum number of groups that can be determined according to the effective information included in the experimental data.

3.2.2 Multi-group spectrum analysis with prior constraints

In this section I will present an alternative Bayesian model definition that allows to determine the multi-group fluxes by exploiting the *a priori* informations that can be obtained through a previous analysis of the spectrum main components. In particular, the variables representing the thermal, resonance-intermediate and fast fluxes are defined with the following Priors:

$$\begin{aligned} \phi_{th} &\sim dnorm(obs\_\phi_{th},\ sigma\phi_{th}) \\ \phi_{res} &\sim dnorm(obs\_\phi_{res},\ sigma\phi_{res}) \\ \phi_{fast} &\sim dnorm(obs\_\phi_{fast},\ sigma\phi_{fast}) \end{aligned} \tag{3.13}$$

where the observed values and uncertainties of ϕ_{th}, ϕ_{res} and ϕ_{fast} are assumed to be equal to the results of a Bayesian three-group analysis. The multi-group model is then defined by replacing the summation in Eq. 3.9 with the following expression:

$$\phi_{th}\left[\sum_{i=1}^{n_{th}}\sigma_{ij}^{gr}\ f_i\right] + \phi_{res}\left[\sum_{i=n_{th}+1}^{N-1}\sigma_{ij}^{gr}\ f_i\right] + \phi_{fast}\sigma_{Nj}^{gr} \tag{3.14}$$

where n_{th} and N symbolize the number of groups in the thermal region and in the whole spectrum, respectively. On the other hand, f_i are the fractions of each group flux respect to the thermal or the resonance-intermediate component:

$$\begin{cases} f_i = \dfrac{\phi_i^{gr}}{\phi_{th}} & i = 1, \ldots, n_{th} \\ \\ f_i = \dfrac{\phi_i^{gr}}{\phi_{res}} & i = n_{th}+1, \ldots, N-1 \end{cases} \tag{3.15}$$

Uniform Prior distributions in the range $(0, 1)$ were defined for all the fractions f_i, except for two of them, that were forced to satisfy the following normalization conditions:

$$\sum_{i=1}^{n_{th}} f_i = 1 \qquad \sum_{i=n_{th}+1}^{N-1} f_i = 1 \tag{3.16}$$

In this way the number of system's free variables is the same as in the JAGS models previously discussed, provided that the number of groups is kept the same.

With this new model −thanks to the more constraining Prior definitions− more information is provided to the groups belonging to the thermal and resonance regions. For this reason, it was possible to solve an 11 groups model for the Central Thimble, Rabbit Channel and Lazy Susan spectra. In particular, a subdivision at 750 eV was added to the previous 10 groups energy limits. In this way, 3 subgroups were defined in the thermal region and 7 in the resonance-intermediate one:

$$\begin{cases} Thermal & 0 \text{ eV} \rightarrow 0.05 \text{ eV} \rightarrow 0.15 \text{ eV} \rightarrow 0.8 \text{ eV} \\ Res - Int & 0.8 \text{ eV} \rightarrow 3 \text{ eV} \rightarrow 5.6 \text{ eV} \rightarrow 9 \text{ eV} \rightarrow 23 \text{ eV} \\ & \rightarrow 75 \text{ eV} \rightarrow 750 \text{ eV} \rightarrow 0.5 \text{ MeV} \\ Fast & 0.5 \text{ MeV} \rightarrow 20 \text{ MeV} \end{cases}$$

Regarding the Thermal Channel, it was not possible to increase the number of groups, therefore this different analysis model was tested with the same 5 groups subdivision as before and the energy limit between thermal and resonance neutrons was set at 0.15 eV instead of 0.8 eV.

After solving three-group JAGS models to determine the Priors parameters for ϕ_{th}, ϕ_{res} and ϕ_{fast} variables (see Tab. 3.12), the results of this different multi-group spectrum analysis were compared with the ones from MCNP simulations, as shown in the next section (see Fig. 3.13 and Tab. 3.13, 3.14, 3.15, and 3.16).

Looking at the results obtained with this different multi-group model, it is important to remark that they are fully compatible with the previous ones, proving that the system converges to the same solutions independently of the model definition. Moreover, the uncertainties associated to the group fluxes are generally lower, showing that this analysis model, through the introduction of more constraining Priors, is more robust and allows the determination of the results with higher precision.

Irradiation	$\phi_{th}[n/(cm^2s)]$	$\phi_{res}[n/(cm^2s)]$	$\phi_{fast}[n/(cm^2s)]$
Facility	0 eV → 0.8 eV	0.8 eV → 0.5 MeV	0.5 MeV → 20 MeV
Central Thimble	$(6.92 \pm 0.15)10^{12}$	$(6.29 \pm 0.18)10^{12}$	$(3.83 \pm 0.28)10^{12}$
Rabbit Channel	$(3.25 \pm 0.07)10^{12}$	$(2.33 \pm 0.08)10^{12}$	$(1.38 \pm 0.10)10^{12}$
Lazy Susan	$(1.22 \pm 0.03)10^{12}$	$(8.34 \pm 0.37)10^{11}$	$(2.09 \pm 0.16)10^{11}$
	0 eV → 0.15 eV	0.15 eV → 0.5 MeV	0.5 MeV → 20 MeV
Thermal Channel	$(2.06 \pm 0.06)10^{11}$	$(2.64 \pm 0.45)10^{10}$	$(7.94 \pm 0.79)10^{9}$

Tab. 3.12: Results of the three-group JAGS models used to determine the Prior parameters for the multi-group spectrum analysis.

3.2.3 Benchmark analysis of the simulation spectra

With the aim of providing a benchmark for the MCNP reactor model exploited to determine the neutron spectra and calculate the effective cross sections, a comparison with the group fluxes obtained through the MCNP simulations is also presented.

In general a good agreement is found between the experimental data evaluated with the Bayesian analysis and the Monte Carlo results, as you can see in Fig. 3.13. It will be noted that there are a few cases with discrepancies[8]

[8] The discrepancies between the multi-group Bayesian analysis and the Monte Carlo simulations are probably due to systematic errors in the MCNP reactor model or in the experimental data (activation rate measurements and/or cross sections data).

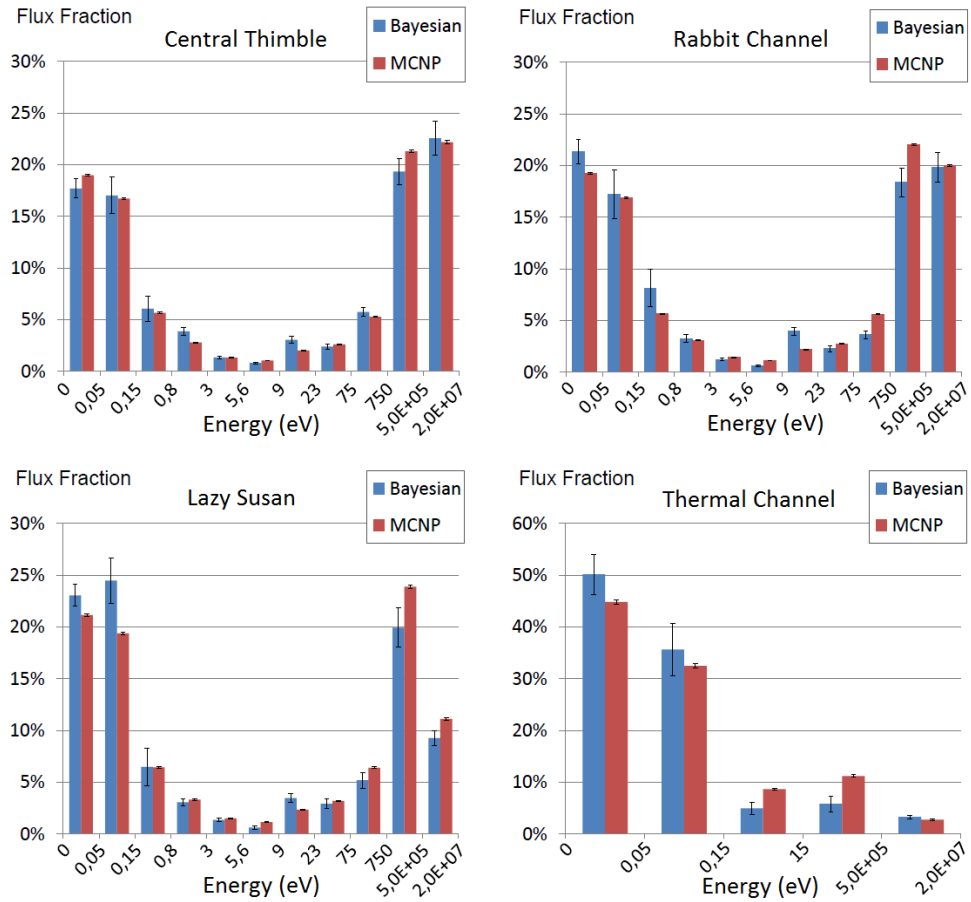

Fig. 3.13: Comparison between the flux fractions evaluated through the Bayesian and Monte Carlo spectrum analysis concerning Central Thimble and Rabbit Channel (top), Lazy Susan and Thermal Channel (bottom).

which significantly exceed the statistical errors (for example the 6^{th}, the 7^{th} and the 9^{th} group of the Rabbit Channel spectrum). This is a direct confirmation that the Bayesian analysis results have a negligible dependence on the MCNP distribution used to calculate the group effective cross sections, because they are not forced to come out equal to those from Monte Carlo simulations.

For this reason, given the general good agreement between the experimental and simulation results, I can conclude that the MCNP model is a reliable tool for determining the neutron spectrum.

Finally, the multi-group flux results were joined to those obtained through the fast neutrons analysis to draw rough spectrum distributions, that were compared with the ones by MCNP simulations. In Fig. 3.14 the case of Central Thimble is shown by way of example (for the comparison keep into account that the axis scales are logarithmic). Similar plots with 13 histogram bins were obtained for Rabbit Channel and Lazy Susan, while for Thermal Channel it was possible to draw a distribution with 7 groups only.

The good agreement that was found in the distribution shapes shows the potential of this analysis, which allows the evaluation of the energy group fluxes and their uncertainties with great accuracy and flexibility, having a negligible dependence on the MCNP spectra that are used to calculate the

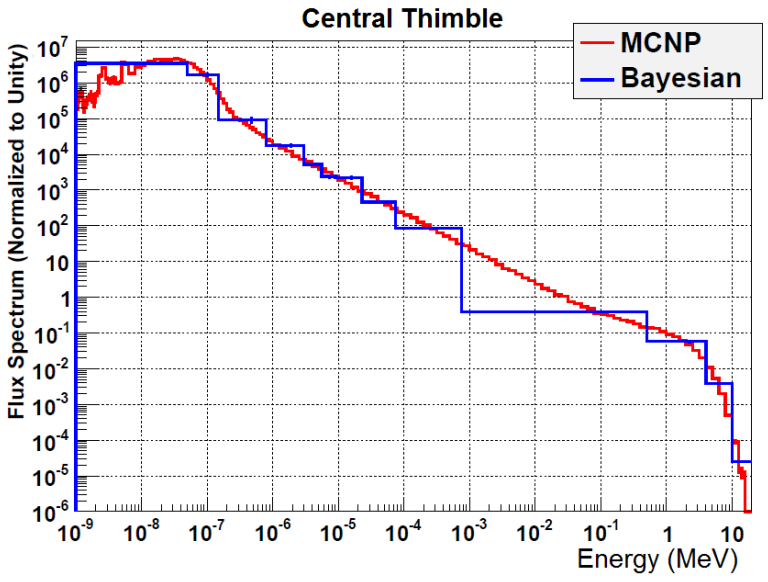

Fig. 3.14: Comparison between the Bayesian multi-group and the MCNP simulation analysis of the Central Thimble spectrum.

group effective cross sections.

The advantage of this methodology is that Bayesian MCMC simulation codes are easy to use and allow to solve complex multi-variables problems with a rigorous statistical approach that combines all the experimental data keeping into account their uncertainties and the variables' correlations.

Energy	Flux		Flux Fraction (%)	
Limits (eV)	$[n/(cm^2 s)]$	ϵ_r%	Bayesian	MCNP
1) $0 \rightarrow 0.05$	$(2.98 \pm 0.16)10^{12}$	5.2	(17.7 ± 0.9)%	(18.99 ± 0.11)%
2) $0.05 \rightarrow 0.15$	$(2.87 \pm 0.30)10^{12}$	10	(17.0 ± 1.8)%	(16.73 ± 0.11)%
3) $0.15 \rightarrow 0.8$	$(1.02 \pm 0.20)10^{12}$	20	(6.1 ± 1.2)%	(5.67 ± 0.06)%
4) $0.8 \rightarrow 3$	$(6.53 \pm 0.62)10^{11}$	9.5	(3.9 ± 0.4)%	(2.80 ± 0.05)%
5) $3 \rightarrow 5.6$	$(2.27 \pm 0.21)10^{11}$	9.1	(1.35 ± 0.12)%	(1.34 ± 0.03)%
6) $5.6 \rightarrow 9$	$(1.37 \pm 0.16)10^{11}$	12	(0.81 ± 0.10)%	(1.05 ± 0.03)%
7) $9 \rightarrow 23$	$(5.17 \pm 0.54)10^{11}$	10	(3.1 ± 0.3)%	(2.03 ± 0.04)%
8) $23 \rightarrow 75$	$(4.05 \pm 0.43)10^{11}$	11	(2.4 ± 0.3)%	(2.61 ± 0.04)%
9) $75 \rightarrow 750$	$(9.69 \pm 0.76)10^{11}$	7.8	(5.8 ± 0.5)%	(5.30 ± 0.06)%
10) $750 \rightarrow 0.5M$	$(3.26 \pm 0.22)10^{12}$	6.7	(19.3 ± 1.3)%	(21.30 ± 0.13)%
11) $0.5M \rightarrow 20M$	$(3.80 \pm 0.28)10^{12}$	7.4	(22.6 ± 1.7)%	(22.19 ± 0.13)%
Φ_{tot}	$(1.68 \pm 0.04)10^{13}$	2.1		

Tab. 3.13: Central Thimble multi-group analysis results.

Energy	Flux		Flux Fraction (%)	
Limits (eV)	$[n/(cm^2 s)]$	ϵ_r%	Bayesian	MCNP
1) $0 \rightarrow 0.05$	$(1.48 \pm 0.08)10^{12}$	5.5	(21.3 ± 1.2)%	(19.26 ± 0.08)%
2) $0.05 \rightarrow 0.15$	$(1.20 \pm 0.16)10^{12}$	14	(17.2 ± 2.3)%	(16.87 ± 0.08)%
3) $0.15 \rightarrow 0.8$	$(5.67 \pm 1.26)10^{11}$	22	(8.2 ± 1.8)%	(5.67 ± 0.05)%
4) $0.8 \rightarrow 3$	$(2.27 \pm 0.25)10^{11}$	11	(3.3 ± 0.4)%	(3.10 ± 0.03)%
5) $3 \rightarrow 5.6$	$(8.73 \pm 0.92)10^{10}$	11	(1.26 ± 0.13)%	(1.44 ± 0.02)%
6) $5.6 \rightarrow 9$	$(4.30 \pm 0.73)10^{10}$	17	(0.62 ± 0.10)%	(1.12 ± 0.02)%
7) $9 \rightarrow 23$	$(2.76 \pm 0.25)10^{11}$	9.2	(4.0 ± 0.4)%	(2.19 ± 0.03)%
8) $23 \rightarrow 75$	$(1.60 \pm 0.21)10^{11}$	13	(2.3 ± 0.3)%	(2.76 ± 0.03)%
9) $75 \rightarrow 750$	$(2.52 \pm 0.29)10^{11}$	11	(3.6 ± 0.4)%	(5.61 ± 0.05)%
10) $750 \rightarrow 0.5M$	$(1.28 \pm 0.10)10^{12}$	7.5	(18.4 ± 1.4)%	(22.01 ± 0.10)%
11) $0.5M \rightarrow 20M$	$(1.38 \pm 0.10)10^{12}$	7.2	(19.9 ± 1.4)%	(19.98 ± 0.09)%
Φ_{tot}	$(6.95 \pm 0.14)10^{12}$	2.1		

Tab. 3.14: Rabbit Channel multi-group analysis results.

Energy	Flux		Flux Fraction (%)	
Limits (eV)	$[n/(cm^2 s)]$	ϵ_r%	Bayesian	MCNP
1) $0 \rightarrow 0.05$	$(5.17 \pm 0.24)10^{11}$	4.6	(23.1 ± 1.1)%	(21.15 ± 0.14)%
2) $0.05 \rightarrow 0.15$	$(5.50 \pm 0.49)10^{11}$	8.9	(24.5 ± 2.2)%	(19.38 ± 0.14)%
3) $0.15 \rightarrow 0.8$	$(1.46 \pm 0.41)10^{11}$	28	(6.5 ± 1.8)%	(6.45 ± 0.09)%
4) $0.8 \rightarrow 3$	$(6.90 \pm 0.83)10^{10}$	12	(3.1 ± 0.4)%	(3.33 ± 0.06)%
5) $3 \rightarrow 5.6$	$(3.07 \pm 0.35)10^{10}$	12	(1.37 ± 0.16)%	(1.53 ± 0.04)%
6) $5.6 \rightarrow 9$	$(1.43 \pm 0.34)10^{10}$	24	(0.64 ± 0.15)%	(1.17 ± 0.03)%
7) $9 \rightarrow 23$	$(7.81 \pm 1.02)10^{10}$	13	(3.5 ± 0.5)%	(2.35 ± 0.05)%
8) $23 \rightarrow 75$	$(6.60 \pm 1.05)10^{10}$	16	(2.9 ± 0.5)%	(3.21 ± 0.06)%
9) $75 \rightarrow 750$	$(1.17 \pm 0.17)10^{11}$	14	(5.2 ± 0.8)%	(6.41 ± 0.09)%
10) $750 \rightarrow 0.5M$	$(4.48 \pm 0.42)10^{11}$	9.5	(19.9 ± 1.9)%	(23.90 ± 0.18)%
11) $0.5M \rightarrow 20M$	$(2.08 \pm 0.16)10^{11}$	7.6	(9.3 ± 0.7)%	(11.12 ± 0.12)%
Φ_{tot}	$(2.24 \pm 0.05)10^{12}$	2.1		

Tab. 3.15: Lazy Susan multi-group analysis results.

Energy	Flux		Flux Fraction (%)	
Limits (eV)	$[n/(cm^2 s)]$	ϵ_r%	Bayesian	MCNP
1) $0 \rightarrow 0.05$	$(1.20 \pm 0.09)10^{11}$	7.7	(50.2 ± 3.9)%	(44.8 ± 0.4)%
2) $0.05 \rightarrow 0.15$	$(8.52 \pm 1.22)10^{10}$	14	(35.6 ± 5.1)%	(32.5 ± 0.3)%
3) $0.15 \rightarrow 15$	$(1.19 \pm 0.29)10^{10}$	24	(5.0 ± 1.2)%	(8.7 ± 0.2)%
4) $15 \rightarrow 0.5M$	$(1.40 \pm 0.37)10^{10}$	26	(5.9 ± 1.5)%	(11.2 ± 0.2)%
5) $0.5M \rightarrow 20M$	$(7.95 \pm 0.79)10^{9}$	10	(3.3 ± 0.3)%	(2.79 ± 0.13)%
Φ_{tot}	$(2.39 \pm 0.06)10^{11}$	2.4		

Tab. 3.16: Thermal Channel multi-group analysis results.

3.3 Characterization of the neutron flux distribution in the core

The last step of the neutron flux analysis involved the measurement and the characterization of the spatial distribution in the core. For this purpose, the neutron activation technique was applied, choosing aluminum-cobalt wires (Al 99.9% - Co 0.1%) as samples to be irradiated in different core positions corresponding to the holes of the upper grid (Fig. 2.17).

The fast flux component was evaluated through the analysis of the ∼4 MeV threshold reaction ^{27}Al(n,α)^{24}Na, while the integral flux was determined from the (n,γ) activation of ^{59}Co. In this way, it has been possible to simultaneously measure the fast and the integral fluxes in the same positions, providing the opportunity to perform interesting comparative analyses.

3.3.1 Experimental equipment and measurements

In order to map the neutron flux distribution along the vertical axis, aluminum-cobalt wires (1 mm in diameter and ∼15 mm long) were looped on dedicated supporting rods which can be inserted in the upper grid holes and can host up to 11 samples 5 cm apart from each other. In this way, an overall length of 50 cm is covered, allowing to map the neutron flux in correspondence with the active fuel region and part of the FE axial reflectors (Fig. 3.15).

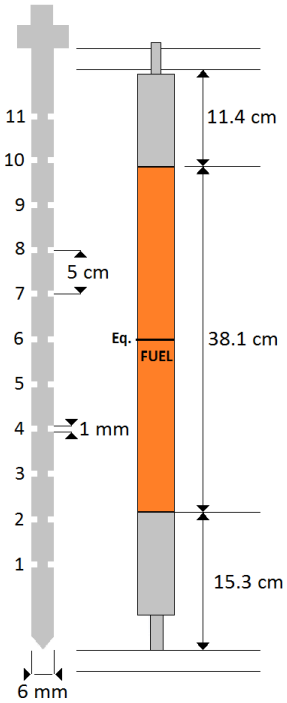

Fig. 3.15

Two identical supporting rods, made of nuclear aluminum, were manufactured so as to perform the irradiations in two holes at the same time.

Due to the relatively short ^{24}Na half-life (14.96 h) and the waiting time required to handle the supporting rods after the irradiation (at least 5 days), we decided not to map more than two holes at a time, otherwise it would have been difficult to measure the sodium activity in all irradiated samples.

For this reason, 6 irradiation campaigns were performed so as to measure the neutron flux in correspondence with 12 upper grid holes (Tab. 3.17). In order to minimize possible systematic effects, the

Irr. #	Date & time	t_{irr} (s)	Holes
1	23/05/13 11:27	3624	12
2	23/05/13 15:58	4859	13
3	29/05/13 15:13	4999	1 & 14
4	21/06/13 12:02	7232	10 & 16
5	26/06/13 15:09	4786	4 & 8
6	02/07/13 11:28	4989	3 & 6
7	09/07/13 11:08	4816	5 & 9

Tab. 3.17: List of the irradiation performed in the different core positions with the corresponding dates and durations.

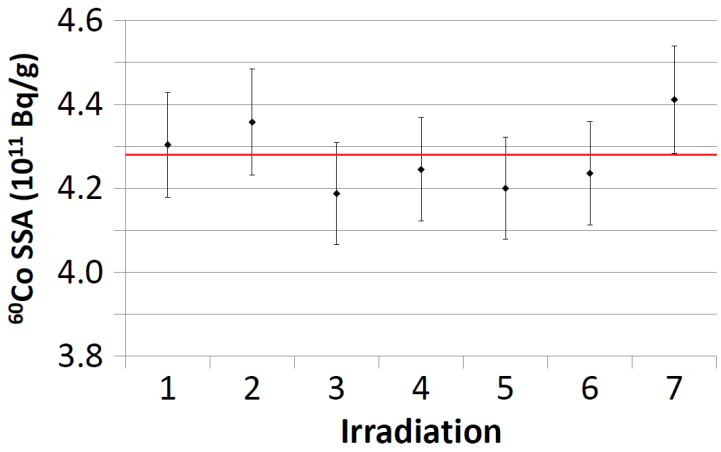

Fig. 3.16: Specific saturation activity of ^{60}Co measured in the monitor samples irradiated in the Lazy Susan facility. The average value is shown through the red line.

control rods were kept in similar positions (with the TRANS and the SHIM completely withdrawn), and the power track was recorded to determine the effective irradiation time at full-power condition (250 kW).

Moreover, in order to check that the flux intensity was equally reproduced in the different irradiations, Al-Co *monitor samples* were positioned in the Lazy Susan facility. In this way, from the analysis of the ^{60}Co activated in the monitor samples (Fig.3.16), we can state that the flux intensity was actually the same within the uncertainty bandwidth. For this reason, to compare the results concerning different irradiations, the data have been normalized to the average monitor's specific saturation activities and their errors have been appropriately estimated including the monitor's uncertainty component.

The activation rates of aluminum and cobalt were evaluated through γ-ray spectroscopy measurements performed with the *GePoz* detector installed at the Radioactivity Laboratory of Milano-Bicocca University.

Thanks to the well configuration of this detector, the geometric efficiency is maximized and the sample placement can be easily reproduced in the different measurements. As described before (see Sec. 3.1.2), the detection efficiency was determined through Monte Carlo simulations based on the GEANT4 code and the uncertainty component due to the efficiency evaluation was fixed to be 5% for each observed γ line.

3.3.2 Fast flux analysis

Firstly, I present the data of the fast flux component[9], whose energy threshold was fixed at 4 MeV, according to the cross section of the ^{27}Al(n,α)^{24}Na reaction (Fig. 3.17).

The effective cross section was evaluated assuming that the fast flux spectrum has an exponential energy dependence: $e^{-\alpha E}$ with $\alpha = 0.65$, as obtained by fitting the MCNP spectrum simulated in the Central Thimble. It is reasonable to assume that this energy dependence does not significantly vary within the core, because it depends primarily on the spectrum of prompt

[9] The experimental data and the fast flux results are reported in appendix: Tab. B.1 and Tab. B.3

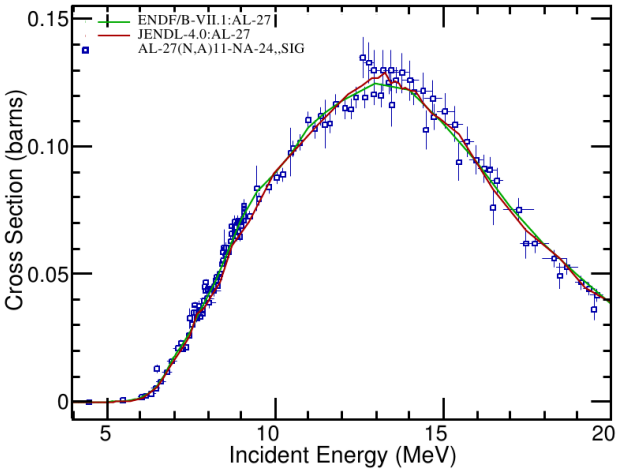

Fig. 3.17: The ENDF/B-VII and JENDL-4.0 cross sections of the ^{27}Al(n,α)^{24}Na reaction, plotted with the experimental data used for their evaluation.

neutrons by fission. For this reason, the same effective cross section value (8.4 mb) can be used for all irradiation positions.

The cross section uncertainty, which can be quantified around 5% (see the experimental data plotted in Fig. 3.17), was treated as a systematic error affecting all measured data in the same way. For this reason, this error component must be considered only when analyzing the absolute value of the fast flux intensity and is not included when presenting comparative analyses of the results obtained in the different irradiation positions.

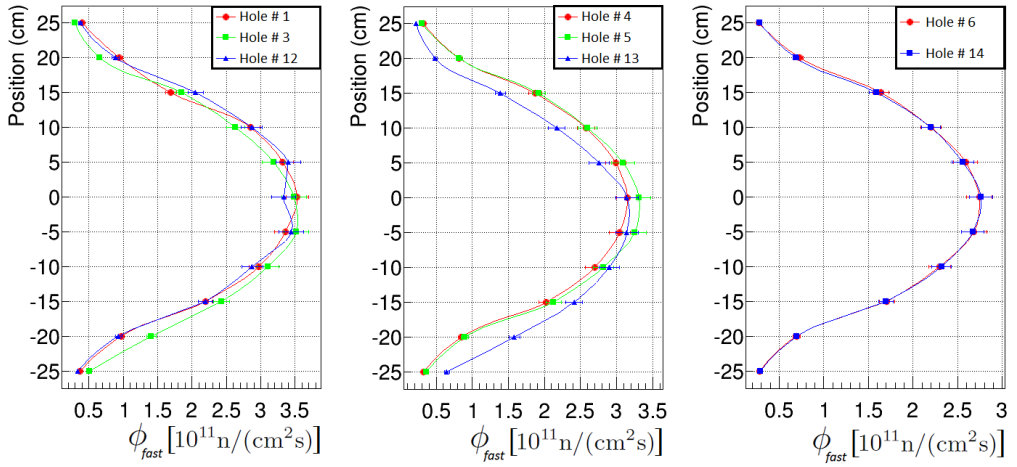

(a) Ring B

(b) Ring C

(c) Ring D

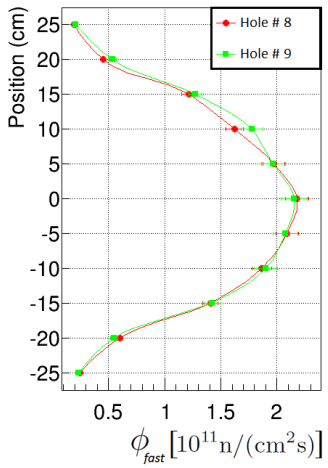

(d) Ring E

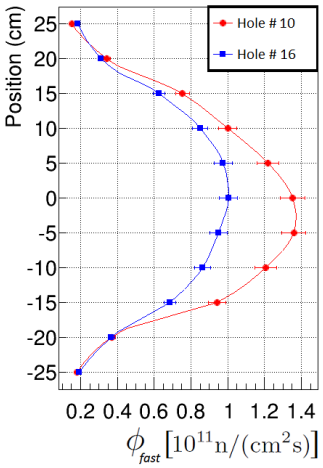

(e) Ring F

Fig. 3.18: Vertical profiles of the fast flux measured in the holes at different distances from the center of the core (rings).

The fast flux vertical profiles obtained for each irradiation position are presented in Fig. 3.18. The data concerning holes which are located at the same distance from the center of the core are drawn on the same graphs to provide the opportunity of an immediate comparison. For convenience, the same labels of the FE rings are used to indicate the hole positions along the radial direction. In the graphs, the red and green colors are used for the holes located in the same side of the core, while the blue points refer to the data acquired in the opposite side (for the scheme of hole positions see Fig. 2.17).

Looking at Fig. 3.18, the fast flux data referring to the peripheral positions are always symmetric respect to the center of the fuel active region (position 0 cm) with two exceptions: the hole #3 in ring B and the hole #13 in ring C. Since these two profiles appear shifted downward respect to the others, we can reasonably assume that the supporting rods were not fully inserted in the core during the irradiations. If this is the case, the experimental data would refer to positions which are few centimeters higher, thus resulting compatible with the other profiles.

In general, it is interesting to note that the fast flux is also symmetric in the radial direction: in fact, comparing the data acquired in the same rings, the profiles are always overlapping except for the outer ring (F). The reason why such large difference was recorded between the data of holes #10 and #16 is not easy to identify and further measurements would be required to investigate this aspect; however, it should be noted that the Rabbit Channel is not far from the hole #16 and its presence could lead to a lower fast flux because a reduced number of fission reactions occur in that core region.

Finally, the measured data show that the fast flux decreases with a relatively high gradient when moving towards the peripheral core regions: in fact, in the vertical profiles, there is a ratio around 1:10 between the data at ± 25 cm and the ones at the center, while in the radial direction a decrease by a factor ~ 2.5 is recorded between the data of ring B and F.

3.3.3 Integral flux analysis

The measurement of the integral flux was performed by analyzing the (n,γ) reaction on ^{59}Co, which is mainly induced by thermal and epithermal neutrons[10]. In this case, it is interesting to firstly analyze the graphs referring to the ^{60}Co activation rate per unit mass (or, equivalently, specific saturation activity, SSA) in the different irradiation positions.

Looking at Fig 3.19, it will be noted that the profiles are not as symmetric

[10] The experimental data and the integral flux results are reported in appendix: Tab. B.2 and Tab. B.4

as those obtained for fast neutrons. Irregular patterns are also observed in the peripheral positions outside the fuel active region (which extends between ±19 cm). In particular, in some holes of rings E and F, the activation rates at ±15 cm resulted lower than those at ±20 cm.

These experimental findings can be explained by considering that the neutron spectrum varies within the core. In particular, the fraction of thermal neutrons over the total flux increases in the peripheral core regions and,

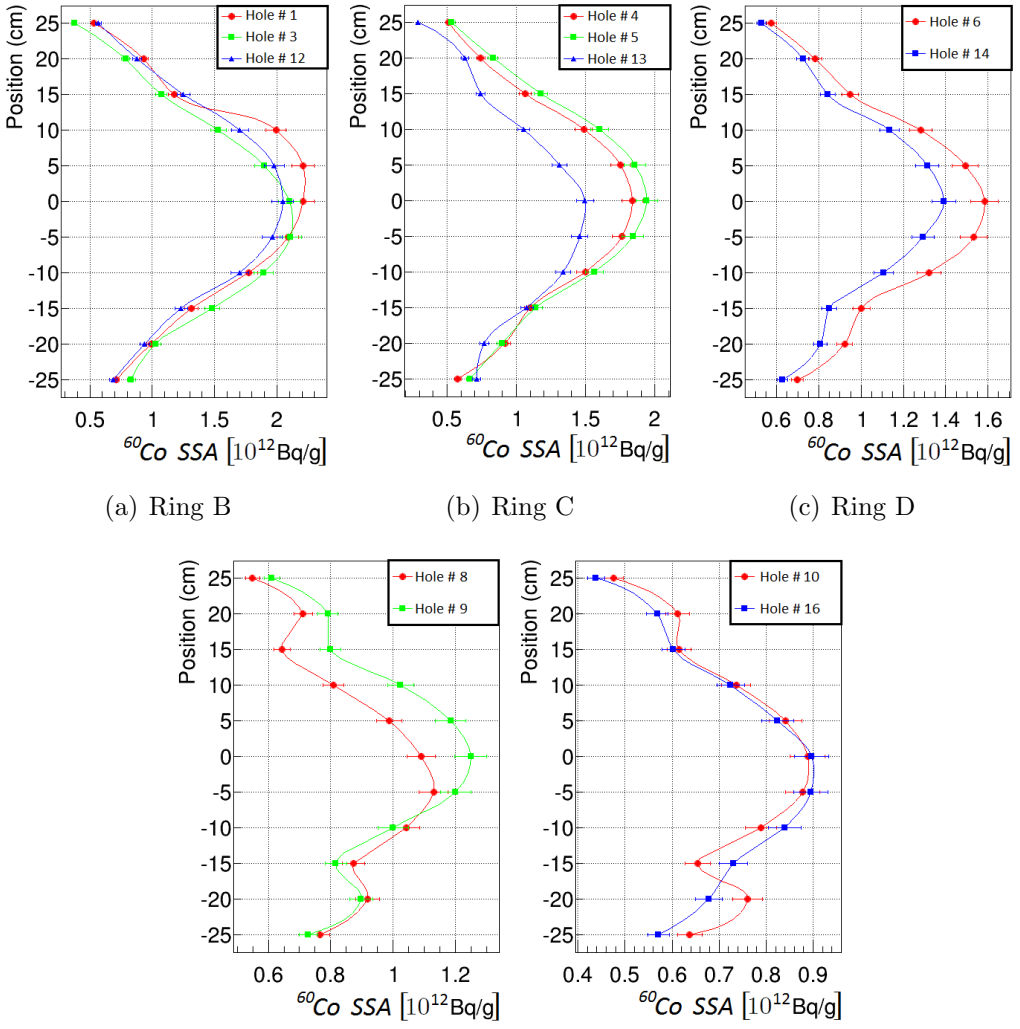

(a) Ring B (b) Ring C (c) Ring D

(d) Ring E (e) Ring F

Fig. 3.19: Vertical profiles of the ^{60}Co SSA measured in the different holes and rings.

as a consequence, the effective cross section is higher.

Therefore, for evaluating the integral flux, it is not possible to use the same σ_{eff} value for all the irradiation positions, otherwise we would obtain incorrect flux profiles characterized by the same irregular patterns observed in the SSA graphs.

For this reason, the MCNP reactor model was exploited to evaluate the neutron spectra and calculate the corresponding effective cross sections in all irradiation positions. The σ_{eff} values obtained for the case of hole #16 are shown in Fig. 3.20, where differences up to a factor 2 are recorded between the central and the peripheral positions.

The integral flux values were then calculated with the effective cross sections evaluated point by point and the results are presented in Fig. 3.21. As expected, the integral fluxes are characterized by decreasing intensities while moving towards the peripheral regions and the irregular patterns are no longer present. With respect to the fast flux, these profiles have a lower gradient: in fact, comparing the data at the ends and at the center of the vertical profiles, we observe a ratio of about 1:3 in the outer rings and 1:5 in the inner ones. Moreover, in the radial direction the flux data in the different rings are nearly constant at ±25 cm and their ratio does not exceed 2.5 at position 0 cm.

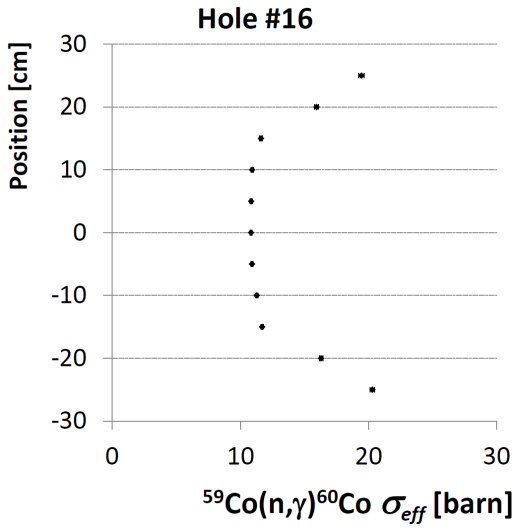

Fig. 3.20: The effective cross section of (n,γ) reaction on ^{59}Co evaluated in the different irradiation positions of hole #16 exploiting the MCNP reactor model for determining the neutron spectra.

The data of the holes #3 and #13 appear again as shifted downward, in line with the observations concerning the corresponding fast flux profiles, thus supporting the hypothesis that in those cases the samples were not correctly positioned in the core.

Analyzing the integral flux profiles referring to holes at the same distance from the center, no significant differences are observed in the case of Ring F, in which the fast fluxes resulted asymmetric in the opposite holes.

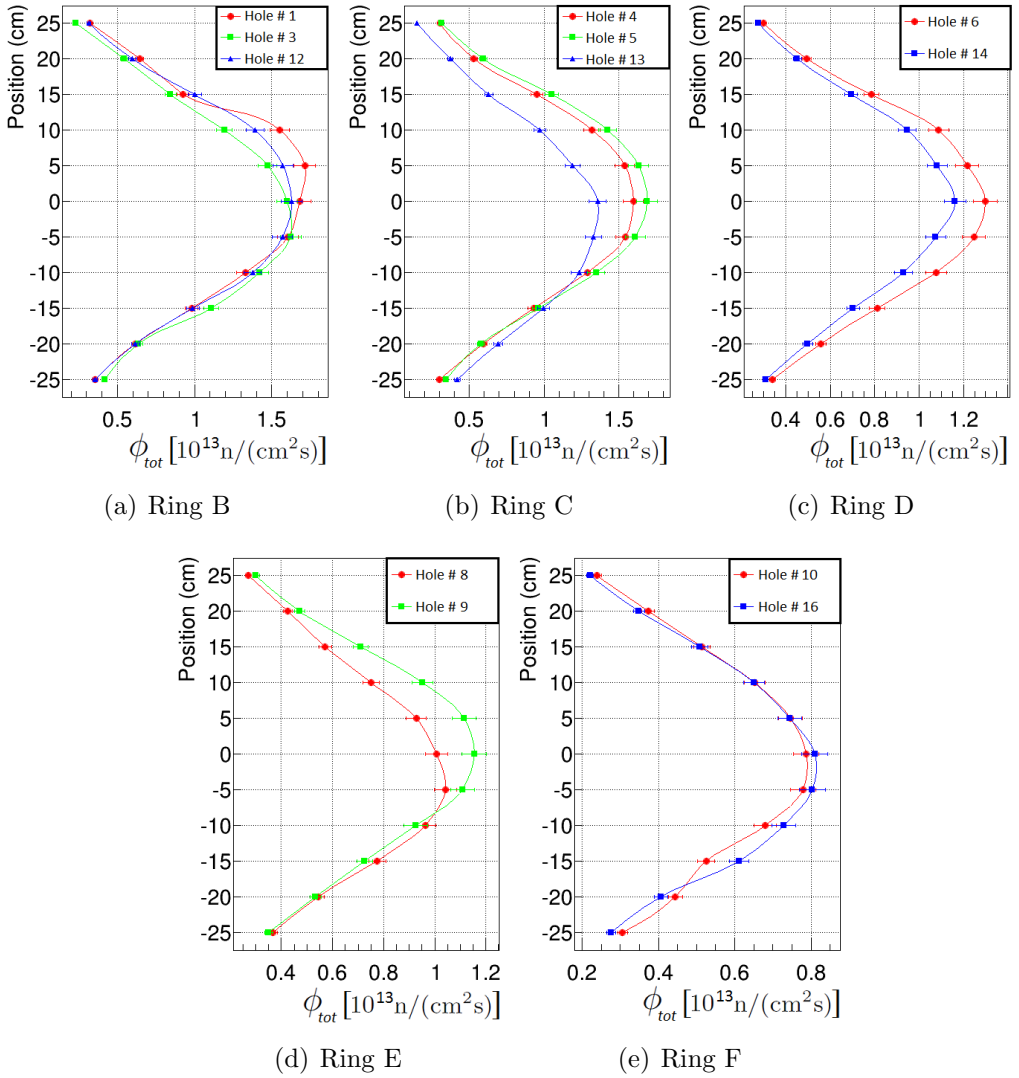

(a) Ring B (b) Ring C (c) Ring D

(d) Ring E (e) Ring F

Fig. 3.21: Vertical profiles of the integral flux measured in the different holes and rings.

The interpretation of these findings is not straightforward and further experimental tests would be needed to check the repeatability of this measurement, in order to exclude possible systematic errors related to the position of the supporting rod in the holes of ring F.

On the contrary, some differences are recorded in the rings C, D and E. In particular, it is interesting to note that the corresponding fast flux profiles are completely overlapped, meaning that these asymmetries regard the thermal and epithermal neutron flux component only.

These experimental observations can be explained by considering the peculiar geometry of an experimental reactor such as the TRIGA Mar II, equipped with a graphite reflector which is not totally symmetric, because it hosts the Lazy Susan facility and the penetrating and tangential irradiation channels (see Sec. 2.1.3). Since the reflector acts mainly on thermal neutrons, this would account the fact that these differences are observed in the integral flux profiles only.

Moreover, the different fuel burnup can locally influence the distribution of the thermal neutrons, which are particularly susceptible to be captured by the poisons that have accumulated over time in the fuel elements.

In conclusion, the results of this analysis show that the fast flux component is always characterized by a symmetric distribution, reflecting the symmetry of the fuel elements disposition. For this reason, the fast flux profiles are also suitable to identify possible systematic errors in the positioning of samples.

On the other hand, in the evaluation of the integral flux, it is important to underline the role of the MCNP simulations: in fact, their utilization has proved to be fundamental for a correct interpretation of the activation data, taking into account the effects related to the thermalization of the neutron spectrum in the peripheral core regions.

In the next chapter, after developing a new MCNP model in which the fuel burnup will be calculated and simulated, these experimental data will be used as a benchmark for validating the new model. In particular, the capability of correctly simulating not only the neutron spectra (as previously shown through the Bayesian analysis), but also the neutron flux absolute intensity will be tested.

Chapter 4

Fuel burnup analysis and core reconfiguration

The fuel burnup analysis is an essential component in the development of a simulation model for a nuclear reactor, because the fuel consumption and the buildup of neutron poisons significantly affect the system reactivity. Moreover, this analysis is important to evaluate the fuel cycle and determine the amount of long-lived radioactive waste which are produced in a reactor after a certain operating time.

In order to adapt the MCNP model for simulating the current configuration of the TRIGA Mark II reactor, a time evolution software was developed to calculate the burnup of each fuel element. The historical data of reactor operating time and core configurations were combined with the information about neutron fluxes, derived from MCNP simulations, to reproduce the material aging through about 48 years.

This software was developed completely in-house to take into account some features that differentiate experimental reactors from those used in power plants, such as the daily ON/OFF cycle and the long fuel lifetime; in fact, these effects are not negligible to properly account for neutron poisons accumulation.

In the next sections, I present first the fuel burnup simulation and then an analysis for validating the MCNP reactor model updated to September 2013 configuration. Finally, I will show how the reactor simulation model was applied to identify and realize a new *optimized* core configuration. The implemented procedures were adopted to increase the system reactivity and reduce, at the same time, the number of fuel elements inserted in the core. In this way, the fuel is exploited with higher efficiency and the reactor can continue to run for a longer time without the need for new fuel elements.

4.1 Fuel burnup simulation

The simulation model for the fuel burnup is based on the solution of a coupled set of production-destruction equations, describing the concentrations of the various fuel isotopes in an operating reactor [5]. The isotopes produced by fission tend to be neutron-rich and undergo radioactive decay. They also undergo neutron capture, with cross sections ranging from a few tenths of a barn to millions of barns. The general equation satisfied by the concentration ($n_j(t)$) of a fission product species j (characterized by λ^j decay constant and σ_a^j absorption cross section) is:

$$\frac{dn_j}{dt} = \gamma_j \, \Sigma_f \, \phi + \sum_i (\lambda^{i \to j} + \sigma^{i \to j} \, \phi) \, n_i - (\lambda^j + \sigma_a^j \, \phi) \, n_j \tag{4.1}$$

where γ_j is the fission yield of isotope j, Σ_f is the macroscopic fission cross section of the fuel, ϕ is the integral flux intensity, $\lambda^{i \to j}$ is the decay rate of isotope i to produce isotope j and $\sigma^{i \to j}$ is the transmutation cross section for the production of isotope j by neutron capture in isotope i. In this equation the cross sections must be intended as being the effective ones, to take into account the reaction rate dependence on the neutron flux spectrum.

The time evolution of the elements belonging to the original fuel composition (U, Zr and H) or produced through neutron capture (e.g. the transuranium isotopes) is described by an equation similar to Eq. 4.1, with the only difference that the production term containing γ_j is zero.

The above equations can be integrated to determine composition changes over the lifetime of a fuel element if the time dependence of the flux is known. However, the flux distribution depends on the fuel composition. In order to overcome this issue, a depletion-time step (Δt_{burn}) is defined in which the neutron flux distribution is assumed to negligibly vary over time. In this way, the above equations can be integrated to determine a new fuel composition to be used in the subsequent time step.

The maximum value of Δt_{burn} depends on how fast the composition is changing and on the effect of that composition change on the neutron flux distribution. For the TRIGA Mark II reactor, we found that the time scale of significant flux changes is greater than the maximum operation time elapsed between two reconfigurations of the core (∼3500 hours)[1]. For this reason, the 48 years of operation were subdivided in 27 time steps, one for each core reconfiguration that occurred from 1965 to 2013 (Tab. 4.1).

[1] For the moment, the relatively short time scale phenomena associated with the ^{135}Xe fission product are excluded.

Therefore, at each step of the burnup simulation, the following procedure was applied:

1. an MCNP simulation with the full power reactor model is run to determine the neutron flux distribution in the fuel elements;
2. the effective cross sections of the simulated isotopes are calculated starting from the MCNP neutron flux spectra and the ENDF/B-VII data libraries;
3. the data about neutron fluxes, fission yields, effective cross sections, radioactive decays and reactor operation time (normalized to 250 kW power) are combined to calculate the new isotopic composition of the fuel elements;
4. a new MCNP simulation input file is prepared, positioning the fuel elements and the control rods according to the next configuration.

The poison accumulation and the fuel evolution were calculated applying some approximations, which were essential to shorten the computational time and simplify the problem solution.

- Each fuel element was subdivided in 5 axial sections, which evolved separately to account for the uneven distribution of the neutron flux[2].

[2] The number of sections in which dividing the fuel elements was chosen after some tests: particularly, since relatively small differences were observed respect to simulations in which 3 sections were defined for each FE, we could consider the 5 axial sections as a good approximation.

Date	Hours	Date	Hours	Date	Hours
16-11-1965	652	17-01-1973	870	13-01-1989	1150
28-04-1967	182	09-10-1973	3039	07-01-1991	164
27-06-1967	907	21-10-1976	111	25-03-1991	2149
17-04-1968	351	27-12-1976	2685	23-10-1995	810
02-09-1968	632	07-01-1980	2488	12-06-1997	2270
03-01-1969	1166	15-03-1983	507	19-10-2001	422
18-08-1969	1500	14-02-1984	582	21-01-2003	678
04-09-1970	2196	29-01-1985	584	22-09-2005	436
11-01-1972	1586	11-11-1985	3556	31-12-2006	1952

Tab. 4.1: Beginning date of each core configuration and operation time in the following step (the last step is until 25-09-2013).

Fission Products						Trans-uranium
^{83}Kr	^{102}Ru	^{131}Xe	^{145}Nd	^{152}Sm		^{236}U
^{95}Nb	^{103}Rh	^{133}Cs	^{147}Pm	^{153}Sm		^{239}Pu
^{95}Mo	^{105}Rh	^{135}Cs	^{147}Sm	^{153}Eu		^{240}Pu
^{97}Mo	^{105}Pd	^{139}La	^{149}Sm	^{155}Eu		^{241}Pu
^{99}Tc	^{113}Cd	^{141}Pr	^{150}Sm	^{155}Gd		^{241}Am
^{101}Ru	^{129}I	^{143}Nd	^{151}Sm	^{157}Gd		

Tab. 4.2: List of the fission products and trans-uranium isotopes included in the burnup calculation.

- A restricted set of fission products and trans-uranium elements was simulated: in fact, we selected only the isotopes reaching concentrations and having absorption/fission cross sections which are not negligible for a correct evaluation of the reactor k_{eff} and of the neutron fluxes (see Tab. 4.2).

- The ^{135}Xe fission product was not evolved as the other isotopes, because it is characterized by large daily variations: its average concentration in the fuel elements was simulated considering a typical week in which the reactor operates 6 hours a day from Monday to Friday.

- Each time step was divided into sub-intervals, in which the ON/OFF condition of the reactor is alternated to properly simulate the time evolution of the radioactive isotopes; particularly, since it was impossible to reconstruct the real ON/OFF cycles, we took 6 hour sub-intervals for the ON condition and we calculated the duration of the OFF sub-steps so that the sum of all ON/OFF cycles was equal to the real time elapsed between the reconfiguration dates.

- In each sub-interval, the production and destruction terms appearing in Eq. 4.1, were assumed to be constant, thus decoupling the evolution equations of the different isotopes.

We checked that all the applied approximations did not significantly affect the burnup calculation. Particularly, we verified that the exact solutions of the coupled set of production-destruction equations are equivalent to those obtained by using decoupled equations, in which the isotopic composition and the production-destruction constants are updated at each sub-interval. Indicating with P_j and D_j the production and the destruction constants of

isotope j, respectively, Eq. 4.1 can be written as:

$$\frac{dn_j(t)}{dt} = P_j - D_j\, n_j(t) \tag{4.2}$$

whose solution is the same for all isotopes:

$$n_j(t) = \frac{P_j}{D_j}\left(1 - e^{-D_j t}\right) + n_j(0)\, e^{-D_j t} \quad (D_j \neq 0) \tag{4.3}$$

When the flux is set to zero for simulating the OFF condition, the D_j coefficient are equal to zero for stable isotopes; in this case, the solution of Eq. 4.2 becomes:

$$n_j(t) = P_j\, t + n_j(0) \tag{4.4}$$

In this way, we implemented a flexible code which can manage the evolution of all isotopes of interest by calculating the P_j and D_j coefficients for each sub-step; if necessary, it is possible to shorten the sub-intervals duration to simulate the evolution of radioisotopes with relatively short half-life. Moreover, the fission products from ^{239}Pu were included in the calculation and the evolution of the burnable poison disks was simulated as well.

In order to analyze the burnup calculation results, we plotted the concentrations of the different isotopes in each fuel section as a function of the reactor operating time. As an example, we report some of these plots in Fig. 4.1, referring to a fuel element which was positioned in slot D1 from 1965 to 2001 and in slot E17 until 2013. The time evolution of the atomic concentrations in the different fuel sections (numbered from 1 to 5 starting from the bottom) can be compared and the integral neutron flux in the central fuel section is also represented to provide information about its change in the different core configurations.

I chose to report in Fig. 4.1 a set of representative isotopes characterized by different time evolutions:

- the fissile isotopes ^{235}U and ^{239}Pu, which show decreasing and increasing trends, respectively, because the first one is burned, while ^{239}Pu is progressively produced by capture reactions on ^{238}U;
- the ^{133}Cs and ^{143}Nd fission products, which do not reach saturation and exhibit a linear trend as a function of the reactor operating time;
- the ^{113}Cd and ^{149}Sm fission products, reaching the saturation condition in which the production rate is equal to the destruction rate by neutron capture;

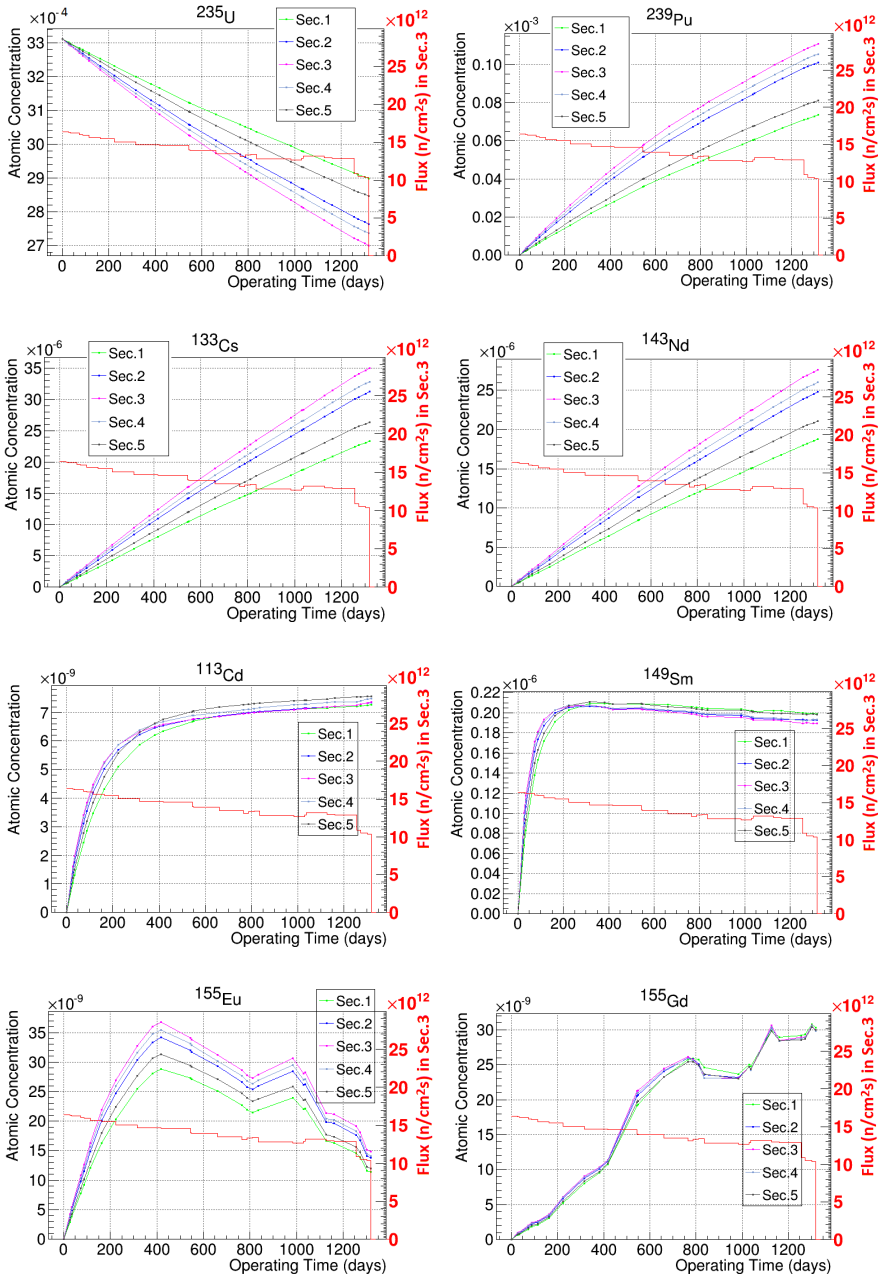

Fig. 4.1: Time evolution of the atomic concentrations of different isotopes in the 5 sections of the FE number 3426. The integral neutron flux in the central section is also represented with the red color. The horizontal axis represents the net operating time of the reactor at full power condition.

- the ^{155}Eu and ^{155}Gd isotopes, whose evolution is correlated because ^{155}Gd is produced by the decay of ^{155}Eu fission product:

$$^{155}Eu \rightarrow ^{155} Gd + e^{-} + \overline{\nu}_e \qquad (\tau_{1/2} = 4.75\, y).$$

In the last case, it must be considered that ^{155}Eu and ^{155}Gd concentrations depend not only on the reactor operation time (represented on the horizontal axis) but also on the OFF time, during which the ^{155}Eu decay continues to occur. Since the ON/OFF time ratio varied over the years, the ^{155}Eu production term can not be considered constant and, as a consequence, its concentration does not reach a stable saturation value, though the neutron flux intensity is practically constant. It is interesting to note the correlation between ^{155}Eu and ^{155}Gd: as ^{155}Eu decreases (for example in the 400-800 days range), the ^{155}Gd concentration grows faster.

Thanks to the flexibility of our evolution software, this peculiar feature, characterizing the isotope time evolution in experimental reactors, was properly simulated.

Analyzing the concentrations in the 5 fuel sections, it is observed that ^{235}U is burned at different rates, depending the neutron flux intensity along the vertical axis, as expected. For the same reason, there is higher accumulation of not-saturated fission products and trans-uranium elements in the central fuel section. However, it is interesting to note that the concentration of the isotopes reaching saturation does not significantly vary in the different fuel sections. In fact, in those cases, the saturation level is equal to the ratio between the production/destruction constants, which is independent of the neutron flux intensity:

$$\frac{P_j}{D_j} = \frac{\gamma_j \, \Sigma_f \, \phi}{\sigma_a^j \, \phi} = \frac{\gamma_j \, \Sigma_f}{\sigma_a^j} \tag{4.5}$$

Therefore the slight differences observed for the saturated isotope concentrations in different fuel sections are correlated to the value of Σ_f, which depends on the atomic density of fissile isotopes.

It is important to point out that non-saturated isotopes represent a fundamental component of neutron poisons, though they are characterized by lower absorption cross sections than those saturated. In fact, the impact of a poison on the neutron balance is determined by the absorption rate:

$$R_a = n_j \, \sigma_a^j \, \phi \tag{4.6}$$

In the case of a saturated isotope, since the atomic concentration n_j is inversely proportional to σ_a^j (Eq. 4.5), R_a does not depend on the absorption

cross section:

$$R_a = \gamma_j \, \Sigma_f \, \phi \tag{4.7}$$

On the other hand, the concentrations of non-saturated isotopes linearly increase over time, reaching values which can be several orders of magnitude greater than those of saturated isotopes.

Moreover, it is important to underline that in both cases the absorption rate is proportional to the fission yield γ_j.

Therefore, a non-saturated isotope may cause more absorption reactions than a saturated poison with higher cross section, but lower fission yield. This is the case, for example, of ^{133}Cs and ^{113}Cd, having effective absorption cross sections of about 15 b and 7550 b, respectively, and fission yields equal to 6.7% and 0.014%, respectively. Looking at Fig. 4.1, it is shown that the ^{133}Cs concentration grows up to 3.5×10^{-5} in the central section of FE number 3426, while ^{113}Cd concentration saturates at $\sim 7.2 \times 10^{-9}$. In this condition, the absorption rate due to ^{133}Cs is about 10 times greater then that due to ^{113}Cd.

In order to check the MCNP model answer to the fuel composition changes, we analyzed the effective multiplication factors (k_{eff}), evaluated through the Monte Carlo simulations at the beginning of each time step. The control rods were positioned according to the available historical data concerning the first full power criticality after each reconfiguration.

The k_{eff} results are shown in Fig. 4.2: all of them are within a range of

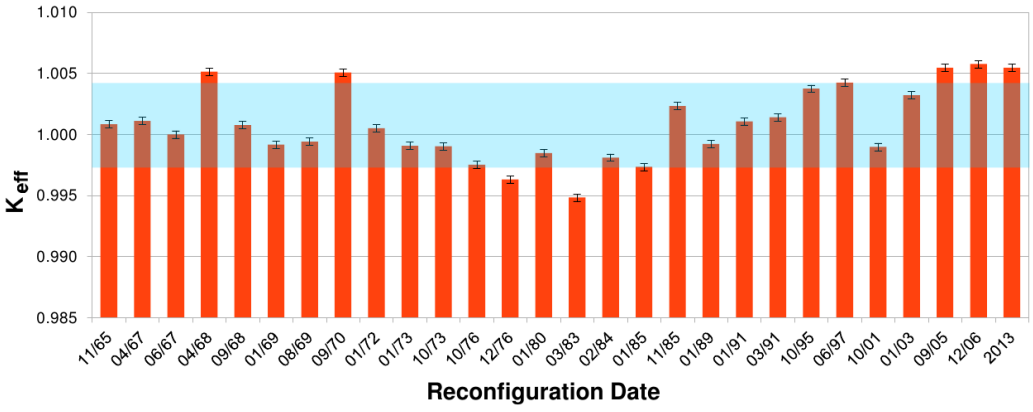

Fig. 4.2: The k_{eff} results evaluated through the Monte Carlo simulations at the beginning of each time step. The shadowed area corresponds to the $\pm 1\sigma$ range from the average value, σ being the standard deviation of the results.

about ± 0.005 centered on the expected value $k_{eff} = 1$. In terms of reactivity, this range corresponds to about ± 0.7 \$. By calculating the average value and the standard deviation of the results, we obtain 1.00067 ± 0.00291, which is an outcome in good agreement with the expected value of 1.

Taking into account that the burnup calculation was performed over a period covering 48 years, this analysis confirms that the fuel aging was simulated with good accuracy. In fact, we do not observe any specific trend connected to an incorrect evaluation of the fuel burnup; there are instead some random fluctuations, due to systematic errors which may affect the evaluation of a very sensitive parameter like k_{eff}. Particularly, it should be considered that there is some lack of information in the historical data, especially regarding the Transient rod position, which is known only approximately for some criticality configurations; moreover, the exact position of the Central Thimble (which can be moved along the vertical axis) is not known for all the configurations.

Finally, in order to quantify the burnup level in each fuel element, a *burnup index* is defined as follows:

$$B.I.(t) = \frac{1}{n^{235}(0)} \left[n^{235}(0) - \left(n^{235}(t) + n^{239}(t) \frac{\sigma_f^{239}}{\sigma_f^{235}} \right) \right] \tag{4.8}$$

where $n^{235}(t)$ and $n^{239}(t)$ are the average concentrations of the fissile isotopes ^{235}U and ^{239}Pu, respectively. With such a definition, the burnup index quantifies not only the ^{235}U consumption, but also the ^{239}Pu production, whose concentration is weighted by the ratio $\sigma_f^{239}/\sigma_f^{235}$, to account for the different probability characterizing the fission of these isotopes.

The burnup indexes referring to September 9 2013, are listed in Tab. 4.3: in this table, all the 97 fuel elements used in the 48 years reactor operation are included. Their burnup index essentially depends on the amount of usage time and on the positions occupied in the core: some fuel elements were used in all configurations, while some others were subsequently added or replaced to guarantee the reactor criticality over years.

In order to visualize the different core configurations, I produced diagrams in which the FE burnup indexes are represented with a color scale. Some of them are shown in Fig. 4.3: the fuel elements represented around the core correspond to those that were used for core refueling or were substituted over time. It is interesting to note that the refueling operations generally regarded the central FEs, which are burned faster compared to the others. Moreover, in the recent configurations, FEs with stainless steel cladding (represented with a black contour) were used in the inner core rings, because this mate-

rial is more resistant to high temperatures compared to aluminum. The last diagram represents the core as it was configured in September 9 2013, after 1405.1 days of full power operation.

FE #	B.I.(%)	FE #	B.I.(%)	FE #	B.I.(%)	FE #	B.I.(%)
2346	6.2	3553	9.2	3668	9.7	7898	8.2
2347	8.9	3576	9.1	3669	8.7	7899	6.0
3068	9.5	3577	10.1	3670	12.0	7900	8.7
3426	11.0	3578	10.9	3757	9.8	7901	6.0
3455	10.4	3579	9.7	3759	10.3	7902	8.5
3528	10.0	3580	9.7	3760	9.5	7903	4.7
3529	9.5	3581	8.8	3762	9.0	7904	6.4
3530	9.5	3582	9.3	3763	8.4	7905	6.5
3531	12.1	3584	11.2	3764	6.7	9680	5.6
3532	10.0	3651	10.5	3765	1.4	10002	5.4
3533	3.3	3652	11.3	3766	9.6	10003	3.8
3534	2.0	3653	6.2	3767	9.0	10004	3.7
3537	7.1	3654	1.0	4976	10.2	10085	2.2
3538	9.4	3655	10.2	4977	9.8	10662	3.7
3539	9.0	3656	9.8	4978	13.2	10663	2.8
3540	6.5	3657	8.9	4979	14.0	10896	1.4
3541	5.9	3658	10.2	4980	14.3	10897	1.4
3542	8.1	3659	10.2	4981	13.5	10898	1.5
3544	2.2	3660	9.0	4982	12.5	10899	1.1
3545	6.8	3661	10.3	4983	11.0	10900	1.3
3546	8.8	3662	10.2	4984	10.3	10901	1.2
3547	9.5	3663	10.1	4985	13.7	10902	0.8
3549	9.1	3664	10.8	5194	7.2		
3550	2.9	3665	11.2	7876	6.4		
3551	7.5	3666	9.9	7897	8.4		

Tab. 4.3: Burnup index of the fuel elements referring to September 9, 2013.

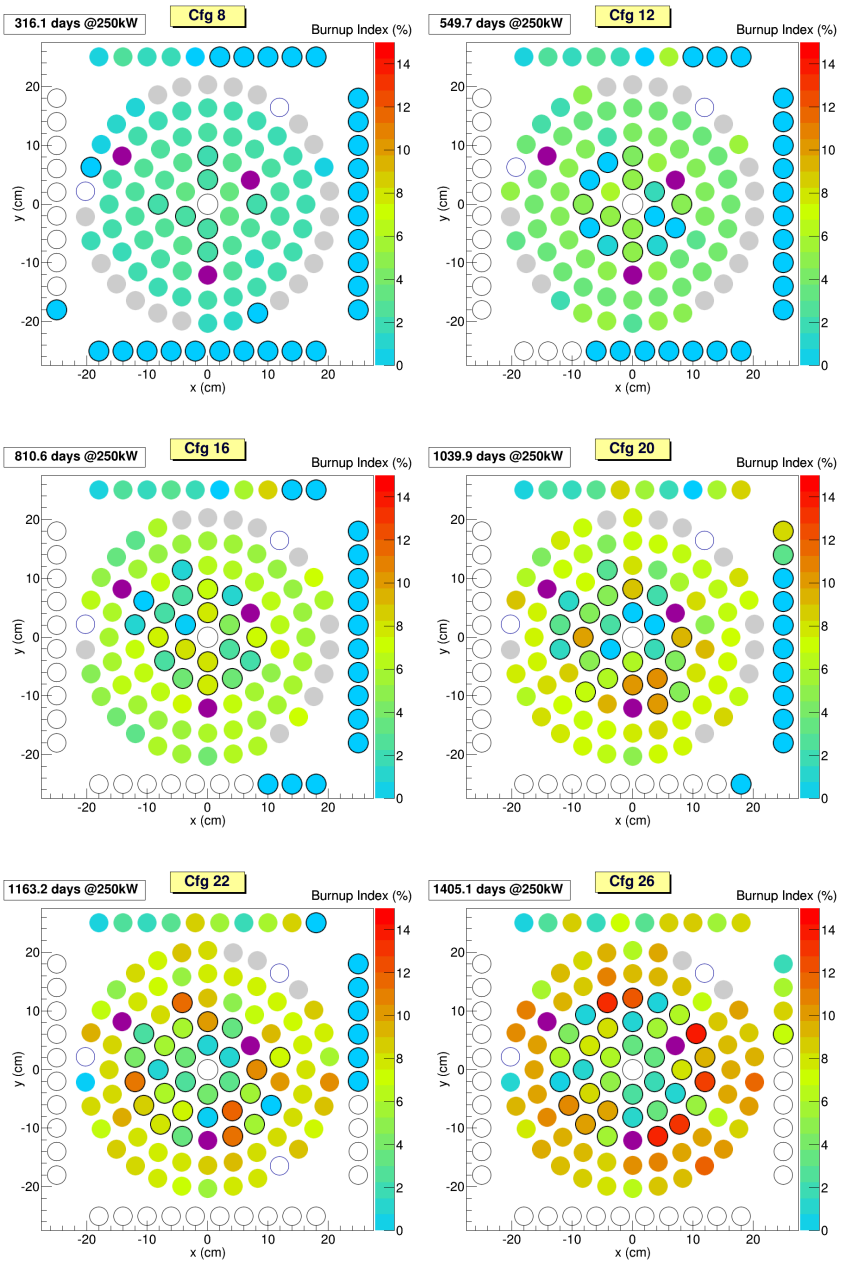

Fig. 4.3: Diagrams of six core configurations: the counter in the top right shows the full-power reactor operating time from 1965. The color scale indicates the burnup index of each fuel element; purple is used for the control rods, grey for the dummy elements and white for the irradiation facilities and the neutron source. The circles forming a square around the core represent the FEs which are not used for that configuration. Black contours are used to identify the FEs with stainless steel cladding.

4.2 Benchmark analysis of the updated MCNP reactor model

The MCNP simulation model referring to September 9, 2013 reactor configuration, obtained at the end of the burnup calculation, was then benchmarked using the available experimental data referring to neutron fluxes, Regulating rod calibration and system criticality.

Monte Carlo simulations were performed with the updated MCNP model to evaluate the integral neutron flux[3] in the positions corresponding to the holes where the Al-Co samples were irradiated (see Sec. 3.3 and the core scheme in Fig. 2.17). The experimental data were then compared with the simulation results, normalized to 250 kW power, in order to check the MCNP capability to correctly reproduce the absolute fluxes. Since a systematic positioning error of about 3 cm was observed for the data referring to hole number 13, the neutron flux tallies for this hole were translated into the corresponding positions for a better comparison.

The benchmark analysis results are presented in Fig. 4.4: in general, a good agreement is observed between the experimental and Monte Carlo data in all irradiation positions. The largest differences are observed in holes number 8 and 14: in the first case, a small positioning error seems to affect the results, while some mismatch is recorded in the central positions of hole #14. Anyway, in both data sets, the maximum difference between each couple of data is around 20%, that, in the first instance, may be considered an acceptable error. Concerning the other positions, a very good agreement is obtained for the holes number 6 and 12, whose data all agree within 8%, which corresponds to $\sim 2\sigma$ range, taking into account that the experimental uncertainties are equal to about 4%. In the other data sets, differences up to 3σ are recorded for some data referring to peripheral positions, while a better agreement characterize the data corresponding to the active fuel length in the range ± 15 *cm*.

This benchmark analysis highlights that the updated MCNP reactor model is able to reproduce the absolute scale of the neutron flux core distribution with good accuracy. This is an important result, confirming the reliability of the fuel burnup analysis, which strictly depends on the neutron fluxes evaluated through the Monte Carlo simulations.

As further benchmark for the new MCNP model of the TRIGA reactor, we simulated the Regulating control rod calibration curve. This rod was chosen because all calibration measurements are performed with the Transient

[3] The simulation results are reported in appendix: Tab. B.5

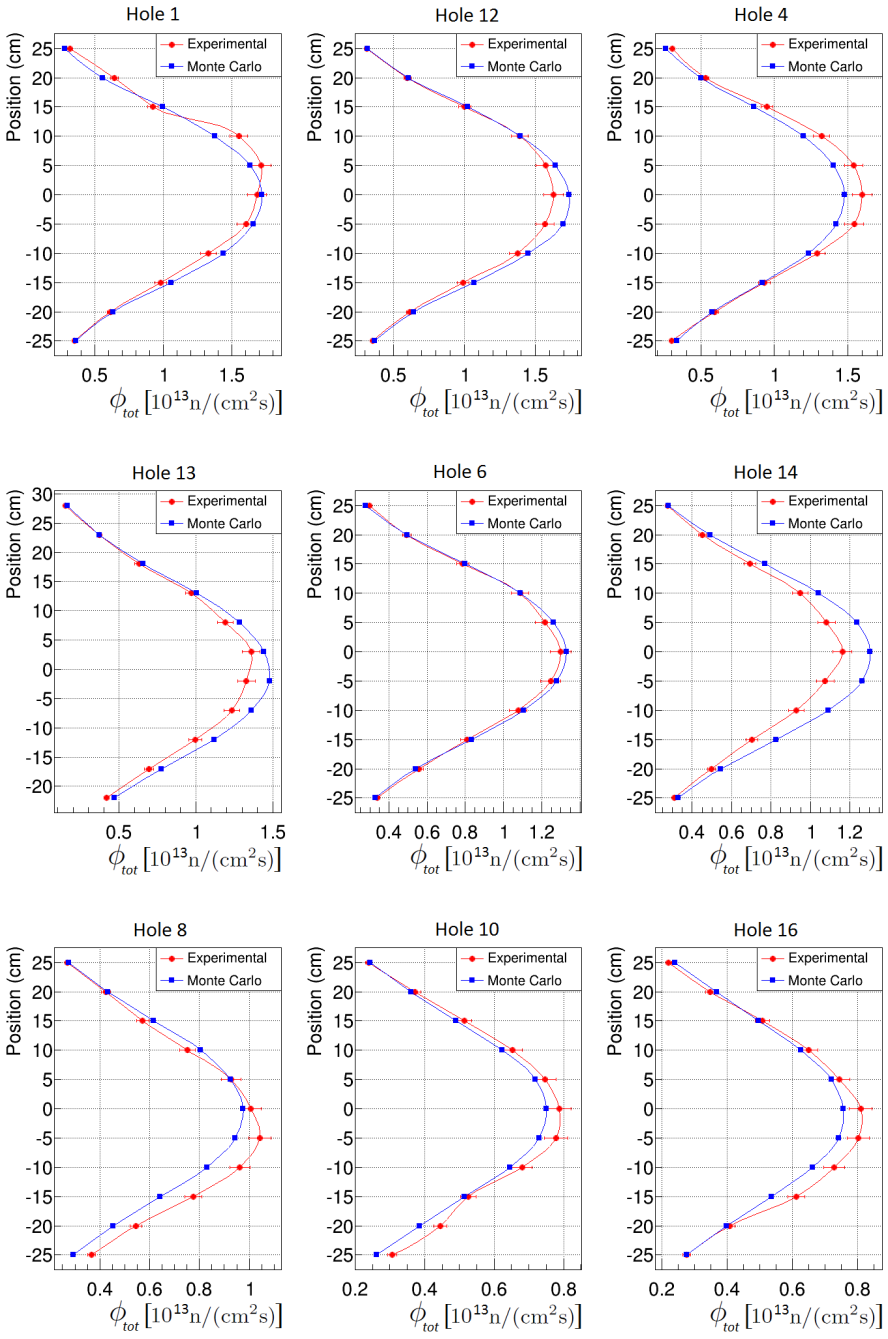

Fig. 4.4: Comparison between the experimental and the simulated vertical distributions of the integral neutron flux.

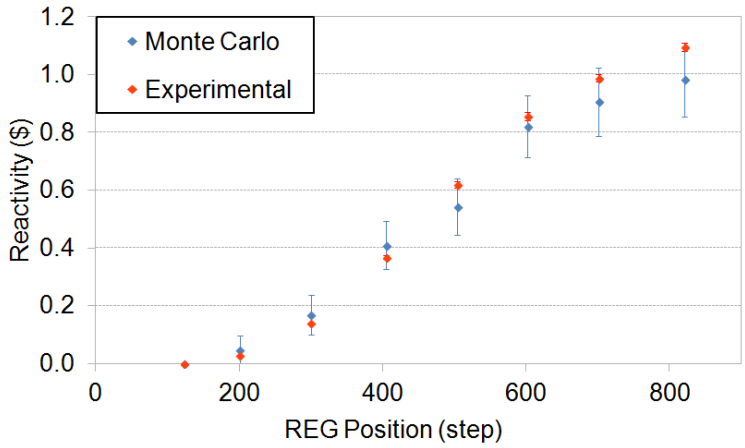

Fig. 4.5: Comparison between experimental and Monte Carlo calibration curve of the Regulating control rod, referring to September 9, 2013 configuration.

rod completely withdrawn: in this way, the possible systematic errors related to the approximate description of the Transient rod are excluded.

The simulation results presented in Fig. 4.5 show a very good agreement with the experimental calibration curve, demonstrating the reliability of the new simulation model in evaluating the reactivity variations induced by moving the Shim and Regulating control rods.

Finally, we checked the model capability to evaluate the system reactivity in the low power condition, in which the fuel can be simulated to be in thermal equilibrium with water at room temperature. In this way, the thermal effects do not affect the evaluation of the k_{eff} parameter. A simulation was performed with the control rods in the positions recorded during a low power (1.5 W) criticality measurement dated September 9, 2013:

- Shim: 430 digits;
- Regulating: 610 digits;
- Transient: 1000 digits (completely withdrawn).

The reactivity resulted equal to (0.16±0.02)$. Although this value is significantly different from the experimental critical condition (0 $), we have to take into account that the uncertainty includes the Monte Carlo statistical component only and that the absolute value of reactivity is a very sensitive parameter of the reactor model. In fact, as previously shown, the systematic uncertainties related to the modeling of the reactor geometry, materials

and neutron cross sections, induce reactivity changes of the order of a few tenths of \$. For this reason, considering that the fuel aging calculation was performed over 48 years and that the evaluation of the full power reactor operating time is also affected by some uncertainty, we can state to have achieved a very good result.

4.3 A new core configuration for the TRIGA Mark II reactor

The updated simulation model of the TRIGA reactor, whose reliability was demonstrated through the benchmark analysis, was then exploited to identify a new *optimized* core configuration, with the aim of increasing the system reactivity.

An important parameter to be considered for this kind of analysis is the *core excess* (CE), defined as the reactivity value which would be obtained in a hypothetical configuration with all the control rods completely withdrawn. Since this configuration is not experimentally feasible, this parameter is determined from the control rods calibration curves. Considering, for example, the low power reactor criticality dated September 9, 2013 (in which the Transient control rod was completely withdrawn), the CE can be determined from the calibration curves of Shim and Regulating rods, which were positioned at step 430 and 610, respectively. The sum of the reactivity ranges between the full withdrawn and the criticality positions (highlighted in Fig. 4.6 through the red arrows) corresponds to the core excess, which resulted equal to (2.06±0.03)\$.

This value is relatively small, because the core excess must be sufficient to counterbalance the reactivity losses due to thermal effects and ^{135}Xe poisoning, otherwise it is not possible to reach the 250 kW power steady state.

In September 9 2013, the CE evaluated at full power condition was (0.43±0.03)\$ only: this condition did not allow to power up the reactor in the morning, if it was operating the afternoon before. As a consequence, it was necessary to wait until ^{135}Xe decayed enough to allow the full power reactor operation.

A core reconfiguration was needed to increase the reactor CE. For this purpose, we exploited the MCNP simulation model, with the fuel burnup updated to September 9, 2013: new configurations, ensuring a higher CE and possibly requiring the use of less fuel elements, were simulated and analyzed.

In defining the new possible configurations, some technical prescriptions must be respected:

- the CE must not exceed the half-sum of the three *control rod worths*[4], which is about ∼3 $);
- the sum of the Transient and Regulating control rod worths must exceed the CE by at least 0.5 $;
- the fuel elements instrumented with thermocouples must not be moved from their positions: B3, B6 and D7;
- the rings B and C must be filled using FEs with stainless steel cladding, which is more resistant than aluminum to the high fuel temperature in the inner core region;
- some of the FE listed in Tab. 4.3 are not usable, because in the past their cladding was damaged[5] and they were removed from the core.

The basic idea we used to find an optimized configuration is to concentrate the FEs with lower burnup index in the inner core region, where the "fresh" fuel is better exploited thanks to the higher fluxes. Moreover, since the aluminum cladding has a lower absorption cross section respect to stainless steel, we decided to fill the rings D and E with 101-type FEs.

[4] The control rod worth is the reactivity excursion obtained by moving a rod from the full inserted to the full withdrawn position.

[5] The numbers of the damaged FEs are: 2346, 2347, 3533, 3534, 3544, 3550, 3654 and 5194. Their cladding was probably fissured by the high temperature excursions occurring when the reactor was operated in pulse mode, reaching a 250 MW power peak. Moreover, the FE number 3539 is not usable because its bottom endcap pin has been accidentally skewed.

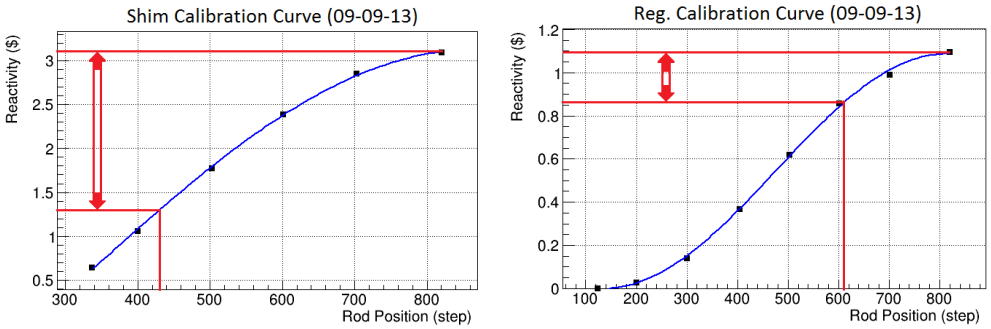

Fig. 4.6: Calibration curves of Shim and Regulating control rods, with the indication of the reactivity ranges used for evaluating the core excess of the configuration dated September 9, 2013.

Therefore, after fixing the positions of the instrumented FEs, we identified the "fresher" fuel elements with steel cladding to be placed in rings B and C. After that, the 101-type FEs were sorted in ascending order according to their burnup index and were disposed in the core starting from ring D to ring F. The remaining empty slots in ring F were filled with FEs having steel cladding. Finally, the arrangement of fuel elements belonging to the same ring was chosen such to obtain a configuration as symmetric as possible.

The first simulation tests were run to determine the minimum number of fuel elements needed to increase the CE by at least 0.5 \$ with respect to the configuration of September 9 2013, in which 83 FEs were used. The Monte Carlo simulations predicted that 79 FEs are sufficient to realize a configuration with a CE ∼0.55 \$ higher than the previous one. Moreover, it was evaluated that the reactivity gain would be ∼0.25 \$ lower using 78 FEs and ∼0.15 \$ higher using 80 FEs.

Moreover, we checked that the choice of the FEs arrangement within a ring does not significantly affect the system reactivity. Some simulations were performed by randomly exchanging the FEs belonging to the same rings, finding comparable values for the k_{eff} results.

Therefore, the proposed configuration with 79 FEs can be considered as

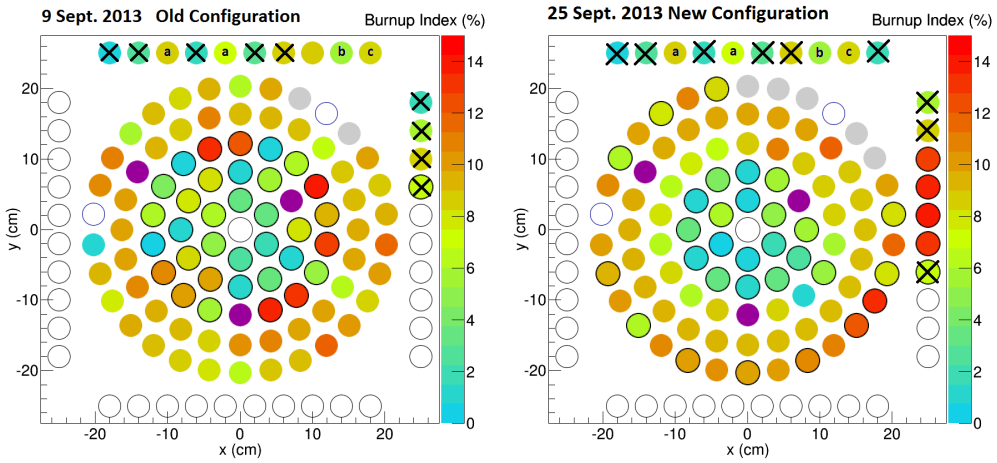

Fig. 4.7: Comparison between the old configuration and the new core configuration. The fuel elements barred with X correspond to the damaged FE removed from the reactor pool; the FEs labeled with "a" are elongated more than 5 mm, the "b" FE is the one not entering in the upper grid and the "c" FE is the one that is impossible to hook.

Rod Worths ($)		
Control Rod	Before	After
SHIM	3.09	2.87
REG	1.08	1.06
TRANS	1.95	2.03

Tab. 4.4: The control rod worths before and after the core reconfiguration. The uncertainties, evaluated from the control rods calibration procedure, are quantified around 1%.

the optimal one and we decided to experimentally realize it.

The handling operations for the core reconfiguration started after September 9, 2013. In this phase, the fuel elements were inspected one by one, finding that four of them were not usable for the new core configuration. Particularly, the FEs number 3551 and 3762 are elongated more than 5 mm, the 3541 FE can not enter in the upper grid, while it is impossible to hook the 3581 FE.

For this reason, we simulated a new configuration, excluding these four elements from the core. In order to achieve a comparable reactivity gain, equal to (0.57± 0.05)$, 80 FE had to be used. The core excess predicted for this new configuration is (2.63 ± 0.05)$, where the uncertainty corresponds to the Monte Carlo statistical error.

The *old* and the *new* core configurations are compared in Fig. 4.7 and reported in appendix (Tab. C.1), where it is possible to see that the FEs with higher burnup were removed from the core, while the elements with "fresher" fuel were concentrated in the inner rings.

After the core reconfiguration was completed (September 25, 2013) the control rods were calibrated through the stable period method. In this way, it is possible to determine the new core excess value and check that the technical prescriptions concerning the control rod worths are respected.

The new calibration curves are presented in Fig. 4.8 and the control rod worths are reported in Tab. 4.4, where the new values are compared to the previous ones.

The new experimental core excess resulted equal to (2.49±0.03)$, which is a value compatible within 2σ of the CE predicted by Monte Carlo simulations: (2.63 ± 0.05)$. Moreover, the control rod worths technical prescriptions are all respected and the reactor can be safely operated.

Finally, the criticality configurations, recorded during the calibration of the Regulating rod, were simulated to check the evaluation of k_{eff} in the low power condition. The simulation results are presented in Fig. 4.9; their mean

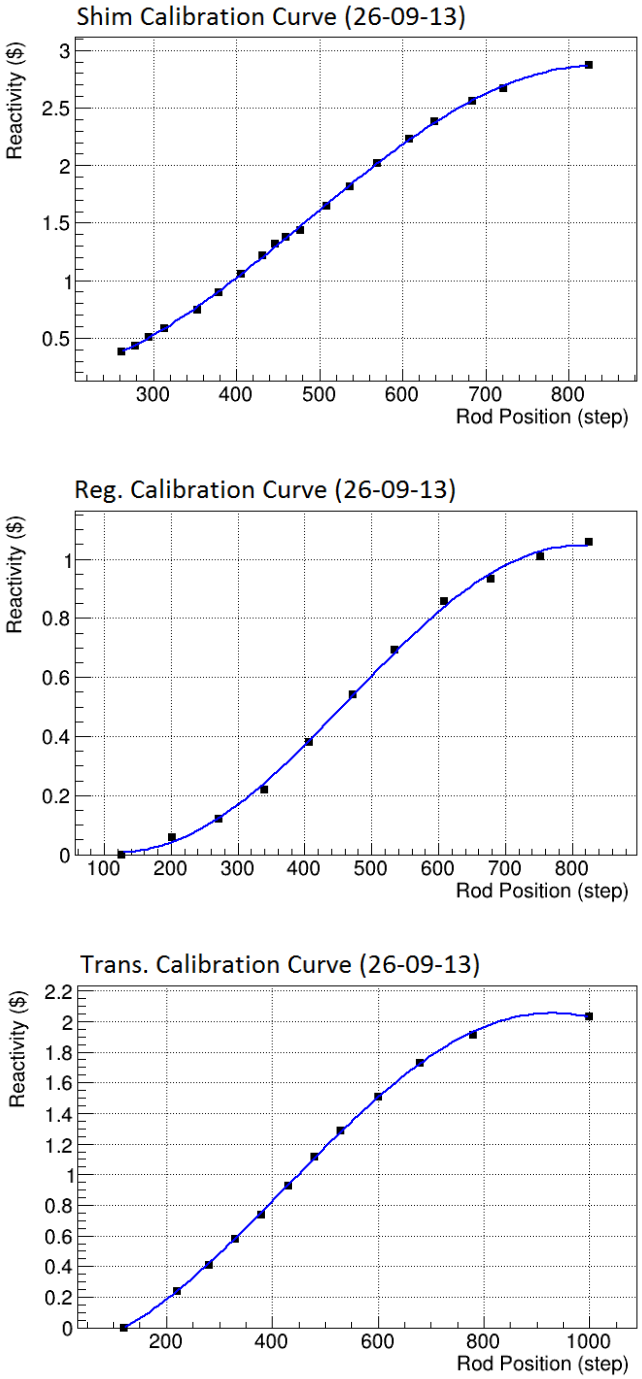

Fig. 4.8: The new calibration curves of the control rods, dated September 26, 2013.

and standard deviation are equal to (0.27±0.06)$. It is worth noting that these results are characterized by an offset, with respect to 0 $, which is compatible with that affecting the reactivity evaluation in the previous core configuration, which was equal to (0.16±0.02)$.

These findings prove that the MCNP simulation model developed for the TRIGA Mark II reactor is a reliable tool for predicting the system reactivity and the core excess after a complete reconfiguration. This is a very important achievement, since the Monte Carlo simulation model was crucial for identifying the new core configuration, which will allow to exploit the TRIGA fuel with higher efficiency.

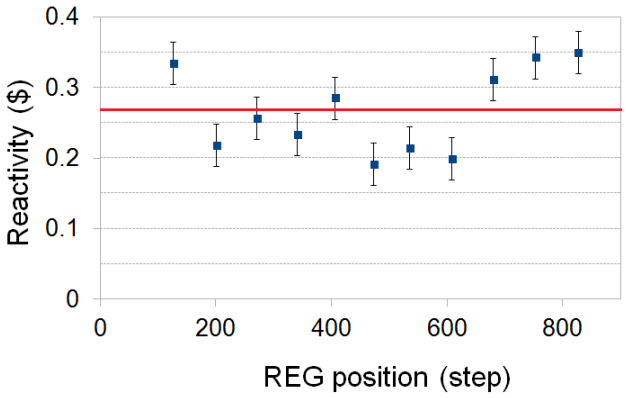

Positions (digit)		ρ ($)
REG	SHIM	[±0.03]
126	477	0.33
201	460	0.22
271	447	0.26
340	432	0.23
406	406	0.29
472	379	0.19
534	353	0.21
608	313	0.20
679	295	0.31
752	278	0.34
826	262	0.35

Fig. 4.9: Results of the simulations with the control rods in the positions corresponding to the criticality configurations recorded during the calibration of Regulating rod (the Transient rod was completely withdrawn).

Conclusions

A complete model for the Triga Mark II reactor at the University of Pavia was developed using the Monte Carlo code MCNP and was validated through experimental benchmarks.

This tool for the neutronic analysis of the reactor has proved to be reliable in simulating different operating conditions and core configurations.

Particular care was devoted to describe the reactor geometries and materials, analyzing the main systematic components which can affect the model. After introducing all the information and the data that were collected from the original documents provided by General Atomics (the reactor constructor), it was possible to correctly simulate the first criticality configuration, dated back to 1965. In this respect, it was shown that the joint use of the MCNP model and a thermal-hydraulic calculation tool allowed to evaluate the temperature distribution of the fuel-moderator in the full power reactor steady state, characterizing the thermal effects which significantly influence the system reactivity.

Thereafter, in order to evaluate the fuel burnup over the years and update the simulation model to the current configuration, a thorough analysis of the neutron fluxes was carried out, because the knowledge of their intensities, energy spectra and spatial distributions is fundamental for determining all the reaction rates.

The neutron activation of different isotopes was used for accurately measuring the neutron fluxes and a Bayesian statistical methodology, original in this research field, was conceived to analyze the different neutron spectra which characterize some irradiation positions within the reactor. The good agreement between the measured and the simulated neutron spectra proves that the experimental data analysis is robust and that the MCNP reactor model provides a good description of the neutron spectra.

This feature of the simulation tool has revealed to be fundamental in the

analysis of neutron-induced reactions, because modeling the neutron spectrum in the different core positions allows to accurately estimate the effective cross sections and, as a consequence, the reaction rates.

The MCNP simulation model of the reactor was thus exploited to evaluate the fuel burnup and the accumulation of neutron poisons and trans-uranium isotopes. In fact, the evolution equations were solved by combining the information about neutron fluxes (derived from MCNP simulations) with the historical data of reactor operating time and the nuclear data of neutron cross sections and fission yields.

The updated reactor model, obtained after simulating the material aging through about 48 years, was benchmarked using the experimental data of reactivity and neutron fluxes, finding a good agreement in the results. This achievement, along with the success of the core reconfiguration, shows that the MCNP model of the TRIGA Mark II reactor is a powerful tool, able to evaluate complex parameters such as the fuel burnup.

The results of this Ph.D. thesis highlight that it is possible to implement analysis tools −ranging from Monte Carlo simulations to the fuel burnup time evolution software, from neutron activation measurements to the Bayesian statistical analysis of flux spectra, and from temperature measurements to thermal-hydraulic models−, which can be appropriately exploited to describe and comprehend the complex mechanisms ruling the operation of a nuclear reactor. Particularly, it was demonstrated the effectiveness and the reliability of these tools in the case of an experimental reactor, where it was possible to collect many precious data to perform benchmark analyses.

Therefore, for as these tools have been developed and implemented, they can be used to analyze other reactors and, possibly, to project and develop new generation systems, which will allow to decrease the production of high-level nuclear waste and to exploit the nuclear fuel with improved efficiency.

Appendix A

Experimental data and results of integral neutron flux measurement

Appendix A. Experimental data and results of integral neutron flux measurement

SPECIFIC SATURATION ACTIVITY (Bq/g)				
Isotope	Central Thimble	Rabbit Channel	Lazy Susan	Thermal Channel
		STD2		
^{46}Sc	$(2.01 \pm 0.08)10^{12}$	$(8.97 \pm 0.35)10^{11}$	$(3.39 \pm 0.15)10^{11}$	$(6.86 \pm 0.59)10^{10}$
^{140}La	$(2.30 \pm 0.03)10^{11}$	$(1.06 \pm 0.02)10^{11}$	$(3.98 \pm 0.27)10^{10}$	$(7.53 \pm 0.53)10^{9}$
^{153}Sm	$(2.37 \pm 0.09)10^{12}$	$(1.03 \pm 0.05)10^{12}$	$(3.66 \pm 0.28)10^{11}$	$(4.68 \pm 0.58)10^{10}$
^{152m}Eu	$(3.24 \pm 0.14)10^{13}$	$(1.44 \pm 0.08)10^{13}$	$(5.40 \pm 0.05)10^{12}$	$(1.03 \pm 0.12)10^{12}$
^{152}Eu	$(6.01 \pm 0.20)10^{13}$	$(2.80 \pm 0.25)10^{13}$	$(1.08 \pm 0.07)10^{13}$	$(2.08 \pm 0.17)10^{12}$
^{154}Eu	$(4.60 \pm 0.12)10^{12}$	$(2.12 \pm 0.14)10^{12}$	$(7.57 \pm 0.23)10^{11}$	$(1.40 \pm 0.41)10^{11}$
^{160}Tb	$(1.11 \pm 0.05)10^{12}$	$(4.85 \pm 0.33)10^{11}$	$(1.68 \pm 0.15)10^{11}$	$(2.01 \pm 0.19)10^{10}$
^{166}Ho	$(2.29 \pm 0.07)10^{12}$	$(1.04 \pm 0.04)10^{12}$	$(3.79 \pm 0.36)10^{11}$	$(5.10 \pm 0.84)10^{10}$
^{177}Lu	$(2.28 \pm 0.15)10^{12}$	$(9.46 \pm 0.56)10^{11}$	$(3.65 \pm 0.29)10^{11}$	$(6.38 \pm 0.59)10^{10}$
^{233}Pa	$(2.07 \pm 0.10)10^{11}$	$(8.81 \pm 0.54)10^{10}$	$(3.38 \pm 0.17)10^{10}$	$(4.76 \pm 0.94)10^{9}$
		STD3		
^{51}Cr	$(5.02 \pm 0.36)10^{10}$	$(2.60 \pm 0.13)10^{10}$	$(7.48 \pm 0.60)10^{9}$	$(1.63 \pm 0.27)10^{9}$
^{60}Co	$(2.68 \pm 0.18)10^{12}$	$(1.11 \pm 0.11)10^{12}$	$(3.88 \pm 0.31)10^{11}$	$(7.39 \pm 0.75)10^{10}$
^{72}Ga	$(1.29 \pm 0.04)10^{11}$	$(5.19 \pm 0.13)10^{10}$	$(2.10 \pm 0.06)10^{10}$	$(3.15 \pm 0.33)10^{9}$
^{76}As	$(3.66 \pm 0.10)10^{11}$	$(1.48 \pm 0.06)10^{11}$	$(5.70 \pm 0.35)10^{10}$	$(6.78 \pm 0.92)10^{9}$
^{75}Se	$(3.35 \pm 0.22)10^{10}$	$(1.43 \pm 0.10)10^{10}$	$(5.52 \pm 0.52)10^{9}$	$(8.2 \pm 1.5)10^{8}$
^{110m}Ag	$(1.25 \pm 0.06)10^{11}$	$(5.12 \pm 0.11)10^{10}$	$(1.90 \pm 0.04)10^{10}$	$(2.35 \pm 0.12)10^{9}$
^{115}Cd	$(1.14 \pm 0.04)10^{10}$	$(3.96 \pm 0.26)10^{9}$	$(1.64 \pm 0.25)10^{9}$	$(1.23 \pm 0.20)10^{8}$
^{114m}In	$(3.04 \pm 0.14)10^{10}$	$(1.23 \pm 0.06)10^{10}$	$(4.69 \pm 0.19)10^{9}$	
^{134}Cs	$(1.40 \pm 0.04)10^{12}$	$(6.05 \pm 0.25)10^{11}$	$(2.40 \pm 0.26)10^{11}$	$(2.86 \pm 0.30)10^{10}$
^{239}Np	$(2.73 \pm 0.12)10^{11}$	$(1.11 \pm 0.05)10^{11}$	$(4.05 \pm 0.28)10^{10}$	$(2.46 \pm 0.23)10^{9}$
		STD4		
^{103}Ru	$(1.49 \pm 0.05)10^{10}$	$(8.19 \pm 0.38)10^{9}$	$(2.79 \pm 0.10)10^{9}$	$(4.35 \pm 0.45)10^{8}$
^{122}Sb	$(3.16 \pm 0.08)10^{11}$	$(1.53 \pm 0.05)10^{11}$	$(4.83 \pm 0.17)10^{10}$	$(4.24 \pm 0.32)10^{9}$
^{124}Sb	$(1.42 \pm 0.05)10^{11}$	$(6.68 \pm 0.33)10^{10}$	$(2.12 \pm 0.19)10^{10}$	$(1.87 \pm 0.20)10^{9}$
^{175}Hf	$(1.70 \pm 0.07)10^{10}$	$(8.26 \pm 0.47)10^{9}$	$(3.22 \pm 0.14)10^{9}$	
^{181}Hf	$(1.09 \pm 0.11)10^{11}$	$(5.59 \pm 0.64)10^{10}$	$(1.73 \pm 0.16)10^{10}$	$(3.7 \pm 1.3)10^{9}$
^{192}Ir	$(7.19 \pm 0.23)10^{12}$	$(3.62 \pm 0.16)10^{12}$	$(1.25 \pm 0.05)10^{12}$	$(2.19 \pm 0.15)10^{11}$
^{194}Ir	$(2.22 \pm 0.07)10^{12}$	$(1.08 \pm 0.03)10^{12}$	$(3.65 \pm 0.11)10^{11}$	$(4.83 \pm 0.30)10^{10}$
^{198}Au	$(3.46 \pm 0.18)10^{12}$	$(1.64 \pm 0.09)10^{12}$	$(5.63 \pm 0.26)10^{11}$	$(6.57 \pm 0.49)10^{10}$
		SOLID SAMPLES		
^{59}Fe	$(2.26 \pm 0.10)10^{8}$	$(9.39 \pm 0.38)10^{7}$	$(3.83 \pm 0.11)10^{7}$	$(7.75 \pm 0.52)10^{6}$
^{60}Co				$(7.48 \pm 0.99)10^{10}$
^{65}Ni	$(6.08 \pm 0.17)10^{8}$	$(2.97 \pm 0.10)10^{8}$	$(1.03 \pm 0.07)10^{8}$	
^{77}Ge	$(7.42 \pm 0.31)10^{8}$	$(3.13 \pm 0.19)10^{8}$	$(1.09 \pm 0.07)10^{8}$	$(1.27 \pm 0.10)10^{7}$
^{77}As	$(7.89 \pm 0.20)10^{8}$	$(3.42 \pm 0.10)10^{8}$	$(1.18 \pm 0.08)10^{8}$	$(1.41 \pm 0.11)10^{7}$
^{114m}In	$(3.28 \pm 0.06)10^{10}$	$(1.11 \pm 0.02)10^{10}$	$(3.80 \pm 0.07)10^{9}$	$(4.05 \pm 0.29)10^{8}$

Tab. A.1: Results of the specific saturation activity *of all the isotopes activated in the different irradiation facilities. The four sections include the isotopes of the STD2, STD3, STD4 and the solid samples, respectively.*

INTEGRAL NEUTRON FLUX				
Precursor isotope	Central Thimble $10^{13} n/(s \cdot cm^2)$	Rabbit Channel $10^{12} n/(s \cdot cm^2)$	Lazy Susan $10^{12} n/(s \cdot cm^2)$	Thermal Channel $10^{11} n/(s \cdot cm^2)$
^{45}Sc	1.68 ± 0.07	7.41 ± 0.30	2.54 ± 0.12	2.69 ± 0.23
^{50}Cr	1.97 ± 0.14	10.10 ± 0.50	2.62 ± 0.21	3.00 ± 0.50
^{58}Fe	1.85 ± 0.09	7.58 ± 0.32	2.78 ± 0.09	3.12 ± 0.21
^{59}Co	1.93 ± 0.13	7.91 ± 0.82	2.49 ± 0.20	2.72 ± 0.22
^{64}Ni	1.30 ± 0.04	6.29 ± 0.22	1.97 ± 0.14	
^{71}Ga	1.65 ± 0.05	6.41 ± 0.17	2.34 ± 0.07	2.46 ± 0.26
^{74}Se	1.71 ± 0.12	7.13 ± 0.52	2.46 ± 0.24	2.78 ± 0.51
^{75}As	1.58 ± 0.05	6.13 ± 0.27	2.05 ± 0.13	2.14 ± 0.29
^{76}Ge	1.51 ± 0.04	6.32 ± 0.18	1.93 ± 0.09	1.75 ± 0.10
^{102}Ru	1.48 ± 0.05	7.94 ± 0.38	2.42 ± 0.09	2.45 ± 0.26
^{109}Ag	1.52 ± 0.07	5.93 ± 0.15	2.01 ± 0.06	2.05 ± 0.11
^{113}In	2.24 ± 0.05	7.41 ± 0.14	2.41 ± 0.05	2.46 ± 0.18
^{114}Cd	1.81 ± 0.07	5.87 ± 0.40	2.20 ± 0.33	2.21 ± 0.35
^{121}Sb	1.68 ± 0.05	7.73 ± 0.26	2.25 ± 0.09	2.20 ± 0.17
^{123}Sb	1.72 ± 0.08	7.52 ± 0.39	2.16 ± 0.20	2.08 ± 0.23
^{133}Cs	1.68 ± 0.05	6.93 ± 0.30	2.50 ± 0.27	2.44 ± 0.26
^{139}La	1.69 ± 0.03	7.68 ± 0.19	2.60 ± 0.18	2.70 ± 0.19
^{151}Eu	1.69 ± 0.05	7.40 ± 0.35	2.50 ± 0.04	2.68 ± 0.18
^{152}Sm	1.70 ± 0.07	7.17 ± 0.36	2.34 ± 0.18	2.45 ± 0.31
^{153}Eu	1.57 ± 0.04	7.04 ± 0.49	2.28 ± 0.07	2.58 ± 0.75
^{159}Tb	1.77 ± 0.08	7.42 ± 0.51	2.33 ± 0.21	2.47 ± 0.24
^{165}Ho	1.75 ± 0.06	7.73 ± 0.29	2.55 ± 0.24	2.59 ± 0.43
^{174}Hf	1.75 ± 0.08	8.36 ± 0.48	2.95 ± 0.13	
^{176}Lu	1.83 ± 0.12	7.53 ± 0.45	2.56 ± 0.20	2.69 ± 0.25
^{180}Hf	1.91 ± 0.20	9.6 ± 1.1	2.67 ± 0.25	3.3 ± 1.2
^{191}Ir	1.60 ± 0.05	7.93 ± 0.37	2.46 ± 0.11	2.64 ± 0.18
^{193}Ir	1.72 ± 0.06	7.98 ± 0.27	2.43 ± 0.08	2.52 ± 0.16
^{197}Au	1.71 ± 0.09	7.59 ± 0.45	2.42 ± 0.12	2.34 ± 0.18
^{232}Th	1.90 ± 0.09	7.71 ± 0.48	2.66 ± 0.14	2.99 ± 0.60
^{238}U	1.61 ± 0.08	6.22 ± 0.30	2.11 ± 0.15	1.94 ± 0.19

Tab. A.2: Neutron flux results for all the analyzed isotopes in the four irradiation facilities.

Appendix B

Experimental data and simulation results of neutron flux distribution

^{24}Na SPECIFIC SATURATION ACTIVITY (10^7 Bq/g)				
Pos.(cm)	Hole 1	Hole 3	Hole 4	Hole 5
-25	0.701 ± 0.035	0.950 ± 0.054	0.607 ± 0.031	0.678 ± 0.041
-20	1.820 ± 0.087	2.642 ± 0.132	1.594 ± 0.074	1.686 ± 0.089
-15	4.113 ± 0.190	4.560 ± 0.222	3.797 ± 0.181	3.989 ± 0.196
-10	5.575 ± 0.264	5.821 ± 0.295	5.063 ± 0.240	5.285 ± 0.262
-5	6.305 ± 0.298	6.594 ± 0.333	5.714 ± 0.271	6.101 ± 0.308
0	6.624 ± 0.314	6.531 ± 0.334	5.913 ± 0.281	6.206 ± 0.315
5	6.225 ± 0.295	5.973 ± 0.305	5.605 ± 0.266	5.799 ± 0.297
10	5.354 ± 0.254	4.943 ± 0.255	4.839 ± 0.230	4.876 ± 0.250
15	3.175 ± 0.147	3.473 ± 0.174	3.515 ± 0.169	3.611 ± 0.174
20	1.774 ± 0.085	1.239 ± 0.068	1.541 ± 0.072	1.541 ± 0.083
25	0.753 ± 0.038	0.549 ± 0.035	0.611 ± 0.031	0.574 ± 0.037
Pos.(cm)	Hole 6	Hole 8	Hole 9	Hole 10
-25	0.520 ± 0.034	0.463 ± 0.025	0.444 ± 0.031	0.334 ± 0.018
-20	1.302 ± 0.071	1.127 ± 0.055	1.038 ± 0.059	0.693 ± 0.035
-15	3.200 ± 0.160	2.643 ± 0.128	2.674 ± 0.134	1.767 ± 0.086
-10	4.314 ± 0.226	3.497 ± 0.168	3.564 ± 0.189	2.263 ± 0.110
-5	5.034 ± 0.262	3.920 ± 0.188	3.894 ± 0.207	2.550 ± 0.123
0	5.143 ± 0.270	4.085 ± 0.196	4.036 ± 0.217	2.537 ± 0.123
5	4.855 ± 0.256	3.699 ± 0.178	3.686 ± 0.199	2.286 ± 0.111
10	4.129 ± 0.219	3.041 ± 0.147	3.329 ± 0.180	1.877 ± 0.092
15	3.079 ± 0.167	2.275 ± 0.111	2.388 ± 0.111	1.413 ± 0.070
20	1.369 ± 0.075	0.854 ± 0.043	1.008 ± 0.059	0.643 ± 0.033
25	0.512 ± 0.034	0.371 ± 0.019	0.395 ± 0.029	0.284 ± 0.016
Pos.(cm)	Hole 12	Hole 13	Hole 14	Hole 16
-25	0.642 ± 0.045	1.221 ± 0.066	0.549 ± 0.029	0.358 ± 0.019
-20	1.755 ± 0.090	2.972 ± 0.139	1.308 ± 0.061	0.689 ± 0.034
-15	4.126 ± 0.196	4.525 ± 0.209	3.183 ± 0.147	1.287 ± 0.060
-10	5.394 ± 0.284	5.438 ± 0.271	4.348 ± 0.208	1.620 ± 0.080
-5	6.465 ± 0.337	5.896 ± 0.293	5.007 ± 0.239	1.780 ± 0.088
0	6.249 ± 0.334	5.899 ± 0.298	5.180 ± 0.247	1.885 ± 0.093
5	6.374 ± 0.335	5.172 ± 0.262	4.794 ± 0.229	1.829 ± 0.091
10	5.385 ± 0.286	4.072 ± 0.210	4.122 ± 0.198	1.595 ± 0.079
15	3.853 ± 0.210	2.609 ± 0.139	2.976 ± 0.144	1.175 ± 0.059
20	1.665 ± 0.091	0.918 ± 0.052	1.289 ± 0.062	0.584 ± 0.027
25	0.713 ± 0.048	0.423 ± 0.028	0.527 ± 0.027	0.345 ± 0.018

Tab. B.1: Specific saturation activity *data of ^{24}Na, used for measuring the fast neutron flux distribution through the reaction $^{27}Al(n,\alpha)^{24}Na$.*

^{60}Co SPECIFIC SATURATION ACTIVITY (10^{12} Bq/g)				
Pos.(cm)	Hole 1	Hole 3	Hole 4	Hole 5
-25	0.708 ± 0.029	0.833 ± 0.034	0.577 ± 0.024	0.667 ± 0.028
-20	0.994 ± 0.041	1.025 ± 0.042	0.920 ± 0.038	0.895 ± 0.037
-15	1.314 ± 0.054	1.483 ± 0.061	1.104 ± 0.046	1.141 ± 0.047
-10	1.773 ± 0.073	1.895 ± 0.078	1.497 ± 0.062	1.566 ± 0.064
-5	2.089 ± 0.086	2.110 ± 0.087	1.765 ± 0.073	1.841 ± 0.076
0	2.209 ± 0.091	2.099 ± 0.086	1.836 ± 0.076	1.942 ± 0.080
5	2.208 ± 0.091	1.899 ± 0.078	1.752 ± 0.072	1.857 ± 0.076
10	1.992 ± 0.082	1.531 ± 0.063	1.486 ± 0.061	1.602 ± 0.066
15	1.176 ± 0.048	1.074 ± 0.044	1.066 ± 0.044	1.180 ± 0.049
20	0.932 ± 0.038	0.787 ± 0.033	0.743 ± 0.031	0.833 ± 0.034
25	0.530 ± 0.022	0.379 ± 0.016	0.512 ± 0.021	0.535 ± 0.022
Pos.(cm)	Hole 6	Hole 8	Hole 9	Hole 10
-25	0.698 ± 0.029	0.765 ± 0.032	0.729 ± 0.030	0.637 ± 0.026
-20	0.922 ± 0.038	0.918 ± 0.038	0.898 ± 0.037	0.760 ± 0.031
-15	1.002 ± 0.041	0.874 ± 0.036	0.817 ± 0.034	0.655 ± 0.027
-10	1.322 ± 0.056	1.042 ± 0.043	1.001 ± 0.049	0.789 ± 0.033
-5	1.534 ± 0.063	1.130 ± 0.047	1.201 ± 0.049	0.878 ± 0.036
0	1.584 ± 0.065	1.090 ± 0.045	1.250 ± 0.051	0.888 ± 0.037
5	1.493 ± 0.061	0.987 ± 0.041	1.185 ± 0.049	0.842 ± 0.035
10	1.284 ± 0.053	0.809 ± 0.033	1.024 ± 0.042	0.736 ± 0.030
15	0.949 ± 0.039	0.644 ± 0.027	0.799 ± 0.033	0.615 ± 0.025
20	0.781 ± 0.032	0.711 ± 0.029	0.791 ± 0.033	0.612 ± 0.025
25	0.576 ± 0.024	0.549 ± 0.023	0.612 ± 0.025	0.476 ± 0.020
Pos.(cm)	Hole 12	Hole 13	Hole 14	Hole 16
-25	0.687 ± 0.029	0.713 ± 0.029	0.627 ± 0.026	0.571 ± 0.024
-20	0.939 ± 0.039	0.771 ± 0.032	0.807 ± 0.033	0.678 ± 0.028
-15	1.232 ± 0.051	1.077 ± 0.044	0.850 ± 0.035	0.731 ± 0.030
-10	1.702 ± 0.070	1.337 ± 0.055	1.106 ± 0.046	0.840 ± 0.035
-5	1.962 ± 0.081	1.456 ± 0.060	1.293 ± 0.053	0.895 ± 0.037
0	2.045 ± 0.084	1.496 ± 0.062	1.391 ± 0.057	0.897 ± 0.037
5	1.978 ± 0.081	1.313 ± 0.054	1.313 ± 0.054	0.825 ± 0.034
10	1.704 ± 0.070	1.055 ± 0.044	1.135 ± 0.047	0.725 ± 0.030
15	1.251 ± 0.052	0.742 ± 0.031	0.842 ± 0.035	0.603 ± 0.025
20	0.881 ± 0.036	0.628 ± 0.026	0.726 ± 0.030	0.568 ± 0.023
25	0.566 ± 0.024	0.291 ± 0.012	0.528 ± 0.022	0.438 ± 0.018

Tab. B.2: Specific saturation activity *data of* ^{60}Co*, used for measuring the integral neutron flux distribution through the reaction* $^{59}Co(n,\gamma)^{60}Co$.

FAST NEUTRON FLUX (10^{11} n/cm^2·s)				
Pos.(cm)	Hole 1	Hole 3	Hole 4	Hole 5
-25	0.374 ± 0.019	0.507 ± 0.029	0.324 ± 0.017	0.362 ± 0.022
-20	0.970 ± 0.046	1.408 ± 0.071	0.850 ± 0.039	0.899 ± 0.047
-15	2.193 ± 0.101	2.431 ± 0.118	2.025 ± 0.097	2.127 ± 0.104
-10	2.972 ± 0.141	3.103 ± 0.157	2.699 ± 0.128	2.817 ± 0.140
-5	3.361 ± 0.159	3.515 ± 0.178	3.046 ± 0.144	3.253 ± 0.164
0	3.531 ± 0.167	3.482 ± 0.178	3.152 ± 0.150	3.309 ± 0.168
5	3.319 ± 0.157	3.184 ± 0.163	2.988 ± 0.142	3.092 ± 0.158
10	2.854 ± 0.135	2.635 ± 0.136	2.580 ± 0.123	2.599 ± 0.134
15	1.693 ± 0.078	1.852 ± 0.093	1.874 ± 0.090	1.925 ± 0.093
20	0.946 ± 0.046	0.660 ± 0.036	0.821 ± 0.038	0.822 ± 0.044
25	0.402 ± 0.020	0.293 ± 0.019	0.326 ± 0.017	0.306 ± 0.020
Pos.(cm)	Hole 6	Hole 8	Hole 9	Hole 10
-25	0.277 ± 0.018	0.247 ± 0.013	0.237 ± 0.017	0.178 ± 0.010
-20	0.694 ± 0.038	0.601 ± 0.030	0.553 ± 0.032	0.370 ± 0.018
-15	1.706 ± 0.085	1.409 ± 0.068	1.425 ± 0.072	0.942 ± 0.046
-10	2.300 ± 0.121	1.864 ± 0.089	1.900 ± 0.101	1.207 ± 0.058
-5	2.683 ± 0.140	2.090 ± 0.100	2.076 ± 0.110	1.359 ± 0.066
0	2.742 ± 0.144	2.178 ± 0.105	2.152 ± 0.116	1.352 ± 0.066
5	2.588 ± 0.136	1.972 ± 0.095	1.965 ± 0.106	1.219 ± 0.059
10	2.201 ± 0.117	1.621 ± 0.078	1.775 ± 0.096	1.001 ± 0.049
15	1.641 ± 0.089	1.213 ± 0.059	1.273 ± 0.059	0.753 ± 0.037
20	0.730 ± 0.040	0.455 ± 0.023	0.537 ± 0.031	0.343 ± 0.017
25	0.273 ± 0.018	0.198 ± 0.010	0.211 ± 0.016	0.152 ± 0.008
Pos.(cm)	Hole 12	Hole 13	Hole 14	Hole 16
-25	0.342 ± 0.024	0.651 ± 0.035	0.293 ± 0.016	0.191 ± 0.010
-20	0.935 ± 0.048	1.584 ± 0.074	0.697 ± 0.032	0.367 ± 0.018
-15	2.200 ± 0.104	2.412 ± 0.111	1.697 ± 0.078	0.686 ± 0.032
-10	2.875 ± 0.151	2.899 ± 0.144	2.318 ± 0.111	0.864 ± 0.043
-5	3.447 ± 0.180	3.143 ± 0.156	2.670 ± 0.127	0.949 ± 0.047
0	3.332 ± 0.178	3.145 ± 0.159	2.762 ± 0.132	1.005 ± 0.050
5	3.398 ± 0.178	2.757 ± 0.140	2.556 ± 0.122	0.975 ± 0.048
10	2.871 ± 0.153	2.171 ± 0.112	2.198 ± 0.105	0.851 ± 0.042
15	2.054 ± 0.112	1.391 ± 0.074	1.586 ± 0.077	0.626 ± 0.032
20	0.888 ± 0.049	0.490 ± 0.028	0.687 ± 0.033	0.311 ± 0.015
25	0.380 ± 0.025	0.225 ± 0.015	0.281 ± 0.014	0.184 ± 0.010

Tab. B.3: Fast neutron flux (E_n >4 MeV) measured in the mapped positions of TRIGA Mark II reactor core.

INTEGRAL NEUTRON FLUX (10^{13} n/cm^2·s)				
Pos.(cm)	Hole 1	Hole 3	Hole 4	Hole 5
-25	0.357 ± 0.015	0.419 ± 0.018	0.298 ± 0.013	0.345 ± 0.015
-20	0.616 ± 0.026	0.636 ± 0.027	0.593 ± 0.025	0.577 ± 0.024
-15	0.982 ± 0.041	1.108 ± 0.046	0.932 ± 0.039	0.963 ± 0.041
-10	1.328 ± 0.056	1.420 ± 0.059	1.289 ± 0.054	1.349 ± 0.056
-5	1.605 ± 0.067	1.622 ± 0.067	1.544 ± 0.064	1.610 ± 0.067
0	1.683 ± 0.070	1.599 ± 0.066	1.597 ± 0.067	1.690 ± 0.070
5	1.713 ± 0.071	1.473 ± 0.061	1.541 ± 0.064	1.633 ± 0.068
10	1.552 ± 0.065	1.193 ± 0.050	1.322 ± 0.055	1.425 ± 0.060
15	0.924 ± 0.039	0.844 ± 0.035	0.951 ± 0.040	1.052 ± 0.044
20	0.644 ± 0.027	0.543 ± 0.023	0.531 ± 0.022	0.595 ± 0.025
25	0.321 ± 0.014	0.229 ± 0.010	0.302 ± 0.013	0.316 ± 0.014
Pos.(cm)	Hole 6	Hole 8	Hole 9	Hole 10
-25	0.339 ± 0.014	0.368 ± 0.016	0.350 ± 0.015	0.306 ± 0.013
-20	0.558 ± 0.024	0.546 ± 0.023	0.534 ± 0.023	0.444 ± 0.019
-15	0.810 ± 0.034	0.775 ± 0.033	0.725 ± 0.031	0.525 ± 0.022
-10	1.077 ± 0.046	0.963 ± 0.041	0.925 ± 0.046	0.681 ± 0.029
-5	1.248 ± 0.052	1.043 ± 0.044	1.108 ± 0.047	0.779 ± 0.033
0	1.299 ± 0.054	1.007 ± 0.043	1.154 ± 0.049	0.787 ± 0.033
5	1.216 ± 0.051	0.928 ± 0.039	1.114 ± 0.047	0.746 ± 0.032
10	1.088 ± 0.046	0.751 ± 0.032	0.951 ± 0.040	0.653 ± 0.028
15	0.786 ± 0.033	0.572 ± 0.025	0.710 ± 0.030	0.514 ± 0.022
20	0.494 ± 0.021	0.424 ± 0.018	0.472 ± 0.020	0.372 ± 0.016
25	0.300 ± 0.013	0.270 ± 0.011	0.300 ± 0.013	0.239 ± 0.010
Pos.(cm)	Hole 12	Hole 13	Hole 14	Hole 16
-25	0.356 ± 0.015	0.419 ± 0.018	0.309 ± 0.013	0.275 ± 0.012
-20	0.617 ± 0.026	0.693 ± 0.029	0.498 ± 0.021	0.407 ± 0.017
-15	0.989 ± 0.041	0.997 ± 0.042	0.702 ± 0.029	0.612 ± 0.026
-10	1.376 ± 0.057	1.234 ± 0.052	0.929 ± 0.039	0.729 ± 0.031
-5	1.569 ± 0.065	1.329 ± 0.056	1.075 ± 0.045	0.803 ± 0.034
0	1.629 ± 0.068	1.360 ± 0.057	1.162 ± 0.049	0.810 ± 0.034
5	1.571 ± 0.065	1.192 ± 0.050	1.081 ± 0.045	0.744 ± 0.032
10	1.391 ± 0.058	0.971 ± 0.041	0.947 ± 0.040	0.650 ± 0.028
15	1.003 ± 0.042	0.629 ± 0.027	0.693 ± 0.029	0.508 ± 0.022
20	0.598 ± 0.025	0.372 ± 0.016	0.451 ± 0.019	0.349 ± 0.015
25	0.315 ± 0.014	0.150 ± 0.007	0.276 ± 0.012	0.220 ± 0.009

Tab. B.4: Integral neutron flux measured in the mapped positions of TRIGA Mark II reactor core.

INTEGRAL NEUTRON FLUX (10^{13} n/cm^2·s) BY MCNP SIMULATIONS			
Pos.(cm)	Hole 1	Hole 4	Hole 6
-25	0.364 ± 0.002	0.337 ± 0.002	0.329 ± 0.002
-20	0.633 ± 0.004	0.576 ± 0.003	0.540 ± 0.003
-15	1.060 ± 0.006	0.918 ± 0.006	0.834 ± 0.005
-10	1.439 ± 0.009	1.233 ± 0.007	1.106 ± 0.007
-5	1.655 ± 0.010	1.421 ± 0.009	1.280 ± 0.008
0	1.721 ± 0.010	1.478 ± 0.009	1.329 ± 0.008
5	1.632 ± 0.010	1.401 ± 0.008	1.261 ± 0.008
10	1.374 ± 0.008	1.199 ± 0.007	1.089 ± 0.007
15	0.998 ± 0.006	0.861 ± 0.005	0.799 ± 0.005
20	0.558 ± 0.003	0.500 ± 0.003	0.497 ± 0.003
25	0.283 ± 0.002	0.259 ± 0.002	0.278 ± 0.002
Pos.(cm)	Hole 8	Hole 10	Hole 12
-25	0.294 ± 0.002	0.261 ± 0.002	0.366 ± 0.002
-20	0.454 ± 0.003	0.386 ± 0.002	0.645 ± 0.004
-15	0.642 ± 0.004	0.515 ± 0.003	1.069 ± 0.006
-10	0.830 ± 0.005	0.645 ± 0.004	1.452 ± 0.009
-5	0.944 ± 0.006	0.729 ± 0.004	1.697 ± 0.010
0	0.976 ± 0.006	0.750 ± 0.004	1.741 ± 0.010
5	0.924 ± 0.006	0.719 ± 0.004	1.640 ± 0.010
10	0.806 ± 0.005	0.623 ± 0.004	1.396 ± 0.008
15	0.616 ± 0.004	0.490 ± 0.003	1.023 ± 0.006
20	0.434 ± 0.003	0.360 ± 0.002	0.605 ± 0.004
25	0.276 ± 0.002	0.243 ± 0.001	0.318 ± 0.002
Pos.(cm)	Hole 13	Hole 14	Hole 16
-25	0.467 ± 0.003	0.330 ± 0.002	0.276 ± 0.002
-20	0.776 ± 0.005	0.543 ± 0.003	0.399 ± 0.002
-15	1.121 ± 0.007	0.826 ± 0.005	0.536 ± 0.003
-10	1.363 ± 0.008	1.091 ± 0.007	0.662 ± 0.004
-5	1.479 ± 0.009	1.262 ± 0.008	0.743 ± 0.004
0	1.441 ± 0.009	1.304 ± 0.008	0.756 ± 0.005
5	1.285 ± 0.008	1.236 ± 0.007	0.720 ± 0.004
10	1.002 ± 0.006	1.041 ± 0.006	0.626 ± 0.004
15	0.655 ± 0.004	0.770 ± 0.005	0.495 ± 0.003
20	0.372 ± 0.002	0.490 ± 0.003	0.369 ± 0.002
25	0.164 ± 0.001	0.280 ± 0.002	0.240 ± 0.001

Tab. B.5: Integral neutron flux evaluated in the mapped positions of TRIGA Mark II reactor core through MCNP simulations (the positions referring to hole 13 are shifted by 3 cm upwards to take into account the experimental positioning offset).

Appendix C

Core reconfiguration data

Core Position	**Configuration 9/9/13**		**Configuration 25/9/13**	
	FE#	B.I.(%)	FE#	B.I.(%)
B1	10004	3.70	10901	1.16
B2	10662	3.72	10002	5.39
B3	10085	2.23	10085	2.23
B4	10663	2.82	10899	1.15
B5	10002	5.39	10902	0.84
B6	7876	6.41	7876	6.41
C1	10900	1.31	10900	1.31
C2	7901	6.03	7899	6.00
C3	SHIM		SHIM	
C4	7897	8.35	7901	6.03
C5	10896	1.38	10663	2.82
C6	10003	3.82	10004	3.70
C7	10898	1.53	10898	1.53
C8	4976	10.23	10662	3.72
C9	7900	8.66	10897	1.41
C10	10897	1.41	10003	3.82
C11	7898	8.25	10896	1.38
C12	7902	8.48	7903	4.73
D1	4982	12.46	3660	9.04
D2	10899	1.15	3652	11.28
D3	7905	6.49	3576	9.08
D4	4980	14.26	3767	9.00
D5	4977	9.75	3657	8.90
D6	4978	13.16	3653	6.18
D7	9680	5.64	9680	5.64
D8	4981	13.51	3765	1.41
D9	4979	13.95	3546	8.83
D10	TRANSIENT		TRANSIENT	
D11	7899	6.00	3549	9.14
D12	4984	10.33	3540	6.55
D13	4983	10.97	3669	8.71
D14	10902	0.84	3764	6.68
D15	7904	6.43	3763	8.37
D16	7903	4.73	3545	6.81
D17	10901	1.16	3542	8.14
D18	4985	13.72	3537	7.10

Continued on next page

Tab. C.1 – continued from previous page

Core Position	Configuration 9/9/13		Configuration 25/9/13	
	FE#	B.I.(%)	FE#	B.I.(%)
E1	3068	9.49	3659	10.16
E2	3668	9.69	3655	10.20
E3	3538	9.38	3662	10.20
E4	3537	7.10	3531	12.15
E5	3553	9.18	3553	9.18
E6	3529	9.49	3582	9.25
E7	3528	9.97	3538	9.38
E8	3663	10.09	3760	9.45
E9	3764	6.68	3547	9.48
E10	3662	10.20	3529	9.49
E11	3659	10.16	3068	9.49
E12	3665	11.16	3530	9.53
E13	3664	10.81	3766	9.56
E14	3657	8.90	3580	9.67
E15	3766	9.56	3668	9.69
E16	3666	9.90	3579	9.75
E17	3426	10.99	3656	9.83
E18	3655	10.20	3757	9.84
E19	3658	10.20	3666	9.90
E20	3661	10.32	3532	9.97
E21	REGULATING		REGULATING	
E22	3579	9.75	3528	9.97
E23	3576	9.08	3577	10.08
E24	3584	11.24	3663	10.09
F1	3540	6.55	Dummy	
F2	3577	10.08	Dummy	
F3	Dummy		Dummy	
F4	Neutron Source		Neutron Source	
F5	Dummy		Dummy	
F6	3759	10.27	Dummy	
F7	3549	9.14	3759	10.27
F8	3656	9.83	7902	8.48
F9	3670	11.97	3670	11.97
F10	3455	10.39	7897	8.35
F11	3546	8.83	4985	13.72

Continued on next page

Tab. C.1 – continued from previous page

Core Position	Configuration 9/9/13		Configuration 25/9/13	
	FE#	B.I.(%)	FE#	B.I.(%)
F12	3651	10.53	4982	12.46
F13	3531	12.15	3584	11.24
F14	3760	9.45	4983	10.97
F15	3582	9.25	3455	10.39
F16	3545	6.81	4976	10.23
F17	3763	8.37	3664	10.81
F18	3767	9.00	4984	10.33
F19	3547	9.48	3426	10.99
F20	3532	9.97	7905	6.49
F21	3542	8.14	3651	10.53
F22	3580	9.67	4977	9.75
F23	3765	1.41	3661	10.32
F24	Rabbit Channel		Rabbit Channel	
F25	3578	10.94	3578	10.94
F26	3652	11.28	7904	6.43
F27	3653	6.18	3658	10.20
F28	3530	9.53	7898	8.25
F29	3669	8.71	3665	11.16
F30	3757	9.84	7900	8.66
OUT	3762 (a)	9.01	3762 (a)	9.01
OUT	3551 (a)	7.52	3551 (a)	7.52
OUT	3541 (b)	5.88	3541 (b)	5.88
OUT	3581 (c)	8.76	3581 (c)	8.76
OUT	3660	9.04	4978	13.16
OUT			4979	13.95
OUT			4980	14.26
OUT			4981	13.51

*Tab. C.1: The "*old*" and the "*new*" core configurations (referring to September 9 and September 25, 2013, respectively) with the comparison of the burnup indexes (B.I.) corresponding to the fuel elements. The FEs labeled with "a" are elongated more than 5 mm, the "b" FE is the one not entering in the upper grid and the "c" FE is the one that is impossible to hook.*

Acknowledgments

It is with immense gratitude that I acknowledge the support and help of professors Ezio Previtali and Monica Sisti, who guided me with their great expertise in Physics during my Ph.D. Particularly, I would like to thank Ezio for being passionated and open-minded in leading the research project, discussing the ideas, promoting new experiments, analyzing the results and so much more. Many thanks to Monica for her precious contribution to the research activity and for her valuable advices.

I would also like to acknowledge the collaboration of the researchers at the Polytechnic University of Milan, guided by Prof. Antonio Cammi, and at the Applied Nuclear Energy Laboratory (L.E.N.A.), directed by Dr. Andrea Salvini: it is also thanks to their expertise that it was possible to perform the research project described in this thesis.

I am really grateful to Massimiliano Clemenza and Massimiliano Nastasi for their willingness to carry out the experimental measurements at any time of the day (and night).

Special thanks to Stefano Pozzi: he proved to be an outstanding graduating student and an excellent colleague, contributing to the development of the Monte Carlo simulation models from the desk next to mine.

Finally, I would like to thank my parents, Fiorella and Roberto, for giving me the opportunity to study and for supporting me every moment of my life. And last, but not least, my heartfelt thanks go to my fiancée Attilia, for her patient, encouraging and loving support.

Davide Chiesa

Bibliography

[1] G. F. Bassani *et al.*, "Energy in Italy: problems and perspectives (1990-2020)," *Il Nuovo Cimento*, vol. 10-11, 2009. [p. 1]

[2] M. Vazquez, H. Tsige-Tamirat, L. Ammirabile, and F. Martin-Fuertes, "Coupled neutronics thermal-hydraulics analysis using Monte Carlo and sub-channel codes," *Nuclear Engineering and Design*, vol. 250, pp. 403–411, 2012. [p. 2]

[3] J. R. Lamarsh, *Introduction to Nuclear Reactor Theory*. Addison-Wesley Publishing Company, 1966. [pp. 5, 52, 106]

[4] J. J. Duderstadt and L. J. Hamilton, *Nuclear Reactor Analysis*. John Wiley and Sons, Inc., 1976. [pp. 5, 18]

[5] W. M. Stacey, *Nuclear Reactor Physics*. WILEY-VCH Verlag GmbH & Co. KGaA, 2007. [pp. 5, 132]

[6] R. E. MacFarlane, "New thermal neutron scattering files for ENDF/B-VI release 2," Tech. Rep. LA-12639-MS, Los Alamos National Laboratory, 1994. [p. 14]

[7] M. Mattes and J. Keinert, "Thermal Neutron Scattering Data for the Moderator Materials H_2O, D_2O and ZrH_x in ENDF-6 Format and as ACE Library for MCNP(X) Codes," Tech. Rep. INDC(NDS)-0470, International Nuclear Data Committee, 2005. [p. 14]

[8] M. F. James, "Energy released in fission," *Journal of Nuclear Energy*, vol. 23, pp. 517–536, 1969. [p. 18]

[9] A. Borio di Tigliole, A. Cammi, M. Clemenza, V. Memoli, L. Pattavina, and E. Previtali, "Benchmark evaluation of reactor critical parameters

and neutron fluxes distributions at zero power for the TRIGA Mark II reactor of the University of Pavia using the Monte Carlo code MCNP," *Progress in Nuclear Energy*, vol. 52, pp. 494–502, 2010. [pp. 37, 57, 64]

[10] E. L. Slaggie, "Central force lattice dynamical model for zirconium hydride," *Journal of Physics and Chemistry of Solids*, vol. 29, pp. 923–934, 1968. [p. 41]

[11] X-5 Monte Carlo Team, *MCNP - A General Monte Carlo N-Particle Transport Code, Version 5*. Los Alamos National Laboratory, 2008. [p. 49]

[12] Members of the Cross Sections Evaluation Working Group (last revision edited by M. Herman and A. Trkov), "ENDF-6 formats manual," Tech. Rep. BNL-90365-2009, Brookhaven National Laboratory, 2009. [p. 50]

[13] R. E. MacFarlane, "An introduction to the ENDF formats." Lectures given at the Workshop on Nuclear Data and Nuclear Reactors: Physics, Design and Safety. Trieste, 13 March - 14 April 2000. [p. 50]

[14] M. B. Chadwick and *et al.*, "ENDF/B-VII.1 Nuclear Data for Science and Technology: Cross Sections, Covariances, Fission Product Yields and Decay Data," *Nuclear Data Sheets*, vol. 112, pp. 2887–2996, 2011. [p. 51]

[15] A. Koning, C. Dean, U. Fischer, and R. Mills, "Validation of the JEFF-3.1 Nuclear Data Library," Tech. Rep. NEA-7079, Nuclear Energy Agency, 2013. [p. 51]

[16] K. Shibata and *et al.*, "JENDL-4.0: A New Library for Nuclear Science and Engineering," *Journal of Nuclear Science and Technology*, vol. 48, no. 1, pp. 1–30, 2011. [p. 51]

[17] L. Pattavina, "Studio dei parametri di criticità e della distribuzione dei flussi neutronici del reattore TRIGA Mark II del L.E.N.A. mediante codice di simulazione Monte Carlo," Master's thesis, Università degli Studi di Milano-Bicocca, 2007. [p. 57]

[18] A. Cambieri, F. Cingoli, S. Meloni, and E. Orvini, "Il reattore TRIGA Mark II da 250 kW, pulsato, dell'Università di Pavia. Rapporto finale sulle prove nucleari," tech. rep., Università di Pavia, Laboratorio Energia Nucleare Applicata, 1965. [pp. 57, 80]

[19] W. P. Eatherly, M. Janes, R. L. Mansfield, R. G. Bourdeau, and R. A. Meyer, "Physical properties of graphite materials for special nuclear applications," Tech. Rep. A/CONF.15/P/708, National Carbon Co., New York; Brookhaven National Lab., Upton, N.Y., 1958. [p. 68]

[20] University of Arizona, "Activation analysis and component characterization," Tech. Rep. 08-125D-RE-122, 2009. [p. 68]

[21] W. W. Tyler and A. C. Wilson, Jr, "Thermal conductivity, electrical resistivity and thermoelectric power of graphite," *Physical Review*, vol. 89, no. 4, pp. 870–875, 1953. [p. 68]

[22] E. Fermi, "Experimental production of a divergent chain reaction," *American Journal of Physics*, vol. 20, no. 9, pp. 536–558, 1952. [p. 68]

[23] W. M. Manning and O. C. Simpson, "Summary Report for July, August and September, 1948," Tech. Rep. ANL-4258(Del.), Argonne National Laboratory, 1949. [p. 68]

[24] L. Snoj, A. Trkov, M. Ravnik, and G. Zerovnik, "Testing of cross section libraries on zirconium benchmarks," *Annals of Nuclear Energy*, pp. 71–79, 2012. [p. 68]

[25] B. Pritychenko and S. F. Mughabghab, "Neutron Thermal Cross Sections, Westcott Factors, Resonance Integrals, Maxwellian Averaged Cross Sections and Astrophysical Reaction Rates Calculated from the ENDF/B-VII.1, JEFF-3.1.2, JENDL-4.0, ROSFOND-2010, CENDL-3.1 and EAF-2010 Evaluated Data Libraries," *Nuclear Data Sheets*, pp. 3120–3144, 2012. [pp. 68, 102]

[26] D. Chiesa, "Caratterizzazione dei flussi neutronici del reattore TRIGA Mark II del L.E.N.A. con l'analisi della loro dipendenza dalle temperature," Master's thesis, Università degli Studi di Milano-Bicocca, 2010. [p. 70]

[27] A. Cammi, R. Ponciroli, A. Borio di Tigliole, G. Magrotti, M. Prata, D. Chiesa, and E. Previtali, "A Zero Dimensional Model for Simulation of TRIGA Mark II Dynamic Response," *Progress in Nuclear Energy*, vol. 68, pp. 43–54, 2013. [p. 77]

[28] COMSOL Inc., *COMSOL Multiphysics 4.3a User's Guide*, 2012. [p. 77]

[29] S. Agostinelli and *et al.*, "Geant4: A simulation toolkit," *Nucl. Instr. Meth. A*, vol. 506, pp. 250–303, 2003. [p. 83]

[30] M. Clemenza, G. Cucciati, V. Maggi, L. Pattavina, and E. Previtali, "Radioactive fallouts as temporal makers for glacier ice cores dating," *Eur. Phys. J. Plus*, vol. 127, no. 68, pp. 1–8, 2012. [pp. 88, 99]

[31] G. Steinhauser, S. Merz, F. Stadlbauer, P. Kregsamer, C. Streli, and M. Villa, "Performance and comparison of gold-based neutron flux monitors," *Gold Bulletin*, 2012. [p. 95]

[32] J. W. Beeman and *et al.*, "Current Status and Future Perspectives of the LUCIFER Experiment," *Advances in High Energy Physics*, pp. 1–15, 2013. Article ID 237973. [p. 99]

[33] W. N. McElroy, S. Berg, T. Crockett, and R. Hawkins, "A computer-automated iterative method for neutron flux spectra determination by foil activation," Tech. Rep. AFWL-TR-67-41, Vol. 1, Air Force Weapons Laboratory, Reasearch and Techology division, 1967. [p. 99]

[34] A. Gelman, J. B. Carlin, H. S. Stern, and D. B. Rubin, *Bayesian Data Analysis*. Chapman and Hall/CRC, 2004. [pp. 100, 101]

[35] W. J. Metzger, "Statistical methods in data analysis," 2010. Fakulteit der Natuurwetenschappen, Radboud Universiteit Nijmegen. [p. 101]

[36] G. Casella and E. I. George, "Explaining the Gibbs Sampler," *The American Statistician*, vol. 46, no. 3, pp. 167–174, 1992. [p. 101]

[37] W. K. Hastings, "Monte Carlo Sampling Methods Using Markov Chains and Their Applications," *Biometrika*, vol. 57, no. 1, pp. 97–109, 1970. [p. 101]

[38] M. Plummer, *JAGS Version 3.3.0 User Manual*, 2012. [p. 101]